The pattern effect and its implications for climate sensitivity

Yue Dong

A dissertation
submitted in partial fulfillment of the
requirements for the degree of

Doctor of Philosophy

University of Washington

2021

Reading Committee:

David S. Battisti, Chair

Kyle C. Armour

Cecilia M. Bitz

Program Authorized to Offer Degree:
Atmospheric Sciences

University of Washington

Abstract

The pattern effect and its implications for climate sensitivity

Yue Dong

Chair of the Supervisory Committee:
Dr. David S. Battisti
Department of Atmospheric Sciences

Radiative feedbacks depend on the spatial pattern of sea-surface temperatures (SSTs) and thus can change over time as SST patterns evolve – the so-called pattern effect. The radiative feedbacks within atmospheric general circulation models (AGCMs) forced by historical observed SST patterns are generally more negative than those within fully-coupled GCMs forced with increasing CO_2, yielding to a lower value of equilibrium climate sensitivity (ECS) estimates from historical energy budget constraints. The anomalously negative radiative feedbacks are traced to the observed SST pattern over recent decades, featuring enhanced warming the tropical western Pacific and broad cooling in the tropical eastern Pacific and part of the Southern Ocean, which tends to strengthen lower tropospheric stability and enhance tropical low cloud cover.

In Chapter 1, I first describe the global-mean energy budget framework underlying the modern estimates of ECS and radiative feedbacks, and common approaches to quantify the global energy budget in GCMs and in observations. Then I introduce the pattern effect and its implications for ECS estimates. Last, I summarize the overarching research questions that motivate this thesis.

In Chapter 2, I examine inter-model differences in the magnitude of the pattern effect, the source of their differences, and how these differences contribute to the spread in ECS within CMIP5 and CMIP6 models. The results show that the inter-model spread in ECS is dominated by the spread in radiative response on fast timescales (mainly reflecting different

atmospheric physics) rather than by the spread in feedback evolution over time (governed by evolving SST patterns).

In Chapter 3, I assess ECS and radiative feedbacks derived from historical energy budget constraints within historical simulations of CMIP6 GCMs, and compare them with those from observed energy budget constraints and those from long-term GCM simulations forced by CO_2 quadrupling. The results show that historical energy budget constraints generally underestimate values of ECS from CO_2 quadrupling, owing to the pattern effect. The observation-based ECS estimates are even lower than those from GCM historical simulations, due to discrepancies between modeled and observed historical SST patterns.

In Chapter 4, I explore the causes of the observed tropical Pacific SST pattern, and particularly focus on linking the tropical Pacific SSTs with the observed Southern Ocean climate change. I find that there is a two-way teleconnection between the tropical Pacific and the Southern Ocean via atmospheric pathways, associated with regional atmospheric circulations instead of zonal-mean energetic constraints as previously proposed. The results highlight potential impacts on the tropics from the extratropical climate changes that have occurred over the instrumental record.

In Chapter 5, I discuss implications of this study and open research questions inferred from the results of this study.

TABLE OF CONTENTS

LIST OF FIGURES

ACKNOWLEDGMENTS

First, I wish to express my greatest appreciation to my advisors in the Department of Atmospheric Sciences, Prof. David Battisti and Prof. Kyle Armour. Working and exploring sciences with both of them has been the most enjoyable experience in my graduate life. I have been constantly inspired by how they think of a science question within a big picture. I am grateful for all the support, encouragement, inspiration, freedom and guidance that they generously shared with me.

I would like to express my gratitude to Prof. Cecilia Bitz, another member of my thesis reading committee, for her constructive suggestions. My gratitude also goes to Prof. Dargan Frierson and Prof. LuAnne Thompson in my committee. I appreciated all the insightful comments and inspiring questions from my committee during my general exam and defense presentation.

I would like to also express my appreciation to my coauthors and collaborators: Cristian Proistosescu, Malte Stuecker, Robert Jnglin Wills, Edward Blanchard-Wrigglesworth, Timothy Andrews, Mark Zelinka and Andrew Pauling. I enjoyed my collaborations with them all, which not only helped my past several projects, but also expanded my horizon to think broadly. I also appreciate all the help and support from the Armour group and the Bitz group. Every time I practiced my presentation to the groups, I received constructive comments and insightful feedback which were very helpful. It was also nice to keep in touch with people and support each other in group meetings during the pandemic shutdown, even on Zoom.

I would like to thank all my friends in Atmospheric Sciences, specially to my cohort (class 16) and my office-mates (Stephanie Rushley and Wei-Yi Cheng). There were many times that Stephanie kindly helped me to look over the emails or announcements that I wrote in some important occasions, to make sure that my writing flows well. Thanks to

Litai Kang, Shuting Zhai, Xiaojuan Liu, and Ping-Ping Narenpitak, for spending their time listening and chatting with me when I directly walked into their office in the middle of their work. Thanks to Lauren Schmeisser and Katie Brennan, for sharing with me their wisdom of teaching (ATMS 220). Thanks to Isabel McCoy and Casey Wall for sharing with me their experience of applying for postdoc fellowships. Thanks to ATG staff, Hettie Scofield, Jennifer Siembor, Erica Coleman for kindly helping me with all the documents and processes needed for my concurrent MS degree in Applied Mathematics, my teaching, and my PhD defense seminar.

Last, my special thanks go to Xiaoli Zhou. Her accompany during the pandemic and pre-defense period made my quarantine time full of colors. Her patience and open-minded thinking gave me much relief during my application for postdoc fellowships and those times when I was stuck on Chapter 4. My sincere gratitude also goes to my family. My parents have been generously supporting me to pursue research, and constantly caring about me especially during the pandemic, which was more than valuable to me.

Chapter 1

INTRODUCTION

The first calculation of the global climate change due to an increase in CO_2 that made use of an idealized climate model was the ground breaking paper of Manabe and Wetherald in 1967. Nearly a half century of further research by the climate community has led to a public awareness about climate change due to to anthropogenic emissions of greenhouse gases (GHG). Yet, how much the Earth would warm in response to GHG forcing remains a key question in climate science.

This warming is often quantified in terms of the Equilibrium Climate Sensitivity (ECS), defined as the equilibrium global surface temperature change in response to a doubling of atmospheric CO_2 concentration relative to pre-industrial levels. Manabe and Wetherald (1967) estimated a value of climate sensitivity of 2.3°C within their idealized radiative-convective model. The Intergovernmental Panel on Climate Change (IPCC)'s 5th assessment report (Flato et al., 2014), based in part on the estimates of state-of-the-art global climate models (GCMs), reported a likely range (66% confidence) in ECS values of 1.5–4.5°C. This range was narrowed down to 2.6–3.9°C in a recent WCRP report (Sherwood et al., 2020), which used a Bayesian approach to combine multiple lines of observational evidence. The updated range of ECS values is also reported in the IPCC AR6 published this year (Forster et al., 2021), with a best estimate of 3°C within the likely range of 2.5–4.0°C. While the initial estimate of Manabe and Wetherald (1967) appeared to be in good agreement with modern estimates, substantial uncertainty still exists in the estimated values of ECS. In particular, some of the latest generation of GCMs participated in the Coupled Model Intercomparison Project phase 6 (CMIP6) produce values of ECS beyond 5°C (Zelinka et al., 2020), raising a debate of whether such a high value of ECS is realistic.

Before going to the details of physical processes that govern the uncertainty in ECS estimates, one might ask: why do we care about the equilibrium response, which would

take thousands of years to fully emerge? Indeed, estimates of transient climate change in the near future may seem to be more informative and intuitive to policy makers and public. However, most of the spread in model-projected global warming in the 21st century under realistic emission scenarios has been found to be explained by ECS (Grose et al., 2018; Sherwood et al., 2020). This suggests that ECS is a good predictor of future warming. A better understanding of ECS will lead to a better constraint on both the 21st century and equilibrium climate change.

Uncertainty in ECS estimates arises primarily from uncertainty in radiative feedbacks – a quantity representing the efficiency with which the climate system radiates energy to space in response to surface warming. When a radiative forcing (ΔF), for instance from CO_2 increase, is imposed to the climate, the change in the global energy balance can be formulated as Gregory et al. (2004):

$$\Delta N = \Delta F + \lambda \Delta T, \tag{1.1}$$

where ΔN is global-mean top of atmosphere (TOA) radiation imbalance (approximately equal to ocean heat uptake), and the Earth's radiative response is taken to be proportional to the change in global-mean near-surface air temperature (ΔT) where λ is called the radiative feedback parameter. As such, λ represents the amount of outgoing radiative fluxes per unit of global surface warming. The net λ is the sum of Planck response and feedbacks associated with changes in the atmospheric lapse rate, water vapor, clouds and surface albedo. Here I follow the convention of defining λ to be negative for a stable climate, with a more-negative λ implying that the Earth needs to warm less to balance an imposed positive radiative forcing. When a new equilibrium state is achieved (i.e., $\Delta N = 0$), the temperature change at that equilibrium state can be inferred from the imposed forcing ΔF and the net equilibrium radiative feedback λ. In this manner, ECS can be represented as:

$$\mathrm{ECS} = -\frac{F_{2\mathrm{x}}}{\lambda_{\mathrm{eq}}}, \tag{1.2}$$

where $F_{2\mathrm{x}}$ is the effective radiative forcing due to a doubling of CO_2 and λ_{eq} is the net radiative feedback acting in the equilibrium state. While $F_{2\mathrm{x}}$ is now well quantified (Forster et al., 2021), constraining values of λ remains a challenger for ECS estimates.

Estimates of the net radiative feedback and ECS can be derived from multiple lines of evidence (Sherwood et al., 2020). A common approach to estimate λ and ECS within fully-coupled GCMs is to make use of simulations forced by abrupt CO_2 quadrupling ("abrupt-4xCO2"). Because the abrupt-4xCO2 simulations are generally run for only 150 years, values of ECS estimated from these non-equilibrium simulations are often referred to as an *effective* climate sensitivity (EffCS), assuming that the radiative feedback at the transient state would remain constant to equilibrium. Another widely used approach to estimate λ and ECS is to make use of historical energy budget. Over a given historical period with sufficient observations, the global energy budget (Eq. 1.1) gives us:

$$\lambda = \frac{\Delta N - \Delta F}{\Delta T}, \tag{1.3}$$

where Δ denotes changes between two historical states. This approach also provides constraints on EffCS estimates. However, estimates of EffCS from observed historical energy budget constraints have been found to be substantially lower than those from GCM abrupt-4xCO2 simulations (Forster, 2016; Otto et al., 2013; Sherwood et al., 2020). This discrepancy raises an important question: do GCMs overestimate future warming?

In fact, the mismatch between GCM-based estimates and observation-based estimates is greatly reduced when using atmospheric GCMs (AGCMs) forced by the observed sea-surface temperature (SST) and sea-ice concentration (SIC). Values of EffCS from these AGCM prescribed-SST simulations are well in line with those from observed energy budget constraints, but lower than those from their counterpart fully-coupled models forced by CO_2 quadrupling (Andrews et al., 2018; Gregory and Andrews, 2016). The difference in the EffCS estimates between AGCM prescribed-SST simulations and their coupled counterpart abrupt-4xCO2 simulations is thus due to differences between observed and modeled SST patterns (Fig. 1.1), which drive different radiative feedbacks. Indeed, the observed SST trends over recent decades exhibit a pattern that is not seen in the fully-coupled climate models under historical forcings, featuring enhanced warming in the tropical west Pacific and broad cooling in the eastern Pacific and part of the Southern Ocean (Fig. 1.1a). In contrast, abrupt-4xCO2 simulations generally project an equilibrium warming pattern characterized by enhanced warming in the tropical eastern Pacific and Southern Ocean

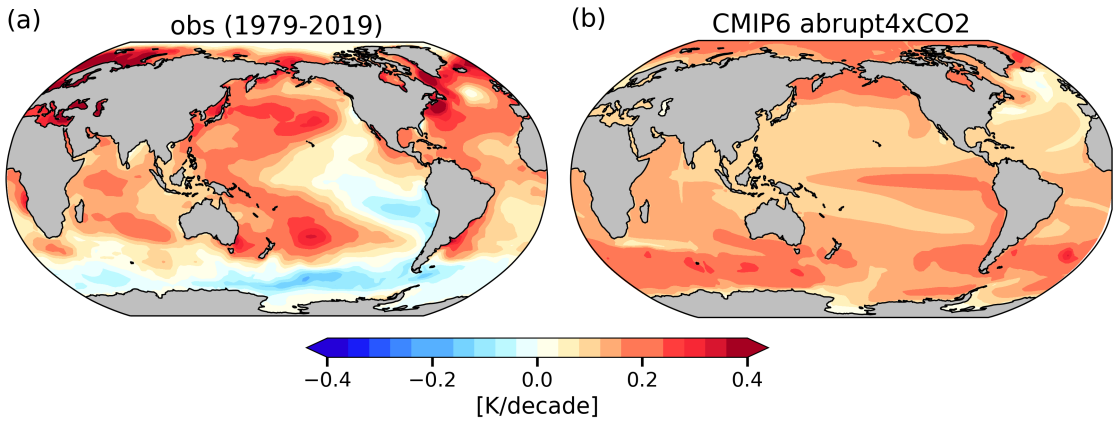

Figure 1.1: Observed historical and modelded near-equilibrium SST patterns. (a) Observed pattern of annual-mean SST trends (K/decade) over 1979–2019, from the average of four observational datasets: HadISST1, AMIPII, COBE-SST2, ERSSTv5. (b) CMIP6 abrupt-4xCO2 SST trend pattern. The SST trends are calculated from the mean of 31 CMIP6 models, over the 150yrs of the simulations.

relative to the tropical western Pacific (Fig. 1.1b). The different warming patterns in observations and simulations induce different radiative feedbacks. As the surface warming pattern evolves with time, the radiative feedbacks also change with time, violating the key assumption often applied in the literature that radiative feedbacks are constant over time. These findings suggest that estimates of EffCS and λ derived from transient states may lead to a biased constraint on the true equilibrium ECS and λ_{eq}, owing to changes in surface warming patterns – this is referred to as the *pattern effect* (Stevens et al., 2016).

What physical processes account for the differences in the net feedback strength? My Master Thesis work (Dong et al., 2019) investigated this question using a Green's function approach. The Green's function is derived from a suite of prescribed-SST simulations within the Community Atmosphere Model version 4 (CAM4), each with a localized patch of SST and/or SIC anomalies. The Green's function allows us to attribute changes in the global energy budget as well as λ to SST changes in each region. The results highlight the preeminent impact of surface warming in ascent regions of the tropical western Pacific on global TOA radiation change (Fig. 1.2a). Over the tropical western Pacific, where the sur-

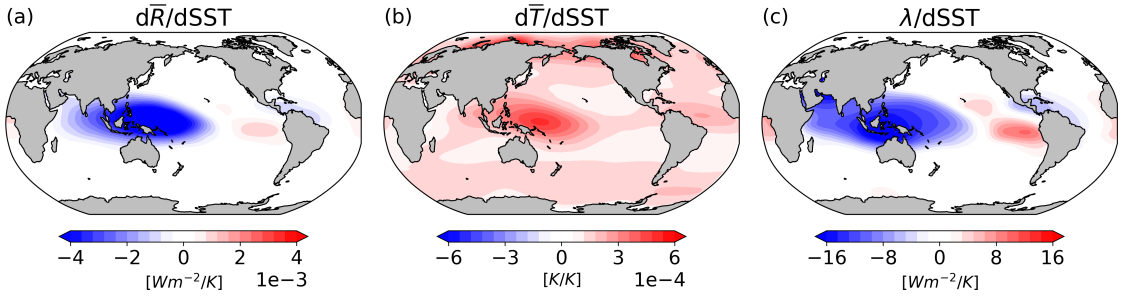

Figure 1.2: The results of the Green's function. Response of global-mean (a) net TOA radiation, (b) near-surface air temperature, and (c) net radiative feedback per unit local SST warming in each grid box. Adapted from Dong et al. (2019).

face is tightly coupled to the free troposphere by deep convection, surface warming directly enhances upper tropospheric warming, leading to strengthened lower tropospheric stability over other regions. In turn, the enhanced stability causes a strong negative lapse-rate feedback and a negative cloud feedback over low-cloud regions, resulting in more efficient radiative damping at TOA (a more-negative λ). On the other hand, the weaker coupling between surface and upper troposphere warming in extratropics results in a weak TOA radiation response to surface warming and decreased lower tropospheric stability, leading to a weaker negative lapse-rate feedback and a more-positive cloud feedback, and therefore, an inefficient radiative damping (a less-negative λ). Therefore, changes in λ can be traced to changes in the ratio of surface warming over the tropical western Pacific relative to all other oceans (Fig. 1.2c). The observed historical warming pattern over recent decades features more warming in the tropical western Pacific and delayed warming or cooling in the rest of the global oceans, which favors a more-negative λ and lower EffCS. Yet the projected equilibrium warming pattern highlights more warming in the eastern Pacific and Southern Ocean relative to the western Pacific, which favors a less-negative λ and higher EffCS. The key importance of warm pool warming for TOA radiation changes is also supported by observational evidence (Ceppi and Gregory, 2017; Fueglistaler, 2019; Zhou et al., 2016).

Having established a physical mechanism for how the pattern effect within a single

atmospheric model, my PhD work seeks to develop a more comprehensive understanding on the pattern effect in both multi-model ensembles and observations, as well as their implications on future climate projections. The next three chapters of this dissertation address the following questions from different aspects:

1. My Master Thesis work and other previous studies have shown that estimates of λ and EffCS within an individual model depend on the pattern of SST changes. **How does the pattern effect differ across CMIP5 and CMIP6 GCMs? Furthermore, to what extent does the pattern effect contribute to the model spread in ECS estimates?** To address these questions, I will describe an inter-model comparison work in Chapter 2, where I examine the pattern effect and their contribution to ECS estimates in CMIP5 and CMIP6 models.

2. Published studies have shown that EffCS values from abrupt-4xCO2 simulations are larger than values of EffCS derived from observed historical energy budget constraints. **Does this imply that the models are overly sensitive? How do the estimates of EffCS from historical simulations compare with those from observations?** To address these questions, I will describe a study focused on the historical energy budget constraints on EffCS estimates within a subset of CMIP6 models in Chapter 3.

3. The observed pattern of SST trends in the tropical Pacific over recent decades has profound impacts on both global and regional climate change, while the underlying causes of the observed SST pattern remain unclear. **Is the observed La Niña-like of tropical SST connected to the observed cooling trends in the Southern Ocean? If so, what is the leading mechanism for this extratropics-to-tropics teleconnection? Moreover, what implications does this teleconnection have on our interpretations of the observed and projected global SST patterns, and thus on EffCS?** To address these questions, I will describe a study using a hierarchy of model simulations in Chapter 4, where I investigate the pathways linking the Southern Ocean to tropical Pacific SSTs.

Chapter 2

INTER-MODEL SPREAD IN THE PATTERN EFFECT AND ITS CONTRIBUTION TO CLIMATE SENSITIVITY IN CMIP5 AND CMIP6 MODELS

(This chapter is published as Dong, Y., Armour, K. C., Zelinka, M. D., Proistosescu, C., Battisti, D. S., Zhou, C., Andrews, T. (2020). Intermodel spread in the pattern effect and its contribution to climate sensitivity in CMIP5 and CMIP6 models. Journal of Climate, 33(18), 7755-7775.)

Abstract

Radiative feedbacks depend on the spatial patterns of sea-surface temperature (SST) and thus can change over time as SST patterns evolve – the so-called "pattern effect". This study investigates inter-model differences in the magnitude of the pattern effect and how these differences contribute to the spread in effective equilibrium climate sensitivity (ECS) within CMIP5 and CMIP6 models. Effective ECS in CMIP5 estimated from 150-year-long abrupt4xCO2 simulations is on average 10% higher than that estimated from the early portion (first 50 years) of those simulations which serves as an analog for historical warming; this difference is reduced to 7% on average in CMIP6. The (negative) net radiative feedback weakens over the course of the abrupt4xCO2 simulations in the vast majority of CMIP5 and CMIP6 models, but this weakening is less dramatic on average in CMIP6. For both ensembles, the total variance in the effective ECS is found to be dominated by the spread in radiative response on fast timescales, rather than the spread in feedback changes. Using Green's functions derived from two AGCMs shows that the spread in feedbacks on fast timescales may be primarily due to differences in atmospheric model physics, whereas the spread in feedback evolution is primarily governed by differences in SST patterns. Inter-model spread in feedback evolution is well explained by differences in the relative warming in the West Pacific warm-pool regions for the CMIP5 models, but this relation fails to explain

differences across the CMIP6 models, suggesting that a stronger sensitivity of extratropical clouds to surface warming may also contribute to feedback changes in CMIP6.

2.1 Introduction

Uncertainty in estimates of equilibrium climate sensitivity (ECS) – the equilibrium surface temperature change in response to a doubling of CO_2 above pre-industrial levels – has long been linked to uncertainty in the radiative feedbacks (λ) that govern the efficiency with which the climate system radiates energy to space per degree of surface warming. The strength of λ is intrinsically set by black-body radiation, which is further modulated by radiative feedbacks associated with changes in atmospheric lapse rate, water vapor, surface albedo, and clouds. Among these, the cloud feedback has been found to be the primary source of ECS uncertainty (Caldwell et al., 2018, 2016; Ceppi et al., 2017; Dufresne and Bony, 2008; Soden and Held, 2006; Webb et al., 2013, 2006; Zelinka et al., 2020, 2016). The low-cloud feedback is particularly uncertain (Ceppi et al., 2017; Webb et al., 2006), leading to tremendous efforts in the community to constrain it (Bony et al., 2006)).

Within global climate models (GCMs), ECS is often estimated based on a standard linear framework for global energy balance:

$$N = F + \lambda T, \tag{2.1}$$

$$\mathrm{ECS} = T_{\mathrm{eq}} = -\frac{F_{2\mathrm{x}}}{\lambda_{\mathrm{eq}}}, \tag{2.2}$$

where F is the effective radiative forcing (with $F_{2\mathrm{x}}$ representing forcing from CO_2 doubling), and where the subscript eq denotes the equilibrium state when N approaches zero. All variables represent global-mean anomalies with respect to a pre-industrial state. A useful method to derive λ and ECS from simulations of abrupt CO2 doubling or quadrupling was proposed by Gregory et al. (2004), regressing net TOA radiation imbalance (N) against surface-air-temperature change (T) (hereafter referred to as "Gregory $N - T$ regression", with the graphical illustration of this regression referred to as a "Gregory plot"). This method has been widely used to provide estimates of λ (regression slope), $F_{2\mathrm{x}}$ (from the y-axis intercept), and ECS (from the x-axis intercept), but is only valid under the assumption

that λ is constant over time, i.e., $\lambda = \lambda_{\text{eq}}$ at any given time. This general assumption may be violated for several reasons. For example, a discrepancy between λ and λ_{eq} may arise from nonlinear state-dependence of some feedbacks on global-mean or local temperature (Bloch-Johnson et al., 2015, 2021). For instance, sea-ice albedo feedback will become less-positive as the amount of sea ice decreases with warming (Goosse et al., 2018) while the water vapor feedback (Meraner et al., 2013) and cloud feedback (Caballero and Huber, 2013) may both become more positive with warming. Most importantly, the majority of GCMs in Coupled Model Intercomparison Project phases 5 and 6 (CMIP5 and CMIP6) exhibit a weakening of the negative net feedback as time evolves after CO_2 forcing is imposed, indicated by a curvature in the Gregory $N - T$ regression (Andrews et al., 2015; Armour et al., 2013; Lewis and Curry, 2018; Proistosescu and Huybers, 2017). The time-dependence of λ has been found to arise primarily from its dependence on the spatial pattern of sea-surface temperature (SST), which itself can evolve over time (Andrews et al., 2018; Armour et al., 2013; Ceppi and Gregory, 2017; Dong et al., 2019; Haugstad et al., 2017; Zhou et al., 2016) – the so-called "pattern effect" (Stevens et al., 2016). An important implication is that the climate sensitivity inferred from the historical energy budget is biased low compared to the climate sensitivity estimated over longer timescales under CO_2 forcing due to the evolution of surface warming patterns (Andrews et al., 2018; Armour, 2017; Dong et al., 2019; Gregory et al., 2020; Marvel et al., 2018; Proistosescu and Huybers, 2017; Rugenstein et al., 2020). What is less-well understood, however, is what sets the magnitude of the inter-model spread in the degree of feedback curvature in the Gregory regression (Andrews et al., 2015; Armour, 2017; Ceppi and Gregory, 2017). Moreover, the contribution of model spread in feedback curvature to the model spread in ECS estimates has not yet been quantified. This work addresses these two key issues in both CMIP5 and CMIP6 models.

We first present an overview of net feedbacks in CMIP5 and CMIP6 models by showing the Gregory $N - T$ regression for the 150-yr-long simulations of abrupt CO_2 quadrupling (hereafter abrupt4xCO2) (Fig. 2.1). Following Andrews et al. (2015), we calculate radiative feedbacks based on regression over a fast time-scale (years 1-20) and over a slow time-scale (years 21-150), noted hereafter as $\lambda_{1\text{-}20}$ and $\lambda_{21\text{-}150}$, respectively. We calculate values of N and T in each model with respect to their pre-industrial control simulations (piControl)

after accounting for drift by subtracting the linear regression of piControl values over time segment corresponding to the abrupt4xCO2 simulation, following Forster et al. (2013) and Armour (2017). All of the anomalies used in this study are annual-mean quantities. Note that we use year 20 to separate the fast response on decadal timescales from the slow response on centennial timescales, following many existing studies, but results are insensitive to the year chosen (Andrews et al., 2015). ECS estimated using the regression method over the course of abrupt4xCO2 simulations is often referred to as the effective equilibrium climate sensitivity (Andrews et al., 2018, 2015; Andrews and Webb, 2018; Gregory et al., 2020), as it presumably differs from the true ECS of the Earth system that would be found by equilibrating over multiple millennia (Rugenstein et al., 2020). In this study, we use several measures of the effective ECS derived from extrapolation of the Gregory $N - T$ regressions to the x-axis (divided by two to account for CO_2 quadrupling) and distinguish them with a subscript denoting the years over which the regression was performed. Specifically, we use $ECS_{1\text{-}20}$, $ECS_{21\text{-}150}$ and $ECS_{1\text{-}150}$, corresponding to values derived from the regressions over years 1–20, years 21–150, and years 1–150, respectively. Of these three, $ECS_{21\text{-}150}$ provides the most accurate estimate of the true ECS in 8 GCMs analyzed by R(Rugenstein et al., 2020), so we will make this approximation and refer the effective ECS of each model to their $ECS_{21\text{-}150}$ values here.

Fig. 2.1 shows that for both CMIP5 and CMIP6, the ensemble-mean (negative) net feedback weakens towards the longer timescales. That is, there is a positive change in the (negative) net feedback ($\Delta\lambda = \lambda_{21\text{-}150} - \lambda_{1\text{-}20} > 0$) across 23 of 24 CMIP5 models and 26 of 29 CMIP6 models, indicating that $ECS_{1\text{-}20}$ is nearly always smaller than $ECS_{21\text{-}150}$ in both CMIP5 and CMIP6. Comparing the two ensembles, we find that $ECS_{1\text{-}20}$ and $ECS_{21\text{-}150}$ on average are higher in CMIP6 relative to CMIP5, although they have larger variance in CMIP6 (Fig. 2.1; Tables 2.1, 2.2). Several up-to-date studies of individual CMIP6 models (Gettelman et al. 2019 for CESM2, Golaz et al. 2019 for E3SM; Sellar et al. 2019 for UKESM1; Bodas-Salcedo et al. 2019 for HadGEM3; Andrews et al. 2019 for HadGEM3-GC3.1 and UKESM1) report that the higher values of ECS in their models are largely due to stronger positive cloud feedbacks, which is recently confirmed to be a common feature in the CMIP6 ensemble by Zelinka et al. (2020). Here, by quantifying λ on different timescales, we

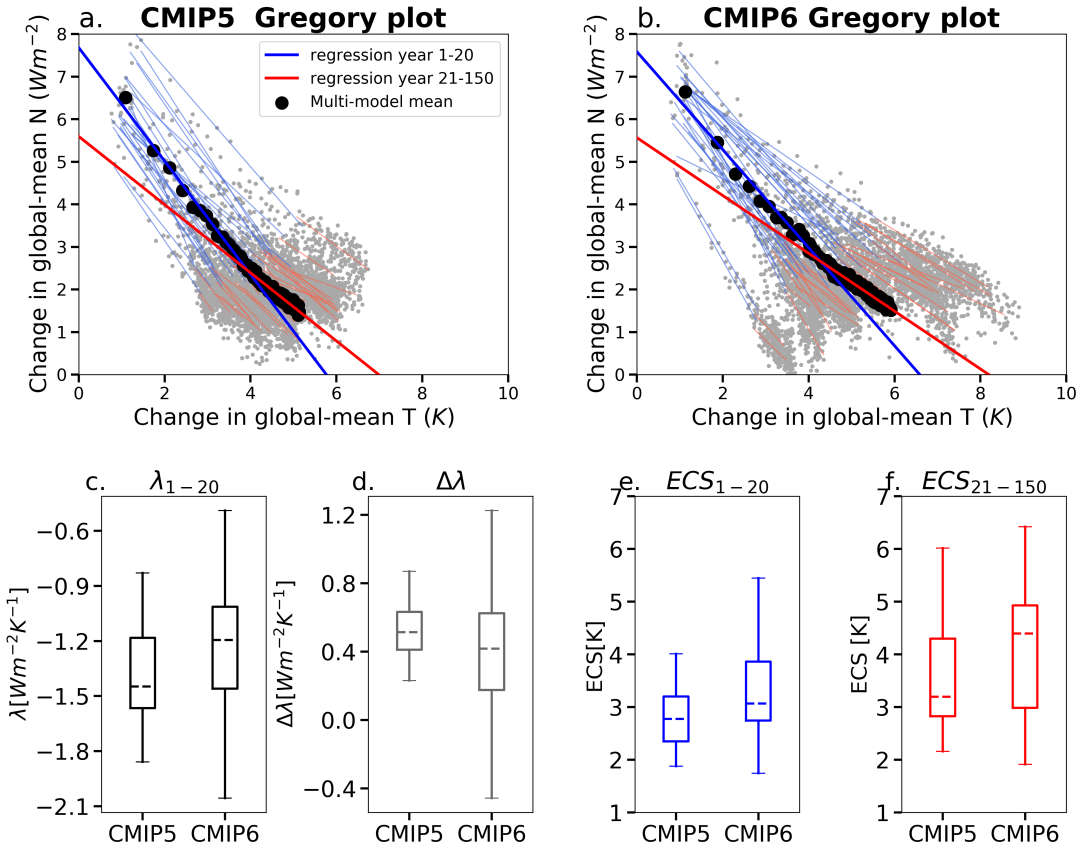

Figure 2.1: (a, b) Gregory plots for (a) CMIP5 and (b) CMIP6: annual-mean change in global-mean net TOA radiation (Wm^{-2}) against annual-mean change in global-mean surface air temperature (K) from abrupt4xCO2 experiments. Gray dots denote each year from each model, black dots denote each year of multi-model means. Thin (thick) lines show regression fits for years 1–20 (blue) and for years 21–150 (red) for each model (multi-model means). The slope of blue line represents feedback parameter on the fast time-scale ($\lambda_{1\text{-}20}$), and the slope of red line represents feedback parameter on the longer time-scale ($\lambda_{21\text{-}150}$). (c, d, e, f) Box plots of $\lambda_{1\text{-}20}$ ($\mathrm{Wm}^{-2}\mathrm{K}^{-1}$), $\Delta\lambda$ ($\mathrm{Wm}^{-2}\mathrm{K}^{-1}$), $\mathrm{ECS}_{1\text{-}20}$ (K) and $\mathrm{ECS}_{21\text{-}150}$ (K) in CMIP5 (left) and CMIP6 (right) models. The box indicates interquartile range (IQR), the whiskers indicate 1.5*IQR range, the dashed line inside box indicates the median value, for each quantity.

find that both $\lambda_{1\text{-}20}$ (feedback strength on the fast timescale) and $\lambda_{21\text{-}150}$ (feedback change over time) are, on average, different in CMIP6 relative to CMIP5 (Fig. 2.1). Key questions are: (i) how do $\lambda_{1\text{-}20}$ and $\Delta\lambda$ contribute to the spread in ECS across models and between CMIP5 and CMIP6 ensembles, and how does the pattern effect over historical period change from CMIP5 to CMIP6, (ii) what causes the differences in $\Delta\lambda$ across models and between CMIP5 and CMIP6 ensembles, and (iii) what physical mechanisms govern $\lambda_{1\text{-}20}$ and $\Delta\lambda$?

Motivated by the three questions, we assess the effective ECS, $\lambda_{1\text{-}20}$ and $\Delta\lambda$ within 24 CMIP5 models and 29 CMIP6 models. In section 2.2, we investigate the source of model spread in the effective ECS relating the radiative response on fast timescale and the pattern effect on slow timescale, and also estimate the ECS bias relative to historical estimates in both ensembles. In section 2.3, we compare the ensemble-mean $\Delta\lambda$ in the CMIP5 and CMIP6 models. In section 2.4, we investigate the inter-model spread in $\lambda_{1\text{-}20}$ and $\Delta\lambda$ separately, and track down the key regions of the pattern effect that are most responsible for driving the spread in $\Delta\lambda$ across the CMIP5 and CMIP6 models.

2.2 The contribution of the pattern effect to the variance of ECS estimates

Fig. 2.1d shows that $\Delta\lambda$ is on average smaller in CMIP6 models (0.4 $\mathrm{Wm^{-2}K^{-1}}$) than in CMIP5 models (0.53 $\mathrm{Wm^{-2}K^{-1}}$), despite the fact that $\mathrm{ECS}_{21\text{-}150}$ is on average higher in CMIP6 (Fig. 2.1f) (corresponding to an overall less-negative λ). That is, higher CMIP6-mean effective ECS is not coming from a stronger pattern effect (it is weaker, in fact); it is likely due to less-negative feedbacks on the fast timescale and stronger radiative forcing (Zelinka et al., 2020). However, there remains the possibility that inter-model spread in $\Delta\lambda$ may contribute to the spread in effective ECS. Therefore, we first estimate the degree to which $\Delta\lambda$ affects the spread in $\mathrm{ECS}_{21\text{-}150}$ across models (subsection 2.2.1). Then we use abrupt4xCO2 simulations as an analog for historical warming (following Lewis and Curry 2018) to estimate the degree to which the pattern effect causes historical estimates of effective ECS to be less than $\mathrm{ECS}_{21\text{-}150}$ (or $\mathrm{ECS}_{1\text{-}150}$) in CMIP5 and CMIP6 models (subsection 2.2.2).

2.2.1 Correlation between $ECS_{21\text{-}150}$ and $ECS_{1\text{-}20}$

Previous studies (Caldwell et al., 2016; Dufresne and Bony, 2008) partitioning ECS into components associated with radiative feedbacks and radiative forcing have identified feedbacks as the dominant source of the ECS spread across models. To estimate the relative roles of $\lambda_{1\text{-}20}$ and $\Delta\lambda$ in setting ECS, we evaluate the correlation between $\mathrm{ECS}_{21\text{-}150}$ and $\mathrm{ECS}_{1\text{-}20}$. Without any pattern effect induced variance, $\mathrm{ECS}_{21\text{-}150}$ and $\mathrm{ECS}_{1\text{-}20}$ would be highly correlated.

The correlation (r^2) between $\mathrm{ECS}_{21\text{-}150}$ and $\mathrm{ECS}_{1\text{-}20}$ is 0.69 in CMIP5 and 0.70 in CMIP6, respectively; both correlations are statistically significant at 95% confidence level. This indicates that the total variance of $\mathrm{ECS}_{21\text{-}150}$ can be primarily explained by the spread in the radiative response on fast timescales, even without considering the feedback evolution due to the pattern effect. The degree to which feedbacks change over time ($\Delta\lambda$) thus explains, at most, 30% of the total variance in ECS in both model ensembles, given the fact that $\lambda_{1\text{-}20}$ and $\Delta\lambda$ are weakly correlated ($r^2 = 0.3$ for CMIP5 and $r^2 = 0.2$ for CMIP6).

These results suggest that the differences in feedback evolution on longer timescales contribute much less to the spread in $\mathrm{ECS}_{21\text{-}150}$ than do the differences in feedbacks on the fast timescales ($\lambda_{1\text{-}20}$), even though this measure of ECS here is based on the latter period of the abrupt4xCO2 simulations (years 21-150). However, it is worth noting that in both ensemble-means and in individual models, $\Delta\lambda$ is generally positive (23 of 24 CMIP5 models and 26 of 29 CMIP6 models), $\mathrm{ECS}_{21\text{-}150}$ is nearly always greater than that derived from early portion of the simulation ($\mathrm{ECS}_{1\text{-}20}$). Thus, while $\lambda_{1\text{-}20}$ is the major driver of variance in ECS, ignoring $\Delta\lambda$ and using an assumption of time-invariant feedbacks would lead to a low estimate of the true ECS (as estimated here by $\mathrm{ECS}_{21\text{-}150}$).

2.2.2 ECS-to-ECS_{hist} ratio

As many studies have shown, the value of ECS estimated from historical energy budget constraints is lower than that based on the behavior of fully-coupled and atmosphere-only GCM simulations (Andrews et al., 2018; Armour, 2017; Gregory et al., 2020; Lewis and Curry, 2018; Marvel et al., 2018; Proistosescu and Huybers, 2017). Multiple factors have

contributed to the spatial pattern of warming, and thus the pattern effect, over the historical period, including the inherent timescales of ocean adjustment to radiative forcings (Armour, 2017; Marvel et al., 2016; Proistosescu and Huybers, 2017) as well as unforced internal climate variability (Andrews et al., 2018; Marvel et al., 2018). The distinction between forced and unforced pattern effects is further discussed in Dessler (2020). In this subsection, we consider how the forced pattern effect may bias values of ECS inferred from historical warming based on the behavior of the CMIP5 and CMIP6 models' response to CO_2 forcing.

Following Armour (2017) and Andrews et al. (2018), we rewrite Eq. (2.2) as:

$$\mathrm{ECS} = -\frac{F_{2\mathrm{x}}}{\lambda_{\mathrm{eq}}} = -\frac{F_{2\mathrm{x}}}{\lambda_{\mathrm{hist}} + \lambda'}, \tag{2.3}$$

where λ_{hist} is the feedback parameter estimated from historical energy budget constraints, λ' is the change in feedback at the equilibrium state relative to the historical period. Using λ_{hist} based on historical energy budgets, one can make an estimate of climate sensitivity (termed $\mathrm{ECS}_{\mathrm{hist}}$ herein):

$$\mathrm{ECS}_{\mathrm{hist}} = -\frac{F_{2\mathrm{x}}}{\lambda_{\mathrm{hist}}}, \tag{2.4}$$

which will underestimate the value of ECS if $\lambda' > 0$. Note that while λ' is expected to have the same sign of $\Delta\lambda$ (positive in most GCMs), their magnitudes will be smaller. $\Delta\lambda$ is defined as the change in feedbacks between the first 20 years and the last 130 years of abrupt4xCO2 simulations, whereas λ' is defined in terms of how feedbacks will change from historical warming to equilibrium warming under CO_2 forcing. Armour (2017) (hereafter A17) and Lewis and Curry (2018) (hereafter LC18) proposed a ratio of ECS to $\mathrm{ECS}_{\mathrm{hist}}$ (hereafter "ECS-to-$\mathrm{ECS}_{\mathrm{hist}}$ ratio") to quantify the difference in ECS estimates, and reported the CMIP5-mean ECS-to-$\mathrm{ECS}_{\mathrm{hist}}$ ratio as 1.095 (LC18) or 1.26 (A17). The difference between these estimates is attributed to the differences in the method and timescale of regression used and to differences in assumptions about how CO_2 forcing scales with CO_2 concentration (LC18).

Ideally, estimates of λ_{hist} and $\mathrm{ECS}_{\mathrm{hist}}$ require accurate estimates of historical energy budgets from observations or GCM simulations with all historical forcing agents included (e.g. historical simulations). In the latter case, additional simulations with the same historical forcings but fixed SSTs are needed to diagnose the magnitude of forcing, namely,

the Radiative Forcing Model Intercomparion Project (RFMIP; Pincus et al. 2016). Given the absence of the RFMIP simulations for the majority of the current CMIP5 and CMIP6 models, several ways to approximate $\mathrm{ECS_{hist}}$ are proposed, for example, using abrupt4xCO2 or 1pctCO2 simulations as an analog for historical warming (A17, LC18), or estimating historical forcings based on empirical scaling (Gregory et al., 2020). Here, following LC18, we make use of the early portion of abrupt4xCO2 simulations as a historical analog to estimate $\mathrm{ECS_{hist}}$ by regressing N against T over years 2–50 of each model's abrupt4xCO2 simulation. We also calculate $F_{2\mathrm{x}}$ by scaling the y-axis intercept of the regression of N against T over years 2–10. Long-term ECS here is estimated from the regression of N against T over years 21–150 (equal to $\mathrm{ECS_{hist}}$), which is the same period used in both A17 and LC18, but using Deming regression to be consistent with LC18 for comparison. We also provide the results using a more conventional estimate of ECS derived from the $N - T$ regression over years 1-150 ($\mathrm{ECS_{1\text{-}150}}$; shown in parenthesis in Table 2.3).

The results of individual CMIP6 models and ensemble-means are shown in Table 2.3. The pattern-effect induced feedback evolution from the historical period to equilibrium (λ') is on average weaker in CMIP6 models (0.06 $\mathrm{Wm^{-2}K^{-1}}$) relative to CMIP5 models (0.092 $\mathrm{Wm^{-2}K^{-1}}$), so that the ECS-to-$\mathrm{ECS_{hist}}$ ratio is also reduced in the CMIP6 ensemble-mean (6%) compared to the CMIP5 ensemble-mean (9.5%; consistent with LC18). This suggests that the latest generation of GCMs produce an overall smaller ECS-to-$\mathrm{ECS_{hist}}$ ratio, consistent with results above that the pattern effect is slightly smaller in the abrupt4xCO2 simulations. However, there remains a large spread across CMIP6 models: λ' varies from 0.3 $\mathrm{Wm^{-2}K^{-1}}$ to -0.23 $\mathrm{Wm^{-2}K^{-1}}$, corresponding to ECS values that are 40% higher to 12% lower than $\mathrm{ECS_{hist}}$.

We note an important caveat of this analysis regarding the calculation of $\mathrm{ECS_{hist}}$. Making use of abrupt4xCO2 simulations as an analog for the historical energy budget is a useful approach as it enables inter-model comparison, but it may produce different values of $\mathrm{ECS_{hist}}$ than those estimated from historical simulations which include a more realistic time-evolution of CO_2 and non-CO_2 forcings as well as an unforced pattern effect (Andrews et al., 2019; Gregory et al., 2020; Marvel et al., 2016). For example, Andrews et al. (2019) found that $\mathrm{ECS_{hist}}$ within historical simulations of HadGEM3-GC3.1-LL is 4.7K, with a

ECS-to-ECS_{hist} ratio of 1.21. For comparison, using HadGEM3-GC3.1-LL's abrupt4xCO2 simulation, our calculation gives an ECS_{hist} of 5.2 K, and an ECS-to-ECS_{hist} ratio of 1.08 (Table 2.3), suggesting that the values reported here may underestimate the historical forced pattern effect. However, as our main focus is to provide information on the difference in pattern effect between the CMIP5 and CMIP6 ensembles, rather than to provide a definitive ECS_{hist} metric for each model. Future work employing RFMIP simulations to accurately quantify radiative feedbacks in the historical simulations of CMIP6 models is needed to shed light on this in greater detail.

2.3 The consistency and difference in ensemble-mean $\Delta\lambda$ between CMIP5 and CMIP6

Even though $\Delta\lambda$ does not contribute as much as $\lambda_{1\text{-}20}$ to the inter-model spread in ECS, it substantially affects ECS estimates for both CMIP5-mean and CMIP6-mean projections (comparing $ECS_{1\text{-}20}$ to $ECS_{21\text{-}150}$ in Figs. 2.1ef). In this section, we first compare the global-mean $\Delta\lambda$ and its individual components partitioned by radiative kernels. We then examine the spatial patterns of ensemble-mean $\Delta\lambda$ from CMIP5 and CMIP6 models. A comparison of SST patterns is also provided to aid in uncovering the causes of ensemble differences.

Fig. 2.2 shows global-mean net $\Delta\lambda$ and its individual components associated with changes in atmospheric temperature, water vapor, lapse rate, surface albedo and clouds, estimated using radiative kernels (Huang et al., 2017b) as described in Zelinka et al. (2020). We calculate the cloud feedback using radiative kernels by removing cloud masking effects from the temperature-mediated change in net cloud radiative effect. An overall consistency between CMIP5 and CMIP6 is found in the fact that the dominant contribution to the ensemble-mean $\Delta\lambda$ comes from the net cloud component ($\Delta\lambda_{\mathrm{CLD}}$), followed by the sum of lapse rate ($\Delta\lambda_{\mathrm{LR}}$) and water vapor ($\Delta\lambda_{\mathrm{WV}}$) components. Both CMIP5 and CMIP6 have a large spread in the net $\Delta\lambda$, primarily owing to the spread in $\Delta\lambda_{\mathrm{CLD}}$. However, the (positive) ensemble-mean net $\Delta\lambda$ is slightly smaller in CMIP6, primarily due to a smaller surface-albedo feedback change ($\Delta\lambda_{\mathrm{ALB}}$), particularly from the Northern Hemisphere (NH).

We next show the spatial patterns of ensemble-mean feedbacks for the CMIP5 and

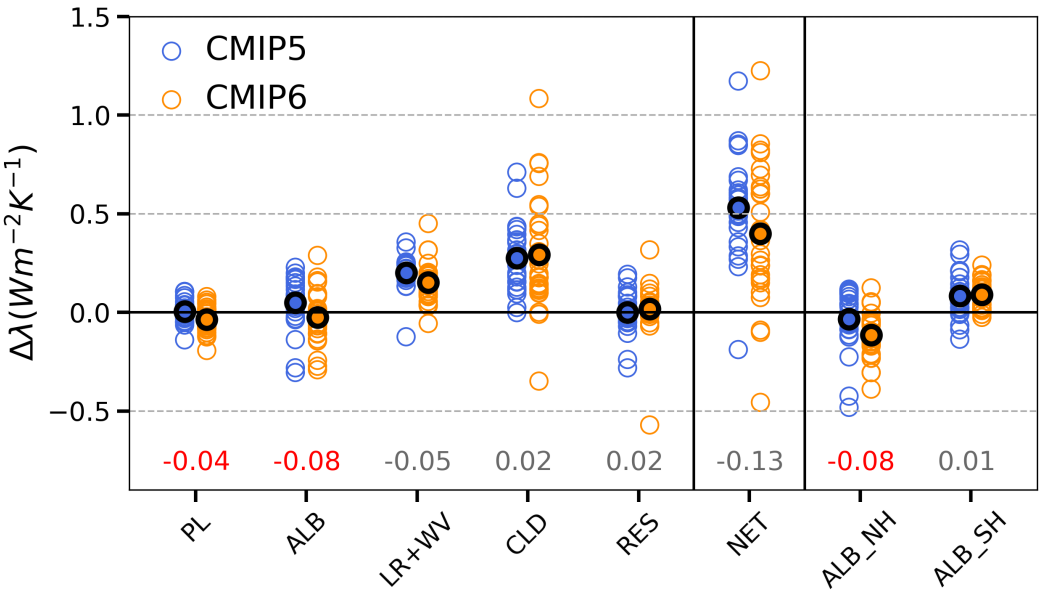

Figure 2.2: $\Delta\lambda$ for each individual CMIP5 models (blue circles), CMIP6 models (orange circles), and their multi-model means (black circles), decomposed into contributions of (from left to right) Planck (PL), surface-albedo (ALB), the sum of lapse-rate (LR) and water vapor (WV), net cloud (CLD), and residual (RES), respectively. The $\Delta\lambda_{\mathrm{ALB}}$ is further broken down into contributions from Northern Hemisphere and Southern Hemisphere. The differences between CMIP5-means and CMIP6-means are printed at the bottom, with red numbers highlighting multi-model means that are significantly different ($p<0.05$)

CMIP6 models (Figs. 2.3, 2.4). The feedback patterns are first calculated for each model by regressing the corresponding local N against global-mean T over the two separate time periods, and then averaging across models. The patterns of local contributions to the net feedback change are qualitatively consistent between the two ensemble-means (Figs. 3, 4, the first row). That is, the positive changes in the net feedback primarily come from the tropical eastern Pacific. This is a region where a cool ocean and a strong capping inversion promote ubiquitous low clouds in the climatology. Because warmer surface temperatures and weaker low-level stability in this region both reduce low cloud cover, delayed warming in this region will yield a less-negative feedback during the approach toward equilibrium (Ceppi and Gregory, 2017; Zhou et al., 2016). Indeed, among all individual components, cloud feedback and lapse-rate feedback contribute the most to the positive change in the net feedback over this region in both CMIP5 and CMIP6. The major difference between the two ensembles lies in the Arctic, where positive surface-albedo feedback strengthens with time in the CMIP5 models (Fig. 2.3 bottom row) but weakens over time in the CMIP6 models (Fig. 2.4 bottom row), consistent with the regional attribution results in Fig. 2.2.

Changes in the strength of the surface-albedo feedback may arise from changes in the sensitivity of local albedo to local surface temperature (a nonlinear state-dependence, e.g., Goosse et al. 2018), or from differences in surface warming patterns acting on constant local surface-albedo feedbacks (e.g., Armour et al. 2013), or from a combination of these two factors. The state-dependence can be identified through changes in the local surface-albedo feedback, which is defined by regressing local N onto local T (rather than global T), assuming that the local surface-albedo feedback is independent of the pattern of surface warming. We found that the local surface-albedo feedback over the Arctic slightly strengthens over time in both ensembles, indicating a nonlinear state-dependence, but that the change in local surface-albedo feedback from fast to slow timescale is nearly identical in the CMIP5 and CMIP6 multi-model means. Moreover, while this nonlinear state-dependence induced strengthening of the local surface-albedo feedback over time may enhance the strengthening of the Arctic surface-albedo feedback within CMIP5 (Fig. 2.3 bottom row), it opposes to the weakening of the Arctic surface-albedo feedback within CMIP6 (Fig. 2.4 bottom row), suggesting that $\Delta\lambda_{\mathrm{ALB}}$ is primarily governed by changing warming patterns rather than by

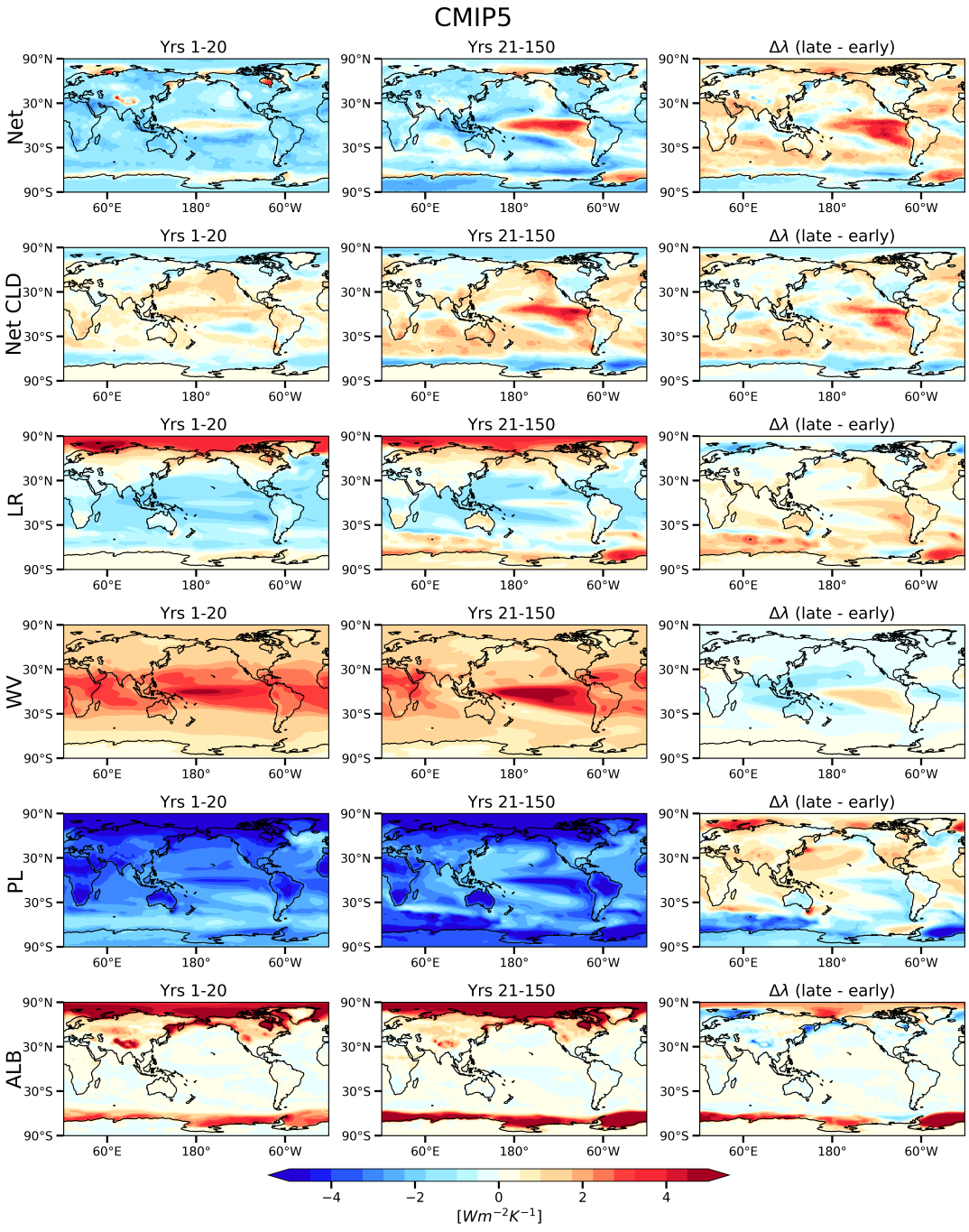

Figure 2.3: CMIP5 ensemble-mean spatial patterns of the local radiative feedback components (calculated by regressing the local N against global-mean T). (top to bottom) net feedback, net cloud feedback, lapse-rate feedback, water-vapor feedback, Planck feedback, surface-albedo feedback, on (left) years 1-20 and (middle) years 21-150 time-scales, and (right) the change (late minus early).

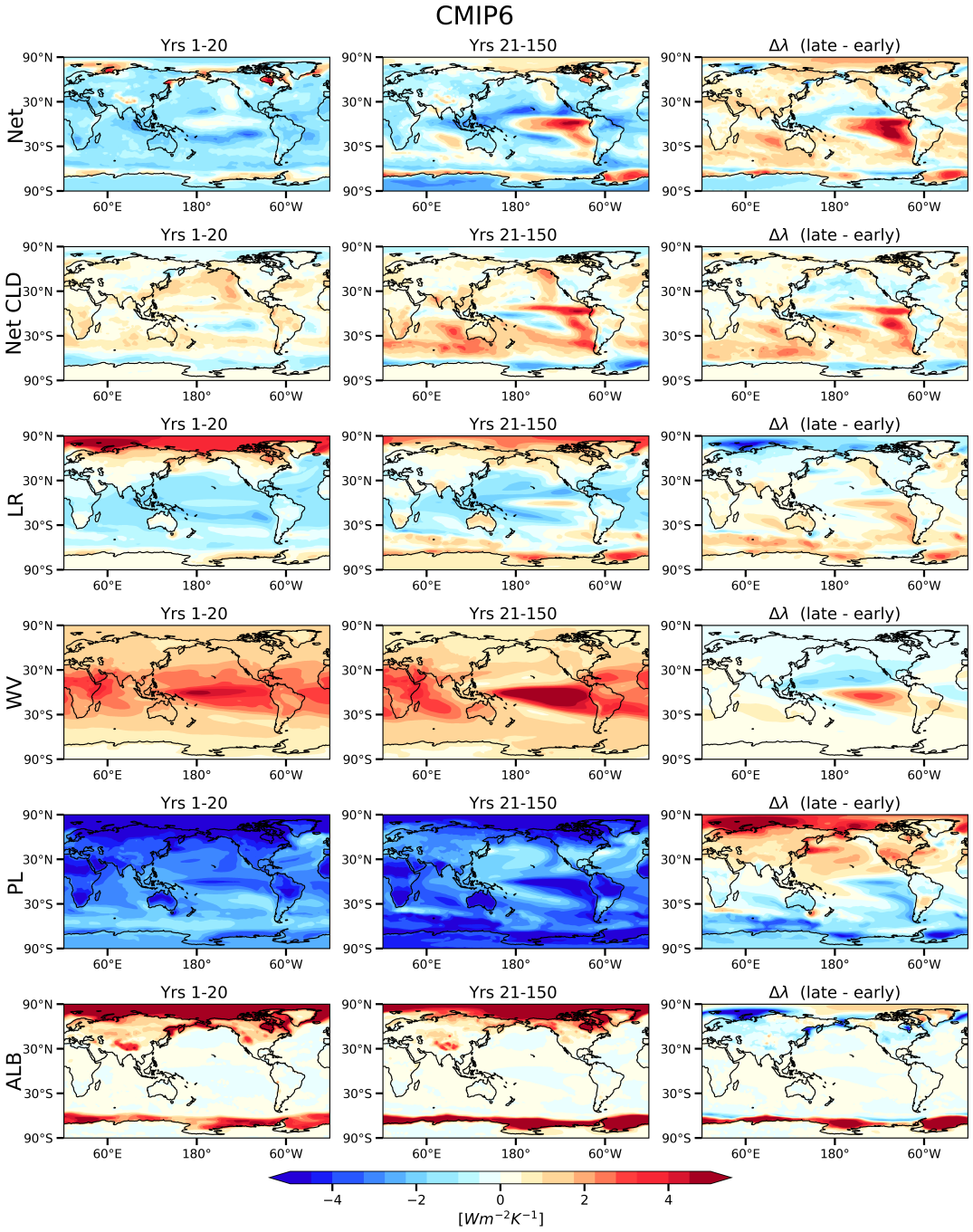

Figure 2.4: Same as Figure 2.3, except for CMIP6 ensemble means.

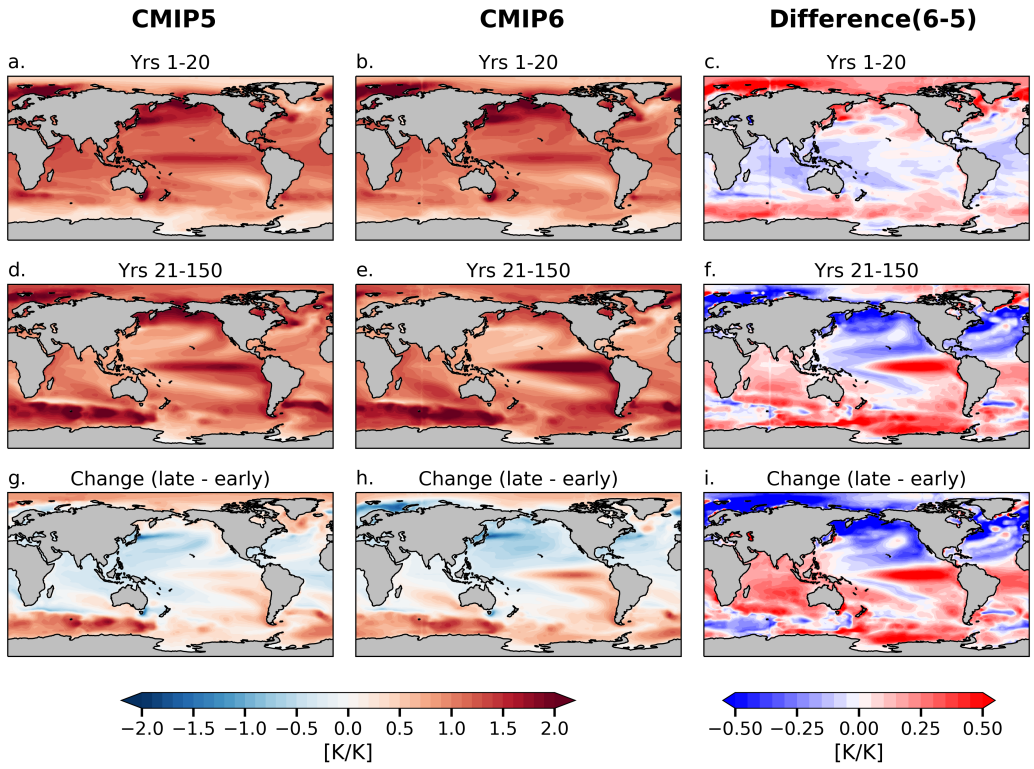

Figure 2.5: Spatial patterns of SST changes (SST^*) over (top to bottom) years 1-20, years 21-150, and their changes (late minus early), for (left) CMIP5 multi-model mean, (middle) CMIP6 multi-model mean, and (right) the difference (CMIP6 minus CMIP5). The values of SST* are calculated as the regression slope of local SST changes against global-mean SST changes, such that the global mean of panels (a, b, d, e) is one by construction. Note that the color scales in the left two columns and in the right column are different.

local state-dependence. Indeed, the relative warming in the Arctic over the first 20 years is stronger in CMIP6 than CMIP5 (Fig. 2.5c), but it becomes weaker over the following decades in CMIP6 relative to CMIP5 (Fig. 2.5f). As a result of this change in the rate of Arctic warming, the Arctic surface-albedo feedback on average weakens over time (i.e. negative $\Delta\lambda_{\mathrm{ALB}}$) within CMIP6 models (Fig. 2.4), which overcomes the positive $\Delta\lambda_{\mathrm{ALB}}$ arising from enhanced warming of the Southern Ocean on the slow timescale (Fig. 2.4 bottom row), leading to a slightly negative value of global-mean $\Delta\lambda_{\mathrm{ALB}}$ and an overall smaller value of global-mean $\Delta\lambda$ in CMIP6 models (Fig. 2.2).

2.4 The source of the inter-model spread in $\Delta\lambda$ across CMIP5 and CMIP6

We next move away from the multi-model mean perspective, to consider why individual models have different values of $\Delta\lambda$. We find it conceptually helpful to consider that radiative feedbacks and their changes may be influenced by both atmospheric model physics and SST patterns. To separate the two factors, we make use of radiative feedback "Green's functions" (Dong et al., 2019; Zhou et al., 2017), which will be introduced in subsection 2.4.1. In subsection 2.4.2 and subsection 2.4.3, we investigate the major source of the inter-model spread in $\Delta\lambda$ across the CMIP5 and CMIP6 models, respectively.

2.4.1 Green's functions

To separate the effect of SST patterns and the effect of model physics, we use radiative feedback Green's functions, as they predict the radiative response based solely on SST anomaly patterns, given the atmospheric physics of the parent model from which they were derived. The basis of a Green's function is a Jacobian matrix, representing the sensitivity of any regional response to regional SST anomalies, which consists of both local and nonlocal effects of changes in SST. The full Jacobian is calculated from a series of prescribed-SST simulations within an AGCM, each with a single patch of SST anomalies on the top of climatological SSTs. Then, convolving the Jacobian with a global SST anomaly pattern can predict the global response to the given SST pattern, based on the assumption of spatial linearity, which has been shown to be a good approximation (Dong et al., 2019; Zhou et al., 2017). Hence, applying the Green's functions linearly separates the differences in SST patterns and the differences in the sensitivity of radiative feedbacks on SST patterns.

Here we employ two Green's functions: one derived from the Community Atmosphere Model version 5 (CAM5) by Zhou et al. (2017), and one derived from CAM4 by Dong et al. (2019). The major difference between CAM4 and CAM5 Green's functions lies in the representation of cloud properties within the two models, which are reported to be more realistic in CAM5 (Kay et al., 2012), although both models exhibit large biases in the subtropical marine boundary layer cloud regimes. Throughout this study, we use the 2-dimensional global-mean Jacobians (denoted as $\mathbb{J}_X$, the sensitivity of a global-mean response

X to each grid of SST anomalies), for computational efficiency because our focus is on global-mean quantities. To compute feedback parameters from the Green's functions, we first reconstruct annual global-mean net TOA radiative response (R) and surface air temperature response (T) by convolving the Green's functions $\mathbb{J}_X$ with each model's annual-mean global SST change (SST($\mathbf{r}$)),

$$X = \mathbb{J}_X \cdot SST(\mathbf{r}), \tag{2.5}$$

where X can be any response (e.g. R, T), SST($\mathbf{r}$) denotes global pattern of SST anomalies. Then $\lambda_{1\text{-}20}$, $\lambda_{21\text{-}150}$, and $\Delta\lambda$ are calculated following the same regressions used to process model outputs. Note that the Green's function can only predict the TOA radiative response $R(=\lambda T)$, which is different to the net TOA radiation imbalance (N) in fully-coupled GCMs, because the latter includes the effective radiative forcing of CO_2 quadrupling F_{4x}: $N = F_{4x} + R$. Indeed, the effective radiative forcing also varies slightly across models; but it is abruptly imposed and held constant over time. Therefore, while radiative forcing matters for ECS itself, its absence does not cause any inconsistency in the estimates of feedbacks (defined as the regression slope in Gregory plots) between Green's functions and the GCM simulations.

2.4.2 Inter-model spread in $\Delta\lambda$ across CMIP5 models

We first show the comparison of feedbacks from CMIP5 GCMs and those reconstructed by the CAM4/CAM5 Green's functions (Fig. 2.6). Both Green's functions poorly capture $\lambda_{1\text{-}20}$ but approximately reproduce GCM values of $\Delta\lambda$, suggesting that $\lambda_{1\text{-}20}$ and $\Delta\lambda$ are governed by different processes. The failure of the Green's functions in reconstructing $\lambda_{1\text{-}20}$ may come from several factors, for example, the Green's functions fail to account for the radiative response to land warming which emerges generally on fast timescales. However, we favor the interpretation that the spread in $\lambda_{1\text{-}20}$ is primarily determined by each model's atmospheric physics (e.g., cloud parameterizations). Therefore, the radiative responses from each model cannot be captured by Green's functions derived from either CAM4 or CAM5, which have distinct atmospheric physics. On the other hand, the fact that both Green's functions more accurately reproduce $\Delta\lambda$ than $\lambda_{1\text{-}20}$, even though they are built from different

models, suggests that the spread in $\lambda_{1\text{-}20}$ arises primarily from the changes in SST patterns and is largely insensitive to model physics.

We next investigate what regions of SSTs drive the inter-model spread in $\Delta\lambda$ across the CMIP5 models. Previous studies have pointed out the importance of tropical warming through changing cloud and lapse-rate feedbacks. Zhou et al. (2016) proposed the role of the tropical eastern Pacific, where relative cooling in recent decades is thought to be responsible for driving an increase in local low cloud and a more-negative cloud feedback. Andrews and Webb (2017) further established a mechanism associated with east-west tropical Pacific SST gradient that governs the change in tropospheric stability, and therefore the change in low clouds and lapse rate. Silvers et al. (2018) highlighted changes in low clouds throughout the tropics beyond the traditional stratocumulus regimes in driving decadal variability of feedbacks over the historical period. Recently, Dong et al. (2019) proposed that $\Delta\lambda$ tracks the ratio of warming in the West Pacific warm-pool (WP) regions relative to warming in the rest of global ocean areas γ). Here we test this mechanism by examining the correlation of $\Delta\lambda$ against the proposed WP warming ratio change ($\Delta\lambda$) across models.

To calculate $\Delta\gamma$ for all CMIP5 and CMIP6 models, we define WP regions in this study as grid cells within 30°S–30°N, 30°E–160°W that have an upward vertical velocity at 500hPa (ω500) in the piControl simulation. Unlike the fixed rectangular area in the west Pacific used in Dong et al. (2019), this updated metric takes into account mean-state biases, ensuring that in each model the WP regions capture the radiative responses in regions of deep convection. Note that results using the fixed region in Dong et al. (2019) are similar to those shown here. We also simplify γ to be the WP SST warming relative to global-mean surface air temperature changes, calculated as the regression slope of the averaged SST over the selected WP regions against global-mean T, over the two time periods used throughout this study (years 1-20 for $\gamma_{1\text{-}20}$, years 21-150 for $\gamma_{21\text{-}150}$, and $\Delta\gamma = \gamma_{21\text{-}150} - \gamma_{1\text{-}20}$).

Fig. 2.7a shows that $\Delta\lambda$ is well correlated with $\Delta\gamma$ for CMIP5 models (with $r^2 = 0.63$). Although many approximations are made in the derivation (Dong et al., 2019), the simple metric $\Delta\gamma$, which includes no information about radiative response, explains over 60% of the variance in CMIP5 $\Delta\lambda$. The physical mechanism, as discussed in Dong et al. (2019), is the preeminent impact of WP warming on global TOA radiation change via deep convection.

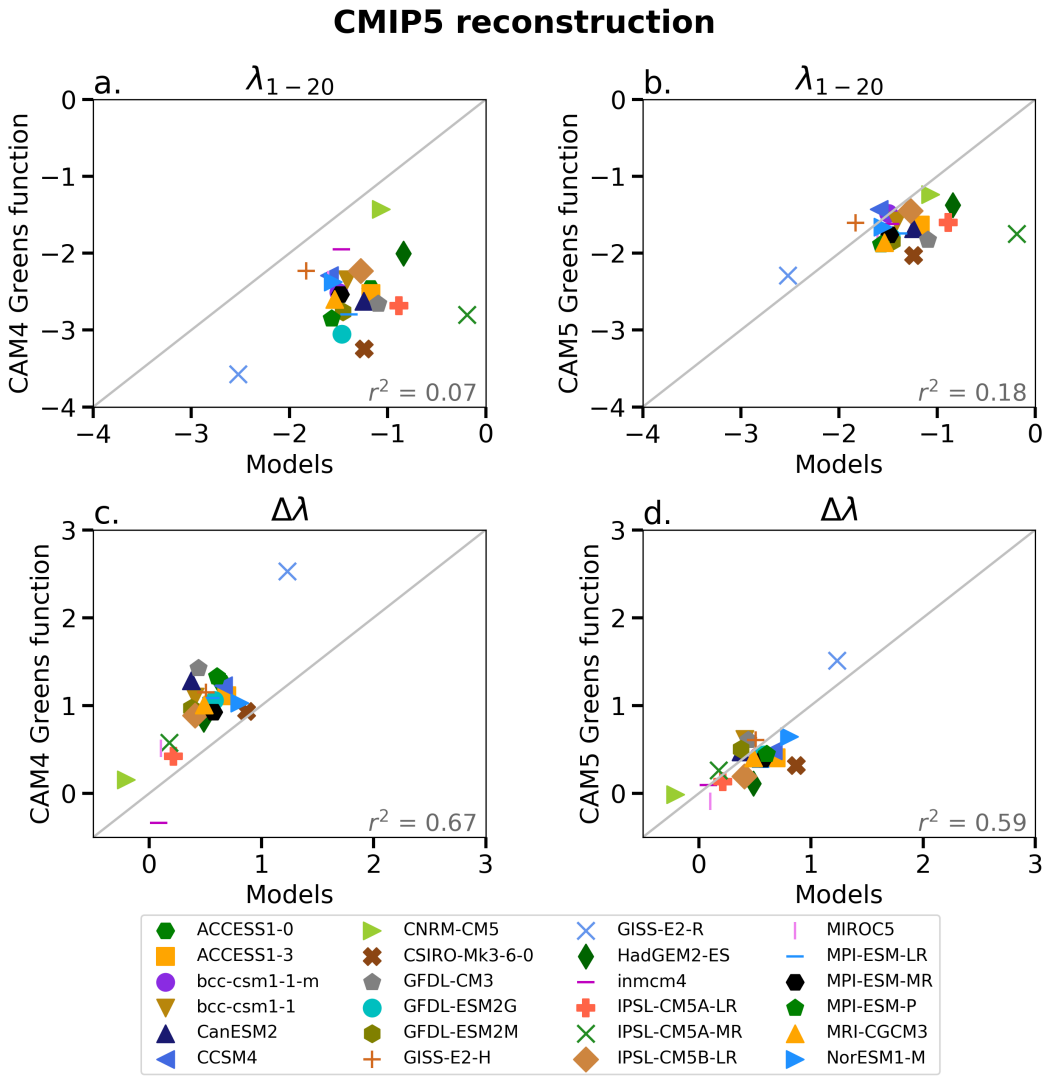

Figure 2.6: Comparison of (top) $\lambda_{1\text{-}20}$ and (bottom) $\Delta\lambda$ from CMIP5 models and those from (left) CAM4 Green's function, (right) CAM5 Green's function, respectively. Gray lines are $y = x$ reference line. Variance explained is noted in the bottom right corner of each panel.

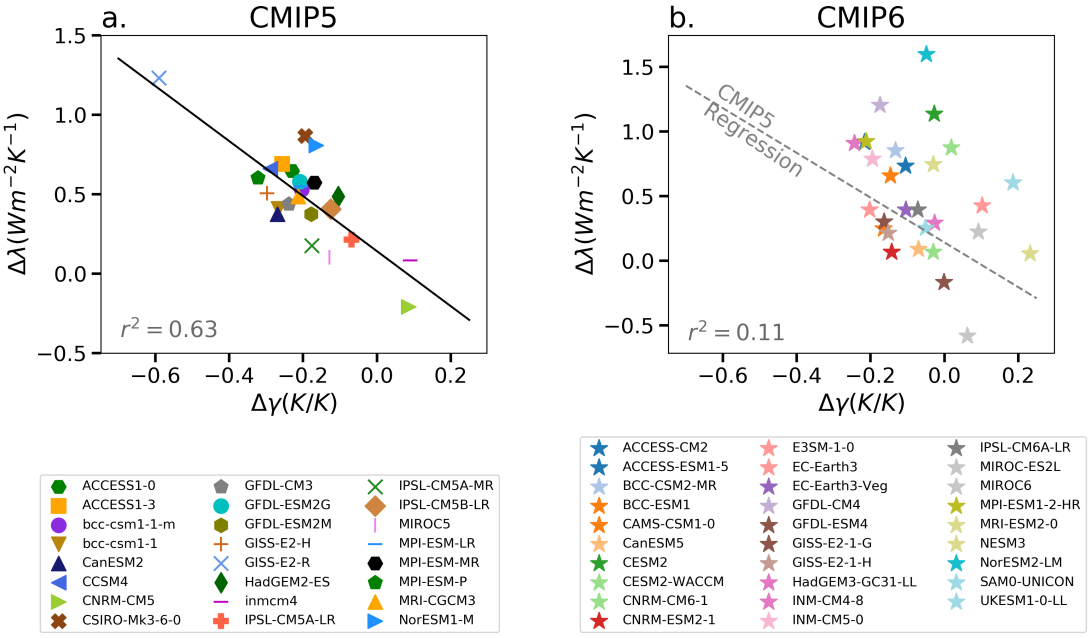

Figure 2.7: The relation between the change in net feedback ($\Delta\lambda$) and the change in the West Pacific warm-pool warming ratio ($\Delta\gamma$), for (left) CMIP5 models and (right) CMIP6 models. The linear fit for CMIP5 models is plotted as the black line in the left panel, and the grey dashed line in the right panel. Variance explained is noted in the lower left corner of each panel.

Over the WP regions, where the surface is tightly coupled to the free troposphere by deep convection, surface warming directly enhances upper tropospheric warming. This leads to a stronger negative lapse-rate feedback and a more-negative cloud feedback over low-cloud regions caused by increased lower tropospheric stability, which together promotes a more efficient radiative damping at TOA. On the other hand, the weaker coupling between surface and upper troposphere in all other regions results in a weak TOA radiation response to surface warming. This leads to a weaker negative lapse-rate feedback, and a more-positive low-cloud feedback, hence, resulting in an inefficient radiative damping (see Dong et al. 2019, Figs. 2.4, 2.5). The key importance of warm pool warming for TOA radiation changes is also supported by observational evidence (Ceppi and Gregory, 2017; Fueglistaler, 2019; Zhou et al., 2016).

To further demonstrate the proposed mechanism, we select three representative models that have large positive $\Delta\lambda$ (GISS-E2-R), small positive $\Delta\lambda$ (IPSL-CM5B-LR), and small negative $\Delta\lambda$ (CNRM-CM5), respectively (Fig. 2.8). $\Delta\lambda$ is demonstrated as the degree of curvature in the Gregory plots for each model (Figs. 2.8 a-c). We then show their SST warming patterns defined as local SST changes regressed against global-mean SST changes, denoted by SST* (Figs. 2.8 d-l). In this context, values above 1 (in red) indicate local warming exceeding the global-mean warming in the given period, and values below 1 (in blue) indicate local warming weaker than the global-mean warming. In GISS-E2-R, the warm-pool regions warm up relatively quickly during the first 20 years, but warming in the warm pool does not keep pace with warming in other oceans (e.g. the Southern Ocean) over the last 130 years. This sharp transition of surface warming from tropical ascent regions to all other regions is responsible for the large $\Delta\lambda$. In IPSL-CM5B-LR, the WP region does not warm substantially faster than the global average warming on the fast timescale, so that the change in the relative warming over WP regions is weaker, leading to a smaller $\Delta\lambda$. In CNRM-CM5, the WP region warms relatively fast on the longer timescales, leading to a nearly zero change in WP region in contrast to the other two models, driving a negative $\Delta\lambda$. This comparison shows that the CMIP5 values of $\Delta\lambda$ can be well characterized by the ratio of warm-pool to global-mean warming (Fig. 2.7a), suggesting an important role of tropical convective regions in modulating the strength of radiative feedbacks in CMIP5.

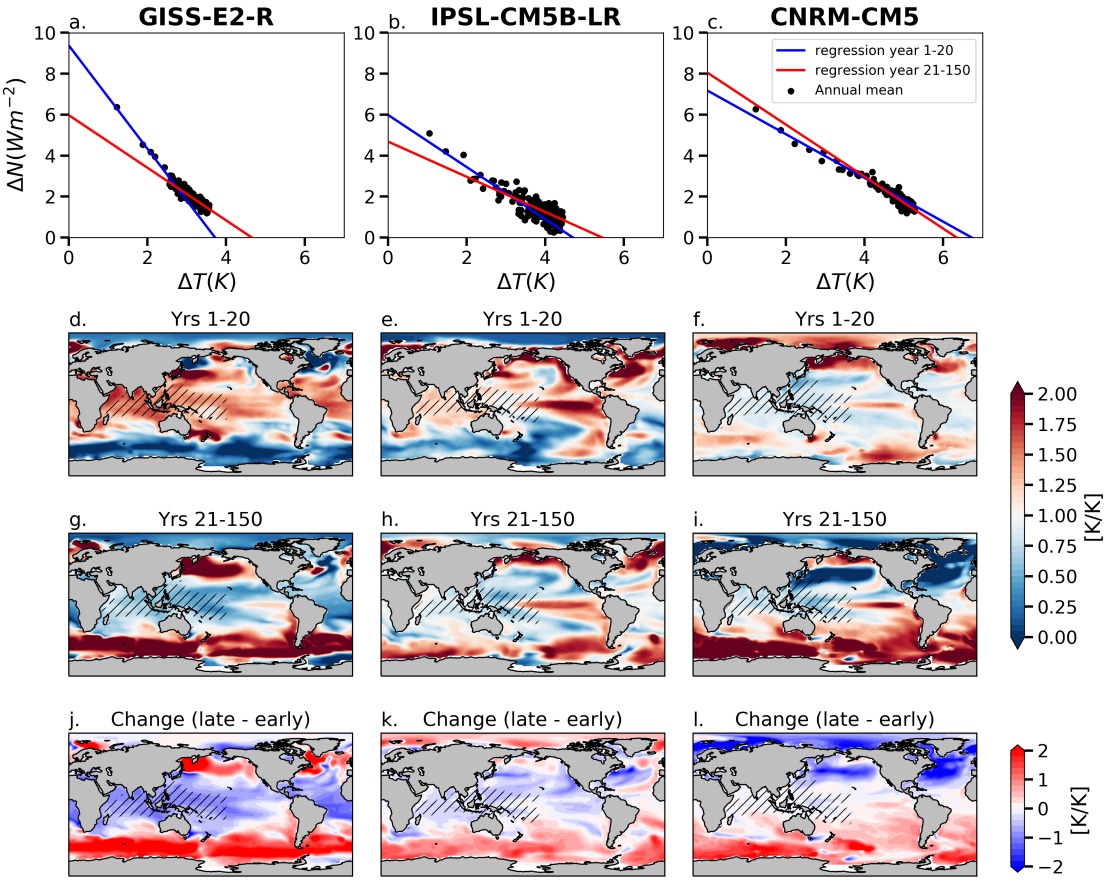

Figure 2.8: Gregory plots (top) and patterns of SST changes (bottom three rows) for (left) GISS-E2-R, (middle) IPSL-CM5B-LR, and (right) CNRM-CM5. (a – c) Colored lines show regression fits for years 1-20 (blue) and for years 21-150 (red). (d – i) plots show the regression slope of local SST changes against global-mean SST changes over (d –f) years 1-20, (g-i) years 21- 150, and (j-i) the change between the two time periods (later minus early). The hatchings highlight the warm-pool ascent regions in each model.

2.4.3 Inter-model spread in $\Delta\lambda$ across CMIP6 models

For CMIP6 models, we first repeat the analysis applying the WP warming ratio. Interestingly, the above theory does not seem to hold as well for CMIP6 models (Fig. 2.7b), suggesting that the $\Delta\lambda$ spread in the latest models may not directly trace to relative warm-pool warming. One may ask whether this is because the deep convection in other regions (e.g. Atlantic Ocean warm-pool regions) carry more weight in the CMIP6 ensemble. To identify where is the key region for driving feedback changes, we regress global-mean $\Delta\lambda$ onto local ΔSST^* (the change in the relative warming rate from fast to slow timescale) across CMIP5 and CMIP6 models, respectively, and evaluate the local correlation coefficient (r). Note that $SST^*$is calculated as the local SST change relative to global-mean SST change, and Δ is defined as the late period (years 21-150) minus the early period (years 1-20).

The resulting correlation maps (r) are shown in Fig. 2.9. The positive correlation indicates that models that have stronger positive global-mean $\Delta\lambda$ tend to show a locally delayed warming as approaching to equilibrium, whereas the negative correlation indicates that models that have stronger positive global-mean $\Delta\lambda$ tend to show a local warming predominately on the fast timescale. The magnitude of correlation coefficient illustrates the degree to which the inter-model spread in $\Delta\lambda$ correlates with the differences in local warming rates. For example, Fig. 2.9a shows a strong negative correlation over Indo-Pacific deep convective regions, which indicates that in the CMIP5 models, $\Delta\lambda$ is primarily governed by the difference in the relative warming in the West Pacific warm-pool regions where greater warming on the fast timescale gives rise to a stronger positive $\Delta\lambda$. This is achieved mostly through $\Delta\lambda_{\mathrm{CLD}}$ (Fig. 2.9c) and $\Delta\lambda_{\mathrm{LR}}$ (Fig. 2.9g). However, the results from the CMIP6 models highlight the tropical Indian ocean, the equatorial eastern Pacific, and the SH midlatitudes (Fig. 2.9b), which are mostly reflected in the pattern of $\Delta\lambda_{\mathrm{CLD}}$ (Fig. 2.9d). This comparison suggests that the CMIP5 values of $\Delta\lambda$ may be primarily dominated by surface warming in the broad tropical convective regions, whereas the CMIP6 values of $\Delta\lambda$ may be influenced more by surface warming in the tropical subsidence regions and extratropics. Indeed, we found that about half of the variance in $\Delta\lambda$ in CMIP5 ensemble

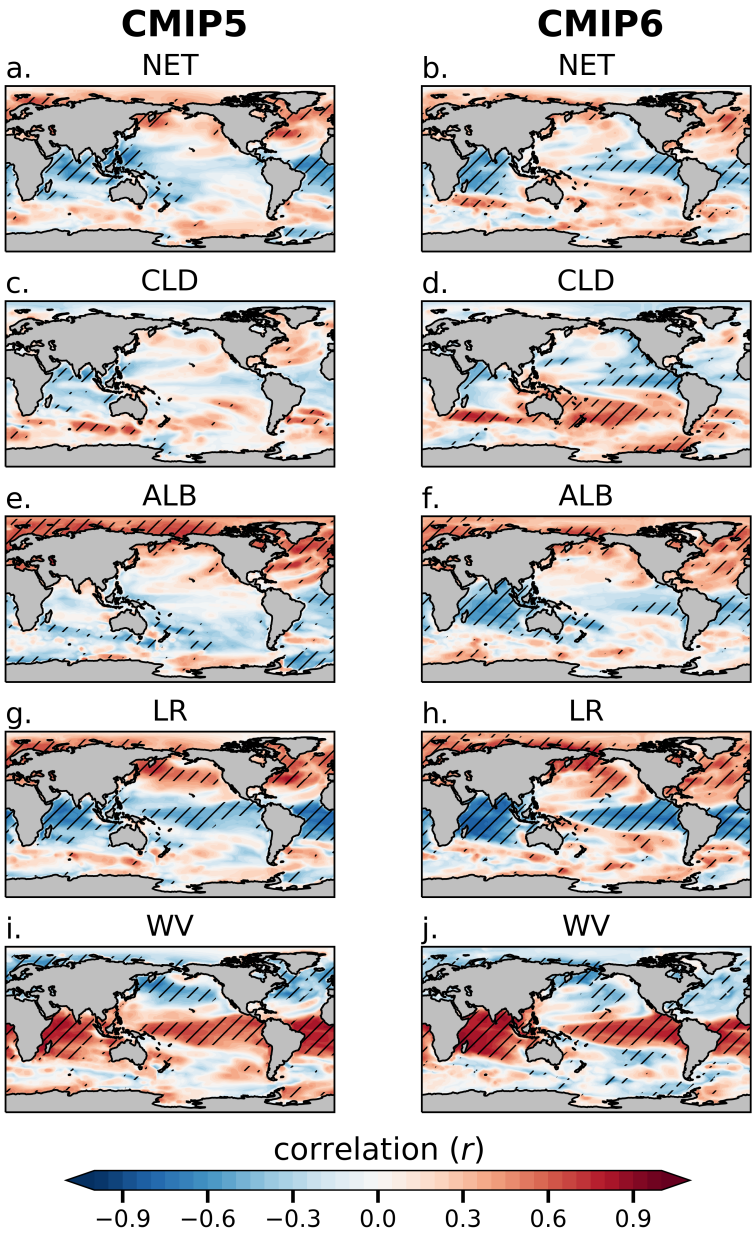

Figure 2.9: Correlation coefficients (r) for local regression of global-mean $\Delta\lambda$ against local ΔSST^* (local SST warming rate relative to global-mean SST change) across (left) CMIP5 models and (right) CMIP6 models. Top to bottom: net $\Delta\lambda$, cloud $\Delta\lambda$, surface-albedo $\Delta\lambda$, lapse rate $\Delta\lambda$, and water vapor $\Delta\lambda$. Hatchings mark grids where correlations are significant (i.e., p¡0.05).

can be explained by the change in the estimated inversion strength (EIS) per unit of global warming, whereas the variance in $\Delta\lambda$ explained by the EIS change in CMIP6 ensemble is slightly decreased ($r^2 = 0.4$). Moreover, we found that both Green's functions fail to reproduce CMIP6 $\Delta\lambda$ (not shown), even though they largely capture $\Delta\lambda$ in CMIP5 models (Figs. 2.6c, d). Multiple factors may contribute to the inability of the CAM4/CAM5 Green's functions to capture the behavior of CMIP6 models, and we consider two of them here.

Firstly, we consider the possibility that the CAM4/CAM5 Green's functions cannot capture feedback changes in the CMIP6 models, even assuming that the radiative response to SST patterns remain linear (section 2.4.1). That is, the CMIP6 models may be systematically different from the CMIP5 models from which the Green's functions are built. One example is the modifications made to extratropical clouds in CMIP6 models, whose feedbacks have strengthened in CMIP6 owing to changes in their sensitivities to local environmental conditions (Zelinka et al., 2020). These changes may give rise to a different dependence of cloud feedbacks on SST pattern, presumably with stronger cloud radiative response to Southern Ocean warming. In this case, the global TOA radiation change may no longer be dominated by the tropical warm-pool warming as seen in CAM4 Green's function for example (see Dong et al. 2019 Fig. 2.11), but could instead also be strongly influenced by the Southern Ocean warming. As a result, the delayed Southern Ocean warming would yield a stronger pattern effect on the cloud feedback (i.e. a greater positive $\Delta\lambda_{\mathrm{CLD}}$). Indeed, the Southern Ocean is highlighted in the CMIP6's result in Fig. 2.9d with a stronger positive correlation, suggesting a stronger sensitivity of cloud feedback on the Southern Ocean warming rate. If this is the case, new Green's functions with up-to-date GCMs may better capture the causes of feedback changes in CMIP6 models.

Apart from extratropical clouds, changes in CMIP6 models may also yield a different radiative response to the equatorial eastern Pacific, where delayed warming seems to drive a negative $\Delta\lambda$ corresponding to a strengthening of global-mean (negative) feedback over time (Fig. 2.9b). However, there also remains a possibility that the correlation between the equatorial eastern Pacific warming and $\Delta\lambda$ is not causal but comes about through correlations between the eastern Pacific and SH extratropical warming rates, for instance.

Specific mechanisms need to be further uncovered.

A second possibility comes from the potential nonlinear state-dependence of feedbacks in the CMIP6 models, in which case the Green's functions can no longer apply as they rely on linear estimation. In particular, we consider a well-documented nonlinearity in the extratropical mixed-phase cloud feedback. The negative mixed-phase cloud feedback arises from the brightening of the clouds as they become increasingly composed of liquid droplets with warming. Therefore, it depends on the mean-state of ice/liquid fraction of the clouds, with more ice in the initial state leading to a stronger negative-feedback with warming (McCoy et al., 2015; Storelvmo et al., 2015; Tsushima et al., 2006). Many CMIP6 models now have higher climatological cloud liquid water fractions, in better agreement with observations (Bodas-Salcedo et al., 2019; Gettelman et al., 2019; Zelinka et al., 2020). Bjordal et al. (2020) shows that in CESM2, with the inclusion of a new mixed-phase ice nucleation scheme, the negative mixed-phase cloud feedback weakens with warming from the first 20 years to the last 20 years of abrupt4xCO2 simulation, particularly over the Southern Ocean, as the amount of ice decreases allowing for no further phase change to happen (see their Fig. 2.3). This weakening towards longer timescales in their simulations leads to a positive $\Delta\lambda_{\mathrm{CLD}}$ over the Southern Ocean, which is primarily driven by the nonlinear state-dependence rather than by the pattern effect. If this case holds more generally across the CMIP6 models, the nonlinear state-dependence of $\Delta\lambda_{\mathrm{CLD}}$ on the Southern Ocean warming may never be captured by any Green's functions, as the method relies on linear estimation.

In summary, we found the CMIP5 and CMIP6 ensembles on average highlight different regions where surface warming can influence the magnitude of global-mean $\Delta\lambda$ (Fig. 2.9). In CMIP5, inter-model differences in $\Delta\lambda$ are overall driven by inter-model differences in the surface warming rates over the West Pacific warm-pool region, where surface warming has strong remote impact on global TOA radiation changes (Dong et al., 2019). In CMIP6, inter-model differences in $\Delta\lambda$ (and the cloud component $\Delta\lambda_{\mathrm{CLD}}$ in particular) appear to have more contributions from SH extratropical warming and tropical eastern Pacific warming. Specific physical mechanisms are under investigation. Here we speculate that the stronger sensitivity of feedbacks on the delayed extratropical warming may result either from a stronger pattern effect (stronger cloud radiative response to surface warming in this region),

or from a nonlinear state-dependence of extratropical cloud feedback on the mean-state of the liquid fraction in the clouds.

2.5 Conclusion

In this study, we investigated the changes in radiative feedbacks over time and their contributions to climate sensitivity from abrupt4xCO2 simulations within 24 CMIP5 GCMs and 29 CMIP6 models. Comprehensive comparisons were made between the two CMIP generations and between individual models. To examine the time-variation of feedbacks, we derived feedback parameters from the Gregory regressions between the net TOA radiation imbalance and surface air temperature change over years 1–20 as $\lambda_{1\text{-}20}$ and years 21–150 as $\lambda_{21\text{-}150}$, and use $\Delta\lambda(= \lambda_{21\text{-}150}–\lambda_{1\text{-}20})$ to represent the feedback changes over time.

We found that on average the effective ECS derived from the regression is higher and $\Delta\lambda$ is smaller in CMIP6 relative to CMIP5. We then evaluated the correlation between $ECS_{21\text{-}150}$ (derived from years 21-150; featuring long-term response) and $ECS_{1\text{-}20}$ (derived from years 1-20; featuring fast response governed primarily by $\lambda_{1\text{-}20}$). The correlation (r^2) is 0.69 for CMIP5 and 0.70 for CMIP6, suggesting that the variance in ECS (as estimated by $ECS_{21\text{-}150}$) is dominated by the differences in radiative response on the fast timescale, rather than the differences in $\Delta\lambda$. This also explains the fact that a greater $\Delta\lambda$ generally leads to a greater effective ECS within individual climate models, yet the higher effective ECS in the CMIP6 models occurs despite smaller $\Delta\lambda$. We also compared the ECS-to-ECS_{hist} ratio between CMIP5 and CMIP6, where ECS_{hist} is estimated from years 2-50 of abrupt4xCO2 simulations as an analog for historical warming. We found the difference in feedback estimates between the short-term abrupt4xCO2 (as the proxy for historical energy budget) and the long-term abrupt4xCO2 (as the proxy for equilibrium state) is on average smaller in CMIP6, and the CMIP6-mean ECS-to-ECS_{hist} ratio is also slightly reduced, on average, relative to CMIP5, suggesting a weaker forced pattern effect in CMIP6 abrupt4xCO2 simulations. Further work employing fully-coupled historical simulation and RFMIP simulations are expected to provide a more accurate estimate on historical energy budget and the role of unforced pattern effect by internal variability over the historical period.

Although the spread in $\Delta\lambda$ contributes less to the spread in ECS than does atmospheric model physics, understanding the magnitude of $\Delta\lambda$ and the pattern effect is still of a great importance to constrain ECS on longer timescales. By comparing the multi-model mean $\Delta\lambda$ in the CMIP5 and CMIP6 models, we see great similarities in the spatial patterns of $\Delta\lambda$, highlighting the cold tongue regions with delayed warming. An overall smaller ensemble-mean $\Delta\lambda$ in the CMIP6 models is primarily due to the difference in surface-albedo feedback over the Arctic. While the positive Arctic surface-albedo feedback generally strengthens with time in CMIP5, it weakens over time in CMIP6, compensating the global-mean change in surface-albedo feedback. This is caused primarily by changes in surface warming patterns in CMIP6, which feature rapid Arctic warming on the fast timescale followed by slow Arctic warming on the slow timescale. But we caution that the differences between ensemble-mean $\Delta\lambda$ are not statistically significant given the large spread across models, and the results may be subject to change as more models come in.

Because both model physics and surface warming patterns are important for driving $\Delta\lambda$, we employ Green's functions to isolate their contributions and investigate why individual models produce different $\Delta\lambda$. The Green's functions used in this study are derived from two GCMs, which intrinsically represent the given model physics of CAM4 or CAM5 but can be independently applied to different SST anomaly patterns. When applied to the CMIP5 models, the Green's functions reproduce $\Delta\lambda$ well but cannot capture $\lambda_{1\text{-}20}$, suggesting that $\Delta\lambda$ is primarily set by the differences in warming patterns, while $\lambda_{1\text{-}20}$ is presumably determined by the differences in model physics. Building upon Dong et al. (2019)), the spread in $\Delta\lambda$ is found to be well correlated with the change in the warm-pool warming ratio, defined as the relative ocean warming from warm-pool ascent regions to global-mean surface air warming. Across CMIP5 models, this simple metric is able to explain over 60% variance of $\Delta\lambda$. Models showing greater $\Delta\lambda$ generally have West Pacific warm-pool regions warming up more quickly than the rest of world oceans on the fast timescale, but more slowly on longer timescales. This transition, on the other hand, is less significant in models that produce smaller $\Delta\lambda$. Regression of global-mean $\Delta\lambda$ against local warming rates also highlights the West Pacific warm-pool regions as the dominant control driving $\Delta\lambda$ variance across CMIP5 models, consistent with recent observations identifying the warm-pool as a

key region controlling global radiation (e.g., Fueglistaler 2019).

However, the correlation analysis across CMIP6 models show a different spatial distribution, with SH extratropics and equatorial eastern Pacific being highlighted in addition to the West Pacific warm-pool regions, suggesting that the CMIP6 values of $\Delta\lambda$ may not be dominated by tropical warm-pool warming. The specific mechanism needs to be further uncovered; we speculate here that it may be partly attributable to a stronger sensitivity of extratropical clouds to surface warming. Future studies employing Green's function approach built from the CMIP6 models may bring more insights on investigating the pattern effect within the latest generation of GCMs, but will have limitations in the case that nonlinear state-dependence of feedbacks also contributes to the changes in feedbacks with time.

Table 2.1: Estimates of feedback parameter and effective climate sensitivity from abrupt4xCO2 simulations for the CMIP6 GCMs and their multi-model mean. Left to right: feedback parameter over the fast time scale ($\lambda_{1\text{-}20}$); feedback parameter over the longer time scale ($\lambda_{21\text{-}150}$); feedback evolution ($\Delta\lambda = \lambda_{21\text{-}150} - \lambda_{1\text{-}20}$); effective climate sensitivity from regressions over years 1-20 ($ECS_{1\text{-}20}$); effective climate sensitivity from regressions over years 21-150 ($ECS_{21\text{-}150}$). The unit for feedback parameters and feedback change is $Wm^{-2}K^{-1}$; for $ECS_{1\text{-}20}$ and $ECS_{21\text{-}150}$, the unit is K. All regressions are calculated using the ordinary least squares regression method.

CMIP6 MODEL	$\lambda_{1\text{-}20}$	$\lambda_{21\text{-}150}$	$\Delta\lambda$	$ECS_{1\text{-}20}$	$ECS_{21\text{-}150}$
ACCESS-CM2	-1.1	-0.5	0.6	3.75	5.41
ACCESS-ESM1-5	-1.14	-0.42	0.73	3.07	4.93
BCC-CSM2-MR	-1.26	-0.63	0.64	2.85	3.5
BCC-ESM1	-1.25	-0.74	0.51	2.78	3.5
CAMS-CSM1-0	-1.94	-1.71	0.24	2.23	2.31
CESM2-WACCM	-1.11	-0.48	0.63	3.65	5.49
CNRM-CM6-1	-0.92	-0.81	0.1	4.29	4.76
CNRM-ESM2-1	-0.49	-0.58	-0.09	5.7	4.91
CanESM5	-0.69	-0.62	0.08	5.44	5.75
E3SM-1-0	-0.77	-0.47	0.3	4.78	5.77
EC-Earth3-Veg	-1.12	-0.7	0.42	3.57	4.45
EC-Earth3	-1.12	-0.7	0.42	3.57	4.45
GFDL-CM4	-1.44	-0.59	0.85	2.94	4.4
GFDL-ESM4	-1.36	-1.46	-0.1	2.71	2.63
GISS-E2-1-G	-1.46	-1.2	0.26	2.74	2.87
GISS-E2-1-H	-1.26	-1.08	0.17	2.95	3.15
HadGEM3-GC31-LL	-0.82	-0.58	0.24	4.72	5.73
INM-CM4-8	-1.8	-0.98	0.82	1.74	1.91
INM-CM5-0	-1.7	-1.09	0.6	1.85	2.02
IPSL-CM6A-LR	-1.01	-0.65	0.36	3.86	4.76
MIROC-ES2L	-1.48	-1.94	-0.46	2.69	2.53
MIROC6	-1.63	-1.44	0.19	2.4	2.59
MPI-ESM1-2-HR	-1.51	-0.81	0.7	2.77	3.34
MRI-ESM2-0	-1.45	-0.85	0.6	2.75	3.41
NESM3	-0.94	-0.79	0.15	4.27	4.72
NorESM2-LM	-2.06	-0.83	1.23	2.24	2.98
SAM0-UNICON	-1.16	-0.74	0.42	3.6	4.19
UKESM1-0-LL	-0.79	-0.63	0.17	4.84	5.49
Mean (median)	-1.24 (-1.19)	-0.84 (-0.74)	0.4 (0.42)	3.4 (3.07)	4.08 (4.4)
Standard deviation	0.37	0.38	0.34	1.01	1.27

Table 2.2: Same as Table 2.1, except for the CMIP5 models.

CMIP5 MODEL	$\lambda_{1\text{-}20}$	$\lambda_{21\text{-}150}$	$\Delta\lambda$	$ECS_{1\text{-}20}$	$ECS_{21\text{-}150}$
ACCESS1-0	-1.15	-0.57	0.57	3.1	4.3
ACCESS1-3	-1.17	-0.5	0.67	2.92	4.36
bcc-csm1-1	-1.49	-0.87	0.62	2.54	3
bcc-csm1-1-m	-1.42	-0.91	0.51	2.71	3.05
CanESM2	-1.23	-0.89	0.33	3.4	3.85
CCSM4	-1.57	-0.89	0.69	2.6	3.2
CNRM-CM5	-1.06	-1.24	-0.19	3.38	3.18
CSIRO-Mk3-6-0	-1.25	-0.4	0.85	2.84	5.03
GFDL-CM3	-1.19	-0.61	0.58	3.11	4.3
GFDL-ESM2G	-1.51	-0.64	0.87	2.32	3.02
GFDL-ESM2M	-1.48	-0.99	0.49	2.42	2.68
GISS-E2-H	-1.86	-1.4	0.46	2.21	2.39
GISS-E2-R	-2.47	-1.3	1.17	1.88	2.31
HadGEM2-ES	-0.83	-0.34	0.49	4.01	6.02
inmcm4	-1.5	-1.26	0.23	2.04	2.16
IPSL-CM5A-LR	-0.89	-0.62	0.27	3.77	4.44
IPSL-CM5A-MR	-0.91	-0.62	0.29	3.85	4.52
IPSL-CM5B-LR	-1.29	-0.79	0.5	2.35	2.79
MIROC5	-1.66	-1.3	0.36	2.64	2.84
MPI-ESM-LR	-1.38	-0.87	0.51	3.32	3.89
MPI-ESM-MR	-1.48	-0.88	0.59	3.16	3.73
MPI-ESM-P	-1.57	-0.96	0.61	3.13	3.68
MRI-CGCM3	-1.56	-1.13	0.43	2.31	2.66
NorESM1-M	-1.61	-0.77	0.85	2.34	3.18
Mean(median)	-1.40(-1.45)	-0.86(-0.88)	0.53(0.51)	2.85(2.78)	3.52(3.19)
Standard deviation	0.35	0.3	0.27	0.58	0.95

Table 2.3: Estimates of ECS_{hist}, ECS-to-ECS_{hist} ratio and λ' (λ change from historical period to equilibrium) for individual CMIP6 models and ensemble-means of CMIP5 and CMIP6, to be compared with Table S2 in Lewis and Curry (2018). For ECS-to-ECS_{hist} ratio and λ', the results shown are calculated with the values of effective ECS derived from regressions over years 21-150 (or years 1-150), using the Deming regression method.

		ECS-to-ECS_{hist} ratio	λ'
CMIP6 MODEL	ECS_{hist}	yrs 21-150 (yrs 1-150)	yrs 21-150 (yrs 1-150)
ACCESS-CM2	4.05	1.28 (1.13)	0.22(0.12)
ACCESS-ESM1-5	3.13	1.41 (1.19)	0.31 (0.17)
BCC-CSM2-MR	2.81	1.06 (1.04)	0.06 (0.05)
BCC-ESM1	3.05	1.07 (1.05)	0.07 (0.05)
CAMS-CSM1-0	2.19	0.98 (1.02)	-0.04 (0.03)
CESM2	4.16	1.4 (1.21)	0.32 (0.2)
CESM2-WACCM	3.9	1.32 (1.17)	0.25 (0.15)
CNRM-CM6-1	4.72	0.96 (1.02)	-0.03 (0.02)
CNRM-ESM2-1	4.52	0.91 (1.02)	-0.06 (0.01)
CanESM5	5.33	1.05 (1.04)	0.03 (0.03)
E3SM-1-0	4.91	1.1 (1.07)	0.06 (0.04)
EC-Earth3	3.87	1.09 (1.1)	0.08 (0.09)
EC-Earth3-Veg	3.91	1.08 (1.09)	0.07 (0.08)
GFDL-CM4	3.16	1.12 (1.14)	0.13 (0.16)
GFDL-ESM4	2.55	0.88 (0.98)	-0.2 (-0.02)
GISS-E2-1-G	2.57	1 (1.03)	0 (0.04)
GISS-E2-1-H	2.95	0.99 (1.02)	-0.01 (0.03)
HadGEM3-GC31-LL	5.24	1.08 (1.05)	0.06 (0.04)
INM-CM4-8	1.74	1.05 (1.04)	0.09 (0.07)
INM-CM5-0	1.84	1 (1.02)	0 (0.04)
IPSL-CM6A-LR	4.31	1.01 (1.02)	0.01 (0.02)
MIROC-ES2L	2.62	0.88 (1.02)	-0.23 (-0.04)
MIROC6	2.37	0.95 (1.03)	-0.09 (0.05)
MPI-ESM1-2-HR	2.63	1.18 (1.11)	0.23 (0.15)
MRI-ESM2-0	2.68	1.09 (1.11)	0.11 (0.13)
NESM3	4.78	0.91 (0.96)	-0.08 (-0.04)
NorESM2-LM	1.88	1.1 (1.16)	0.22 (0.34)
SAM0-UNICON	3.38	1.05 (1.06)	0.06 (0.06)
UKESM1-0-LL	5.12	1.06 (1.04)	0.05 (0.03)
CMIP6 mean	3.46	1.07 (1.07)	0.06 (0.07)
CMIP6 std	1.08	0.13 (0.06)	0.13 (0.08)
CMIP5 mean	2.807	1.095 (1.073)	0.092 (0.086)
CMIP5 std	0.59	0.134 (0.063)	0.141 (0.069)

Chapter 3

BIASED ESTIMATES OF EQUILIBRIUM CLIMATE SENSITIVITY AND TRANSIENT CLIMATE RESPONSE DERIVED FROM HISTORICAL CMIP6 SIMULATIONS

(This chapter in currently in press as: Dong, Y., Armour, K. C., Proistosescu, C., Andrews, T., Battisti, D. S., Forster, P. M., et al. (2021). Biased estimates of Equilibrium Climate Sensitivity and Transient Climate Response derived from historical CMIP6 simulations. Geophysical Research Letters, 48, e2021GL095778. https://doi.org/10.1029/2021GL095778)

Abstract

This study assesses the effective climate sensitivity (EffCS) and transient climate response (TCR) derived from global energy budget constraints within historical simulations of 8 CMIP6 global climate models (GCMs). These calculations are enabled by use of the Radiative Forcing Model Intercomparison Project (RFMIP) simulations, which permit accurate quantification of the radiative forcing. Long-term historical energy budget constraints generally underestimate EffCS from CO_2 quadrupling and TCR from CO_2 ramping, owing to changes in radiative feedbacks and changes in ocean heat uptake efficiency. Atmospheric GCMs forced by observed warming patterns produce lower values of EffCS that are more in line with those inferred from observed historical energy budget constraints. The differences in the EffCS estimates from historical energy budget constraints of models and observations are traced to discrepancies between modeled and observed historical surface warming patterns.

3.1 Introduction

Equilibrium climate sensitivity (ECS) and transient climate response (TCR) are two fundamental metrics for evaluating climate change projections. ECS represents the *equilibrium* global surface warming in response to a doubling of atmospheric CO_2 concentration

relative to pre-industrial levels. Although idealized, ECS has been found to explain most of the spread in projected 21st century global temperature change under realistic emission scenarios (Grose et al., 2018; Sherwood et al., 2020). TCR represents the *transient* surface warming at the time of CO_2 doubling under an idealized 1% per year CO_2 increase. As a measure of transient response, TCR is better constrained and is also informative about the projected degree of global warming in the coming century.

In principle, ECS and TCR can be inferred from the global energy balance framework (Gregory et al., 2004):

$$\Delta N = \Delta F + \lambda \Delta T, \tag{3.1}$$

where ΔN is the global-mean top-of-atmosphere (TOA) radiation anomaly (approximately equal to ocean heat uptake), ΔF is the effective radiative forcing (ERF; Myhre et al. 2013), ΔT is the global-mean surface air temperature anomaly, and λ is the net radiative feedback parameter (negative for a stable climate). By definition, ECS $= -F_{2x}/\lambda_{eq}$, where F_{2x} is the ERF from CO_2 doubling, and λ_{eq} is the radiative feedback when a new equilibrium is reached ($\Delta N = 0$). Ideally, ECS can be estimated from equilibrium states within global climate models (GCM) forced by an abrupt CO_2 doubling (abrupt-2xCO2) or CO_2 quadrupling (abrupt-4xCO2), after sufficiently long integration (Rugenstein et al., 2020). In practice, ECS is often extrapolated from a linear regression of ΔN against ΔT for the first 150yrs of abrupt-4xCO2 simulations (Gregory et al., 2004). This extrapolation generally underestimates the true ECS due to changes in the net radiative feedback as climate equilibrates (Dunne et al., 2020; Rugenstein et al., 2020), owing to time-evolving surface warming patterns (Andrews et al., 2015; Armour et al., 2013; Dong et al., 2020), and nonlinear mean-state dependence of radiative feedbacks (Bloch-Johnson et al., 2015, 2021; Caballero and Huber, 2013). Therefore, we refer the ECS values estimated from these non-equilibrium states to as an *effective* climate sensitivity (EffCS) (Andrews et al., 2015; Sherwood et al., 2020):

$$\text{EffCS} = -\frac{F_{2x}}{\lambda_{\text{eff}}}, \tag{3.2}$$

assuming the effective radiative feedback (λ_{eff}) at a transient state remains constant to

equilibrium. We use $\mathrm{EffCS_{4xCO2}}$ to refer to ECS estimates from abrupt-4xCO2 simulations (through regressions of annual-mean ΔN against ΔT for the first 150yrs; data from Zelinka et al. (2020)), and use $\mathrm{EffCS_{his}}$ to refer to ECS estimates from historical energy budget constraints (see more details in section 3.3).

TCR is commonly calculated as the global-mean surface air temperature change averaged over a 20-year period centered on year 70 of the 1pctCO2 simulations where CO_2 concentration is doubled (referred to as $\mathrm{TCR_{1pct}}$ here). The values of TCR can also be estimated from historical energy budget constraints (see more details in Section 4), in which case we refer to it as $\mathrm{TCR_{his}}$.

Estimates of $\mathrm{EffCS_{his}}$ and $\mathrm{TCR_{his}}$ from observed energy budget constraints have been found to be lower than values of ECS and TCR inferred from other lines of observational and proxy evidence (Forster et al., 2021; Sherwood et al., 2020). However, AOGCMs have also been found to produce values of $\mathrm{EffCS_{his}}$ and $\mathrm{TCR_{his}}$ that are lower than their corresponding values of $\mathrm{EffCS_{4xCO2}}$ and $\mathrm{TCR_{1pct}}$, at least within the few models tested (Winton et al. 2020 for GFDL-CM4; Andrews et al. 2019 for HadGEM3-GC3.1-LL; Dessler et al. 2018 for MPI-ESM1.1). The limited number of model studies reflects the fact that the time-varying historical ERF (ΔF in Eq.3.1) is not often diagnosed, precluding accurate calculation of radiative feedback and thus $\mathrm{EffCS_{his}}$ and $\mathrm{TCR_{his}}$. Some other studies have instead used abrupt-4xCO2 or 1pctCO2 simulations as a surrogate for historical warming (Armour, 2017; Dong et al., 2020; Lewis and Curry, 2018; Proistosescu and Huybers, 2017), or used a rough estimate of historical ERF taken from IPCC AR5 (Myhre et al., 2013) for CMIP5 AOGCMs (Gregory et al., 2020; Marvel et al., 2018). These approaches generally find that $\mathrm{EffCS_{4xCO2}}$ is larger than $\mathrm{EffCS_{his}}$, but it is unclear how accurate their estimates are given that they do not use model-specific estimates of historical ERF.

This work is thus motivated by two key questions: (1) how robust is the finding that values of $\mathrm{EffCS_{4xCO2}}$ and $\mathrm{TCR_{1pct}}$ are higher than values of $\mathrm{EffCS_{his}}$ and $\mathrm{TCR_{his}}$ estimated using historical energy budget constraints? (2) How do the estimates of $\mathrm{EffCS_{his}}$ and $\mathrm{TCR_{his}}$ from models compare to those from observations? The answers to these questions have major implications for how the historical record informs future climate projections. Here we employ simulations of the Radiative Forcing Model Intercomparison Project (RFMIP)

(Pincus et al., 2016), which provide the time series of historical ERF for 8 CMIP6 AOGCMs (section 2). With ERF in hand, we assess $\mathrm{EffCS_{his}}$ and $\mathrm{TCR_{his}}$ values within historical simulations, and compare to the corresponding values of $\mathrm{EffCS_{4xCO2}}$ and $\mathrm{TCR_{1pct}}$ within models and the estimates from observations.

3.2 Data

3.2.1 Historical Effective Radiative Forcing from RFMIP Simulations

The ERF includes rapid adjustments from the atmosphere in response to changes in CO_2 or other forcing agents (Myhre et al., 2013). It can be quantified from the TOA radiation changes within atmosphere-only GCM (AGCM) simulations wherein forcing agents are changed while SST and sea-ice concentration (SIC) fields are fixed at pre-industrial values (Forster et al., 2016). Here we make use of the fixed-SST simulations of RFMIP that are currently available for 8 CMIP6 models (CanESM5, CNRM-CM6-1, GFDL-CM4, GISS-E2-1-G, HadGEM3-GC31-LL, IPSL-CM6A-LR, MIROC6, NorESM2-LM). The timeseries of historical ERF is calculated as the difference of net TOA radiative flux between a 30-year control run (piClim-control), where all forcing agents are fixed to pre-industrial levels, and a forcing run (piClim-histall), where time-varying atmospheric concentrations of all historical forcing agents are imposed. ERF from a single group of forcing agents (e.g., greenhouse gases, anthropogenic aerosols, natural forcings including volcanoes and solar variability) can also be estimated using single-forcing runs of RFMIP (piClim-histghg, piClim-histaer, piClim-histnat, respectively). We also estimate ERF of CO_2 doubling, F_{2x}, from RFMIP piClim-4xCO2 simulations, where CO_2 is abruptly quadrupled and held constant for 30yrs while SST and SIC fields are fixed. F_{2x} is computed from the TOA radiation changes of the 30yr-average (scaled by 1/2 to estimate the forcing for CO_2 doubling from CO_2 quadrupling simulations). For all RFMIP simulations, the ensemble mean is used when more than one member of the simulation exist.

Note that the TOA radiation flux changes derived from the fixed-SST simulations includes the effect of temperature changes over land and sea ice, which should be considered as part of the radiative response rather than ERF. We remove this portion of radiative effects

by subtracting off the global-mean surface air temperature change scaled by each model's radiative feedback parameter from its abrupt-4xCO2 simulation – the method proposed in Hansen et al. (2005). Recent studies find advantages in several new correction methods, such as fixing both SST and land-surface temperatures in AGCM (Andrews et al., 2021), or using surface temperature radiative kernels (Smith et al., 2020). We choose to apply the Hansen et al. (2005) method here because it is a widely used method and readily improves ERF estimates using the available output of the RFMIP simulations. All the historical ERFs are calculated as global and annual means, spanning the period 1850 – 2014 (the same interval of fully-coupled historical simulations).

3.2.2 Historical simulations of AOGCMs and AGCMs

Within historical simulations of AOGCMs, we compute global mean N and T from the mean of all available ensemble members, in attempt to reduce noises from internal variability. Except for GFDL-CM4 (1 member), NorESM2-LM (3 members), and HadGEM3-GC31-LL (4 members), the rest of models have more than 30 historical ensemble members available. The annual mean changes of N and T with respect to the preindustrial control simulations (piControl) are computed by subtracting the linear regression of piControl values over time segment corresponding to the abrupt4xCO2 simulation, following Armour (2017); Forster et al. (2013). Note that ΔN, ΔF, and ΔT in the energy budget framework (Eq. 3.1) can also be defined as differences between two specific historical states. We will elaborate these historical periods over which we compute the historical energy balance in the following two sections. In order to examine the contributions of individual forcing agents to historical climate change, we also employ single-forcing historical simulations (hist-GHG, hist-aer, hist-nat), described by the Detection and Attribution Model Intercomparison Project (DAMIP) (Gillett et al., 2016), where only one type of forcing agent is changed while all other forcing agents are fixed at preindustrial levels.

Results from the coupled AOGCMs are compared to two sets of AGCM simulations. One is called "amip" simulation, a CMIP6 DECK experiment (Eyring et al., 2016) where AGCMs are forced by time-evolving observed SST and SIC fields and by time-varying

historical forcing agents. While amip simulations are available for all of the 8 CMIP6 models assessed here, they are performed only over 1979–2015. The other one is called "amip-piForcing" simulation, described by the Cloud Feedback Model Intercomparison Project (CFMIP) (Webb et al., 2017), where AGCMs are forced by the same observed SST and SIC fields over 1870–2014, except all radiative forcing agents are fixed at pre-industrial levels. In section 3. we show EffCS estimates from both amip and amip-piForcing runs, which are generally consistent with each other. A caveat is that only 6 out of 8 models used have amip-piForcing experiments available (CanESM5, CNRM-CM6-1, GFDL-CM4, HadGEM3-GC31-LL, IPSL-CM6A-LR, MIROC6). For both sets of AGCM simulations we only use the first realization of each model, given that most of the variability in TOA radiative fluxes comes about through variations in SSTs which are the same in these AGCM simulations.

3.3 Historical Energy Budget Constraints on Radiative Feedbacks and EffCS

In the energy budget framework, $\mathrm{EffCS}_{\mathrm{his}}$ can be written as:

$$\mathrm{EffCS}_{\mathrm{his}} = -\frac{F_{2\mathrm{x}}}{\lambda_{\mathrm{his}}}, \tag{3.3}$$

where the historical effective radiative feedback parameter (λ_{his}) is given by:

$$\lambda_{\mathrm{his}} = \frac{\Delta N - \Delta F}{\Delta T}. \tag{3.4}$$

For the historical and amip simulations, we calculate λ_{his} and $\mathrm{EffCS}_{\mathrm{his}}$ use ΔN and ΔT taken from those simulations combined with ΔF from each model's RFMIP simulation. For the amip-piForcing simulations, which have constant forcing, we calculate λ_{his} and $\mathrm{EffCS}_{\mathrm{his}}$ only using ΔN and ΔT taken from those simulations (i.e., $\Delta F = 0$).

We first show historical variations in λ_{his}, calculated by a linear regression form of Eq. 3.4 in a sliding 30-year window. We find remarkable differences in decadal-scale radiative feedbacks between historical simulations (black line in Fig. 3.1a) and amip-piForcing simulations (blue line in Fig. 3.1a). While natural variability may have played a dominant role in the first half of the 20th century, where net ERF was relatively small (Fig. 3.2), the discrepancy between AOGCMs and AGCMs persists throughout the full historical period

towards early 21st century. Notably, λ_{his} in the amip-piForcing simulations of AGCMs (denoted as "amipPF" in Fig. 3.1) trends toward more-negative values since 1970s to present, consistent with earlier studies using CMIP5 models (Andrews et al., 2018; Dong et al., 2019; Gregory et al., 2020; Silvers et al., 2018), whereas in the historical simulations of AOGCMs, λ_{his} trends slightly toward more-positive values, and by the end of the century becomes comparable to the values of λ_{4xCO2} from abrupt-4xCO2 runs. During the second half of the century, λ_{his} values from AOGCMs track those in hist-GHG simulations (red line), suggesting the simulated feedbacks are primarily driven by GHG forcing, which has dominated global net ERF over this period (Fig. 3.2).

We next assess $\text{EffCS}_{\text{his}}$ from energy budget constraints within the historical simulations of the AOGCMs and the AGCMs. To compute the energy budget in Eqs. 3.3 and 3.4, the time interval over which anomalies (Δ) are calculated needs to be carefully chosen to avoid short-term variability and effects of volcanic eruptions (Lewis and Curry 2014; Forster 2016). Previous studies have often used two methods: (1) taking finite differences between a base period and a final period (Lewis and Curry, 2015, 2018; Sherwood et al., 2020; Winton et al., 2020); or (2) using regression over the full period of interest (Andrews et al., 2019; Gregory et al., 2020). Since we are comparing EffCS between AOGCMs and AGCMs (including amip simulations which are only available from 1979 onwards), we choose to use the regression method here. That is, the λ_{his} used to compute $\text{EffCS}_{\text{his}}$ (Eq. 3.3) is calculated via ordinary least squares regression of Eq. 3.4, over two periods of our interest: the full historical period 1870–2014 (Fig. 3.1b), and the recent decades of the Satellite Era 1979–2014 (Fig. 3.1c).

3.3.1 $EffCS_{his}$ from Long-term Historical Energy Budget (1870–2014)

The values of $\text{EffCS}_{\text{his}}$ inferred from long-term energy budget in historical simulations are generally lower than $\text{EffCS}_{\text{4xCO2}}$ from abrupt-4xCO2 simulations (Fig. 3.1b). As noted above, the difference between $\text{EffCS}_{\text{his}}$ and $\text{EffCS}_{\text{4xCO2}}$ has been documented in a few models. For GFDL-CM4, Winton et al. (2020) found an $\text{EffCS}_{\text{his}}$ of 1.8K and an $\text{EffCS}_{\text{4xCO2}}$ of 4K ($\text{EffCS}_{\text{4xCO2}}$ = 5K if using yrs 51-300 of the model's extended abrupt-4xCO2 simulation). For HadGEM3-GC3.1-LL, Andrews et al. (2019) found an effective F_{2x} of 3.49 Wm^{-2}

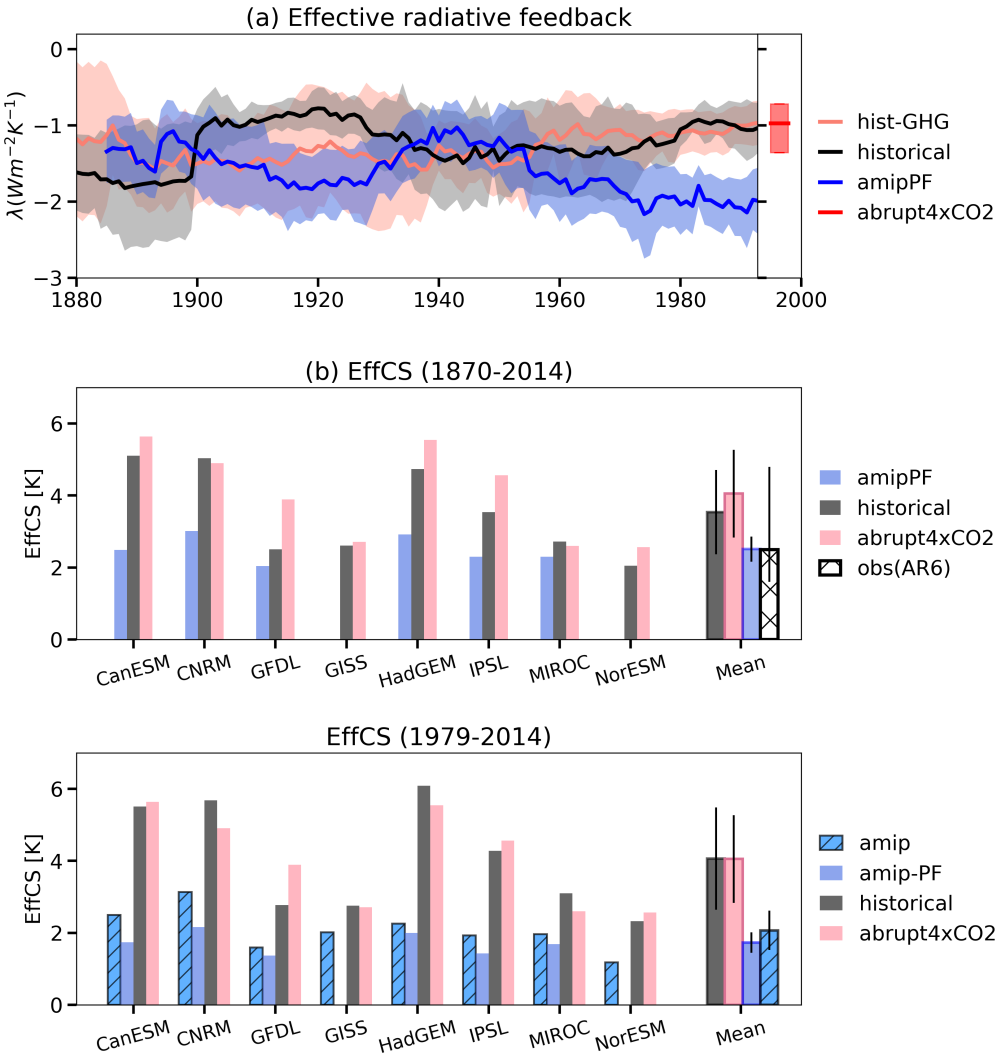

Figure 3.1: (a) Time series of the estimated λ_{his}. Thick lines denote multi-model means, shadings denote one standard deviation across models. The box plot on the right denotes the interquartile range (box) and the mean value (red line) of λ_{4xCO2} across 8 models. (b, c) EffCS estimated from the energy budget of (b) full historical record (1870–2014) and (c) recent decades (1979–2014). The outlined colored bars on the right in (b, c) denote the multi-model mean values of EffCS from corresponding simulations, with error bars indicating one standard deviation across models. The white hatched bar in (b) denotes the median $\text{EffCS}_{\text{his}}$ value of 2.5K based on observed energy budget changes reported in IPCC AR6 (Forster et al., 2021), with the error bars denoting 5-95% range of 1.6 – 4.8 K. Models listed (from the left to right) are: CanESM5, CNRM-CM6-1, GFDL-CM4, GISS-E2-1-G, HadGEM3-GC31-LL, IPSL-CM6A-LR, MIROC6, NorESM2-LM.

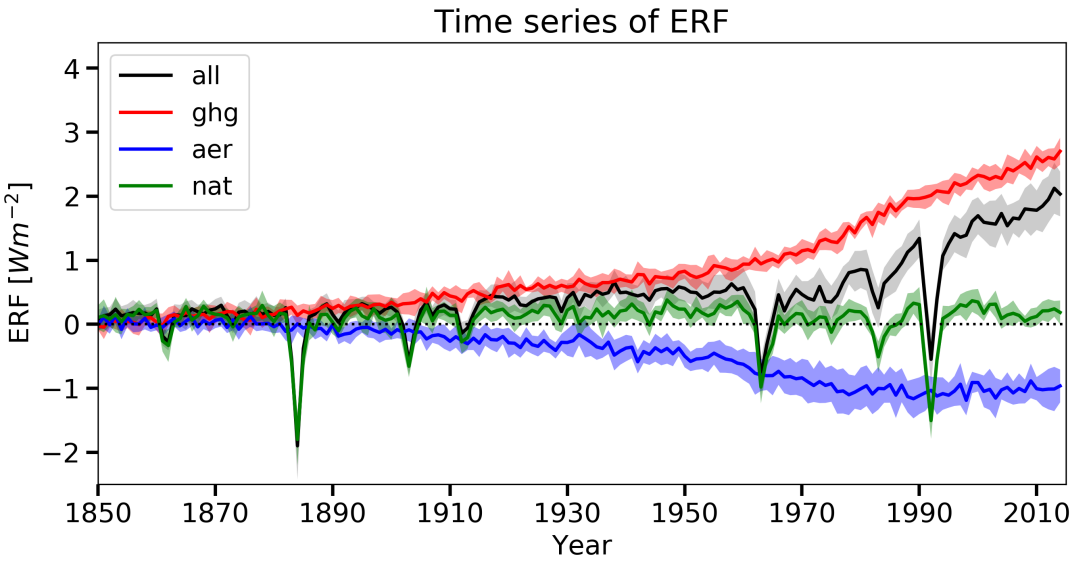

Figure 3.2: Time series of historical effective radiative forcing estimated from RFMIP simulations. Thick lines denote multi-model means, shadings denote one standard deviation across models.

and a historical feedback of 0.86 $\mathrm{Wm^{-2}K^{-1}}$ (average of 4 ensembles), implying an $\mathrm{EffCS_{his}}$ of 4.1K, in contrast to the model's $\mathrm{EffCS_{4xCO2}}$ of 5.5K. Here we show that, within 6 out of 8 CMIP6 AOGCMs assessed, historical energy budget constraints underestimate $\mathrm{EffCS_{4xCO2}}$ from CO_2 quadrupling. Values of $\mathrm{EffCS_{his}}$ range from 4.6% above to 35.6% below values of $\mathrm{EffCS_{4xCO2}}$, with an average of 12.6% below across these 8 models (Table 3.1). Averaging over all these 8 AOGCMs that are currently available, $\mathrm{EffCS_{his}}$ is 3.54 K ($\pm$1.17K; one standard deviation across models, unless noted elsewhere) and $\mathrm{EffCS_{4xCO2}}$ is 4.05K ($\pm$1.46 K), corresponding to an averaged λ_{his} of -1.16 $\mathrm{Wm^{-2}K^{-1}}$ ($\pm$0.37 $\mathrm{Wm^{-2}K^{-1}}$) and λ_{4xCO2} (from the regression of 150yrs abrupt-4xCO2 simulations) of -0.97 $\mathrm{Wm^{-2}K^{-1}}$ ($\pm$0.34 $\mathrm{Wm^{-2}K^{-1}}$), respectively. Lower values of $\mathrm{EffCS_{his}}$ are found in AGCM amip-piForcing experiments over the same historical period, with a mean $\mathrm{EffCS_{his}}$ value of 2.51K ($\pm$0.35K) across 6 available models, which is lower than the mean $\mathrm{EffCS_{4xCO2}}$ value of 4.52 K ($\pm$1.04 K) across the same 6 models by 44%. Using the Winton et al. (2020) method, i.e., taking ΔN, ΔT and ΔF as differences between 1869 – 1882 and 1995 – 2014, yields nearly the same result: the mean

value of $\text{EffCS}_{\text{his}}$ is 3.42 K ($\pm$1.24 K) from historical simulations across all 8 AOGCMs and 2.54 K ($\pm$0.4 K) from amip-piForcing simulations across 6 available AGCMs.

The EffCS and radiative feedback differences between historical energy budget constraints and CO_2 quadrupling in models arise primarily from differences between historical and near-equilibrium warming patterns (Fig. 3.3). Under CO_2 quadrupling, AOGCMs generally project an equilibrium warming pattern featuring polar amplification and weakened tropical Pacific west-east SST gradient (Fig. 3.2c) (Andrews et al., 2015; Andrews and Webb, 2018; Ceppi and Gregory, 2017; Dong et al., 2020); whereas the SST trend pattern in historical simulations are more spatially uniform (Fig. 3.3a). It has been argued that the projected enhancement of warming in the tropical eastern Pacific relative to the tropical western Pacific in models tends to weaken the lower tropospheric stability, thereby weakening the negative low cloud feedback and negative lapse-rate feedback, producing a higher EffCS (Andrews and Webb, 2018; Ceppi and Gregory, 2017; Dong et al., 2019; Zhou et al., 2016). In contrast, the relatively uniform tropical warming patterns simulated in historical simulations would maintain negative cloud feedback and therefore lower EffCS. The fact that $\text{EffCS}_{\text{his}}$ estimates from amip-piForcing simulations are even lower can be traced to their SST patterns prescribed from observations, featuring slightly enhanced warming in the Indo-Pacific Ocean and delayed warming in both the eastern Pacific Ocean and part of the Southern Ocean (Dong et al., 2020, 2019; Silvers et al., 2018; Zhou et al., 2016).

The historical pattern effect that leads to lower values of $\text{EffCS}_{\text{his}}$ may partially result from various non-CO_2 forcing agents that have operated in the historical period (Forster, 2016; Marvel et al., 2016). Gregory et al. (2020) suggest that volcanic forcing may bias the estimate of EffCS from CO_2 quadrupling by causing different surface warming patterns in CMIP5 models. Winton et al. (2020) find that a large portion of the $\text{EffCS}_{\text{his}}$ underestimate in GFDL-CM4 is attributable to its large efficacy of aerosol forcing. To test this possibility within other CMIP6 models, we make use of the DAMIP non-GHG forcing simulations, namely, hist-aer and hist-nat (Fig. 3.4). Within all but one model, natural forcing (volcanoes and solar variability) alone produces even lower values of $\text{EffCS}_{\text{his}}$ than those from historical simulations (i.e., a larger historical pattern effect). In comparison, when forced by anthropogenic aerosol forcing alone, four models show a larger historical pattern effect

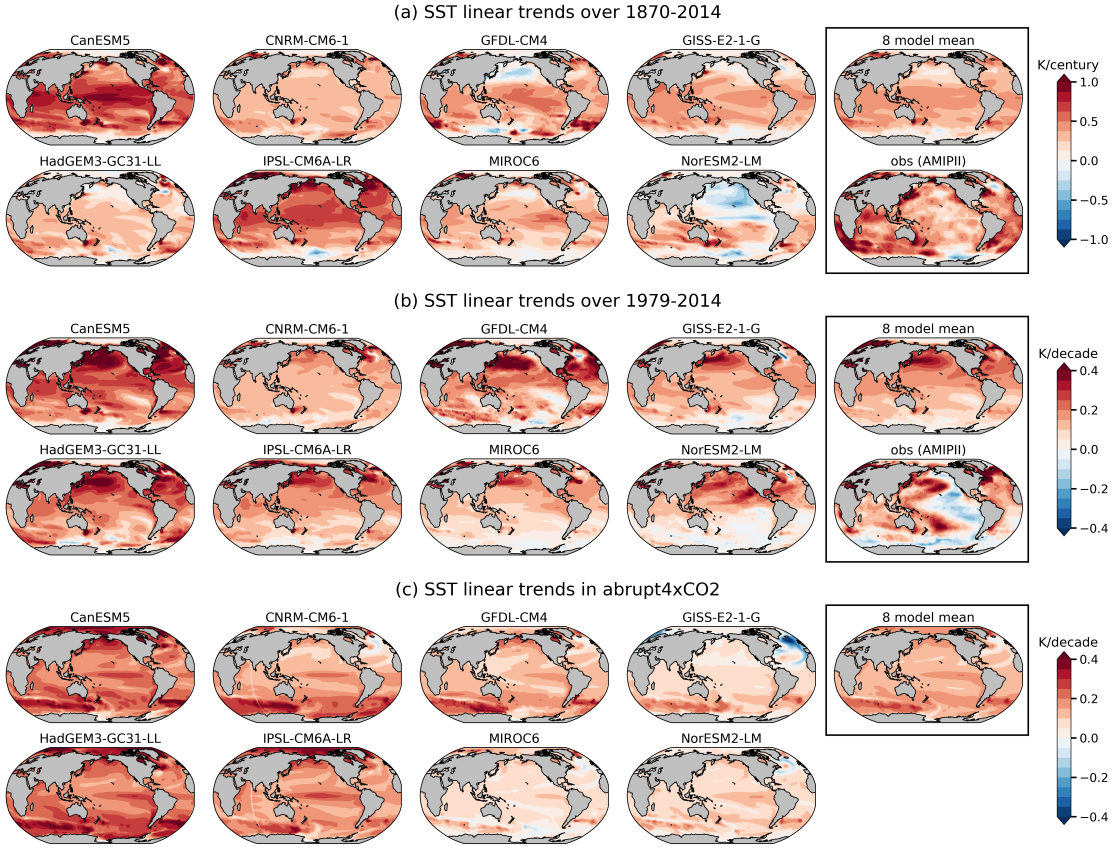

Figure 3.3: Historical and equilibrium SST trend patterns. SST linear trends over (a) 1870–2014, (b)1979–2014, and (c) 150 years of abrupt-4xCO2 simulations, calculated via OLS regressions of annual-mean SST against time. The observed SST trend patterns in (a, b) are calculated using AMIPII dataset (Hurrell et al., 2008).

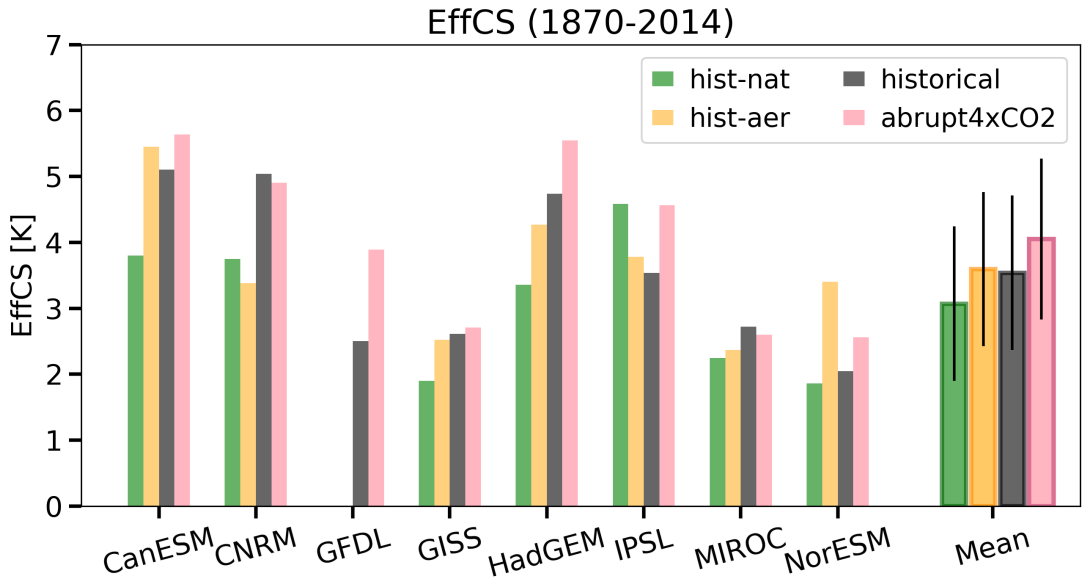

Figure 3.4: Similar to Fig. 3.1b, except $\mathrm{EffCS_{his}}$ estimates are from historical energy budget constraints within historical non-GHG simulations. Yellow bars denote the values of $\mathrm{EffCS_{his}}$ from simulations forced solely with anthropogenic aerosol forcing (hist-aer), and green bars denote the values of $\mathrm{EffCS_{his}}$ from simulations forced solely with natural forcing (hist-nat). Note that GFDL-CM4 currently does not have single-forcing historical simulations available.

while three models show a reduced pattern effect. These results suggest that non-GHG forcing may largely account for the historical pattern effect, though the impact of aerosol forcing is less robust across models.

3.3.2 $EffCS_{his}$ from Recent Energy Budget (1979–2014)

Having quantified the long-term historical energy budget constraint on EffCS, we next focus on the most recent decades 1979–2014 (Fig. 3.1c), where observations of global SSTs have been improved by satellite products and better *in situ* sampling. This is also the period where GHG forcing has increased dramatically while aerosol forcing trends are relatively small (Fig. 3.2). With stronger ERF having operated over this period, nearly all coupled AOGCMs produce higher values of $\mathrm{EffCS_{his}}$, with a multi-model mean $\mathrm{EffCS_{his}}$ of 4.06K (corresponding to a mean radiative feedback of -1.02 $\mathrm{Wm^{-2}K^{-1}}$), comparable to the mean

$\text{EffCS}_{\text{4xCO2}}$ of 4.05K.

Does this imply that the historical pattern effect is weak in recent decades? In fact, the $\text{EffCS}_{\text{his}}$ values over this period from all 8 AOGCMs are substantially higher than the values from their AGCM counterparts driven by observed warming patterns within amip and amip-piForcing simulations (Fig. 3.1c). Averaging over all these AGCMs, the mean $\text{EffCS}_{\text{his}}$ and the corresponding λ_{his} from amip simulations is 2.07 K ($\pm$0.57 K) and -1.92 $\text{Wm}^{-2}\text{K}^{-1}$ ($\pm$0.58 $\text{Wm}^{-2}\text{K}^{-1}$), respectively. Note that $\text{EffCS}_{\text{his}}$ estimates from amip runs are slightly higher than those from amip-piForcing runs, potentially due to minor biases in the estimates of ERF from RFMIP fixed-SST simulations (Andrews et al., 2021), but the difference between these two AGCM simulations is much smaller than the difference between AOGCM historical simulations and AGCM prescribed-SST simulations.

The $\text{EffCS}_{\text{his}}$ difference between AOGCMs and their counterpart AGCMs can be traced to the difference between modeled and observed SST patterns over recent decades. The ensemble-mean SST trend pattern in historical simulations of AOGCMs fails to capture many key features in observations (Fig. 3.3b), including the pronounced cooling trends over the eastern Pacific and Southern Ocean. The enhanced tropical Pacific zonal SST gradient has been linked to the observed increase in low clouds over the stratocumulus deck, which contributes to a more-negative radiative feedback and lower EffCS (Ceppi and Gregory, 2017; Dong et al., 2019; Fueglistaler, 2019; Zhou et al., 2016). The Southern Ocean SSTs have also been found to have large impacts on low-cloud feedbacks over the Southern Ocean and therefore EffCS (Dong et al., 2020; Gjermundsen et al., 2021). Moreover, potential teleconnections from the Southern Ocean to the tropical Pacific may also contribute to the observed changes in the tropical cloud feedback and lower EffCS over this period (Hwang et al., 2017; Kang et al., 2020).

A few studies have argued that the observed tropical Pacific SST pattern may be driven by aerosol forcing (Takahashi and Watanabe, 2016) or volcanic forcings (Gregory et al., 2020). Using the DAMIP simulations, we found that the SST trend patterns driven by anthropogenic aerosol forcing and natural forcing are indeed more spatially heterogeneous, with some models showing weak cooling in the tropical eastern Pacific (Fig. 3.5). However, the cooling trends produced in these non-GHG simulations are much weaker than that ob-

served, and are generally overwhelmed by the warming trends in AOGCMs forced by GHG forcing only(Fig. 3.5a). It is also possible that the observed warming pattern in part results from natural variability. For example, Watanabe et al. (2021) found that the observed equatorial Pacific west-east SST gradient over a longer period (1951-2010) lies within the range of large ensembles of model simulations. However, such regional analyses may be insufficient to explain the observed SST trend pattern beyond the equatorial Pacific, and their results may be sensitive to the time interval selected. We have examined $\mathrm{EffCS_{his}}$ and the equatorial Pacific zonal SST gradient for all individual members of historical simulations. We define the zonal SST gradient following Watanabe et al. (2021): the difference between the eastern Pacific (180°–80°W, 5°S–5°N) and the western Pacific (110°E–180°, 5°S–5°N). But we calculate SST linear trends over 1979–2014 instead of 1951–2010. Over these recent decades, nearly all of the 201 ensemble members fail to capture the low $\mathrm{EffCS_{his}}$ values from the corresponding amip simulations and the observed zonal SST gradient (Fig. 3.6), suggesting a significant discrepancy in the pattern effect between AOGCMs and observations.

Our results on the historical energy budget constraints suggest that $\mathrm{EffCS_{his}}$ estimates from historical simulations generally underestimate $\mathrm{EffCS_{4xCO2}}$ from CO_2 quadrupling due to the pattern effect. However, the historical pattern effect is relatively small over recent decades in AOGCMs, owing to the fact that their historical warming patterns over recent decades are not substantially different from their equilibrium warming patterns. The potential causes of the recent observed SST trend pattern are the focus of Chapter 4.

3.4 Historical Energy Budget Constraints on TCR

In the energy budget framework, TCR can be inferred from sufficiently long-term historical record where ΔT increases approximately proportional to ΔF:

$$\mathrm{TCR_{his}} = \Delta T \frac{F_{2x}}{\Delta F}. \tag{3.5}$$

Under the global energy framework (Eq. 3.1), $\mathrm{TCR_{his}}$ is governed by both historical radiative feedback (λ_{his}) and ocean heat uptake (OHU) efficiency (κ_{his}), with the relationship between these approximated as (Gregory et al., 2015; Gregory and Forster, 2008; Gregory

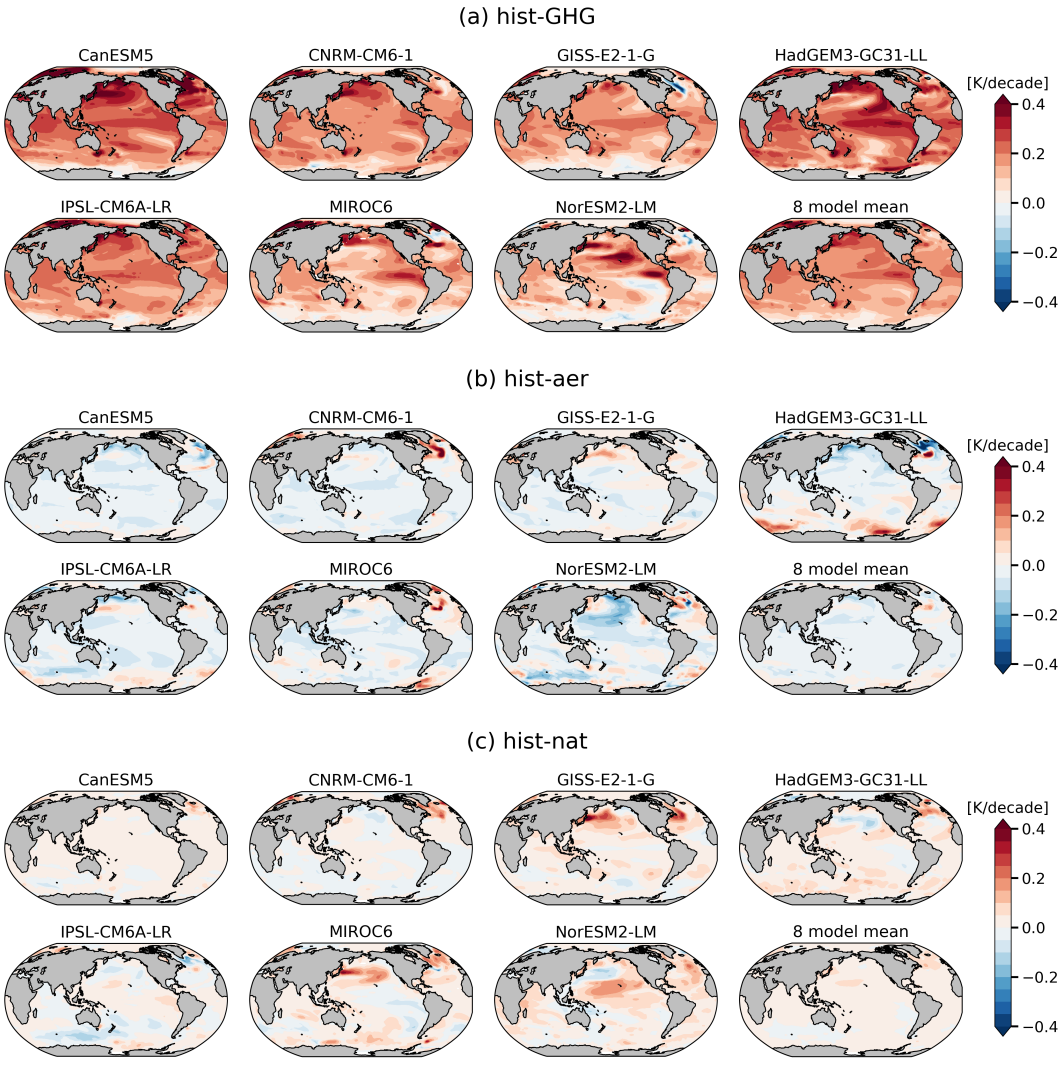

Figure 3.5: Similar to Figure 3.3(b), patterns of SST linear trends over 1979–2014 from (a)hist-GHG, (b)hist-aer, (c)hist-nat simulations.

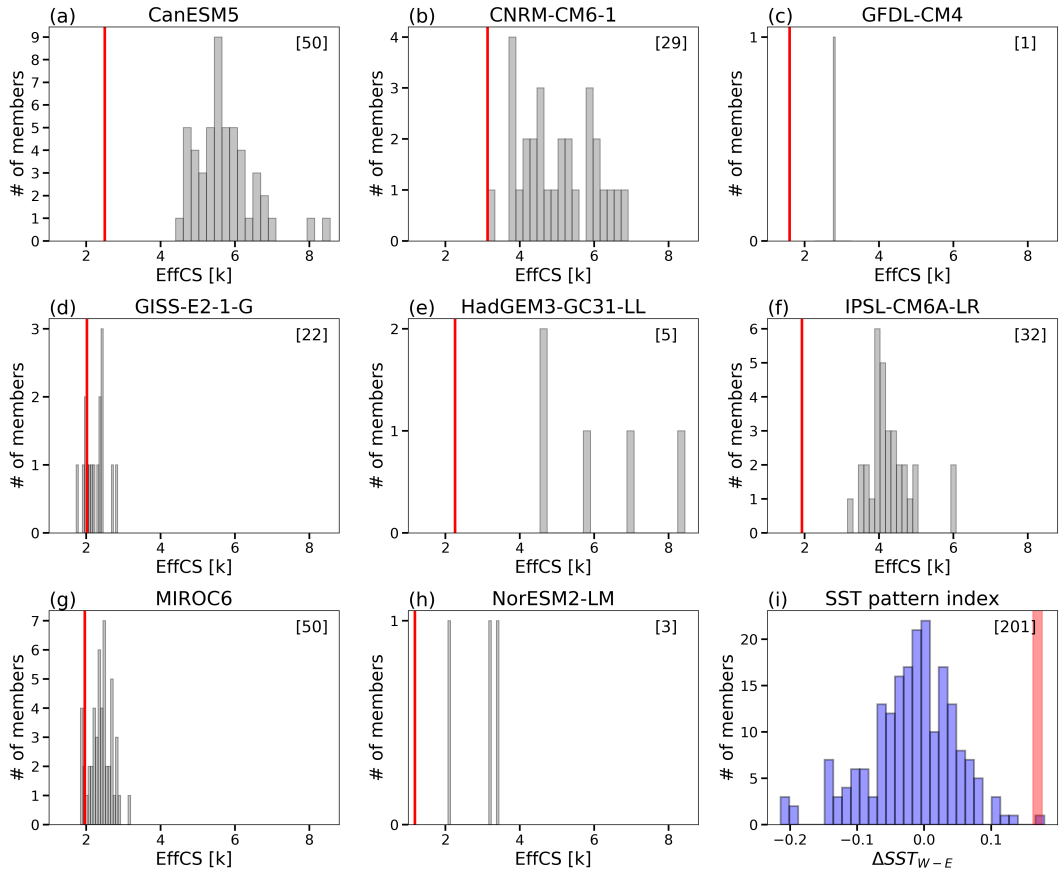

Figure 3.6: (a - h) $\mathrm{EffCS_{his}}$ from 1979–2014 of all available members of historical simulations (black bar) and amip simulations (red line) for each of the eight models. (i) The tropical Pacific zonal SST gradient ($\Delta SST_{\mathrm{W\text{-}E}}$) over 1979–2014 defined inWatanabe et al. (2021) from all models historical ensemble members (blue bars) and observations (red shading). The observations include four datasets: HadISST1 (Rayner et al., 2003), AMIPII (Hurrell et al., 2008), COBE-SST2 (Hirahara et al., 2014), ERSSTv5 (Huang et al., 2017a). The red shading denotes the mean $\Delta SST_{\mathrm{W\text{-}E}}$ ± 1 standard deviation across four observational datasets. The number in the top right corner in each panel denotes the number of total model ensembles plotted.

and Mitchell, 1997; Raper et al., 2002):

$$\mathrm{TCR_{his}} = \frac{F_{2x}}{\kappa_{\mathrm{his}} - \lambda_{\mathrm{his}}}, \tag{3.6}$$

where κ_{his} is defined as:

$$\kappa_{\mathrm{his}} = \frac{\Delta N}{\Delta T}. \tag{3.7}$$

Here we calculate $\mathrm{TCR_{his}}$ from historical simulations using Eq. 3.5, where anomalies (Δ) are averaged over 1995 – 2014 relative to 1869 – 1882. This period is chosen to cover a sufficiently long time of historical record, and also to be largely consistent with several recent studies (Lewis and Curry, 2018; Winton et al., 2020). As noted above, Winton et al. (2020) found a $\mathrm{TCR_{his}}$ of 1.27K for GFDL-CM4, lower than the model's $\mathrm{TCR_{1pct}}$ of 2.05K. Here we find that 7 out 8 AOGCMs assessed here are consistent with GFDL-CM4 – the historical energy budget constraint underestimates TCR values from 1pctCO2 simulations (Fig. 3.7a). Values of $\mathrm{TCR_{his}}$ range from 9.7% above to 32.2% below values of $\mathrm{TCR_{1pct}}$, with an average of 13% below across all 8 models. The mean $\mathrm{TCR_{his}}$ value across 8 AOGCMs is 1.81K ($\pm$0.51K), lower than the mean $\mathrm{TCR_{1pct}}$ value of 2.08K ($\pm$0.43K).

As shown in Eq. 3.6, the difference between $\mathrm{TCR_{his}}$ and $\mathrm{TCR_{1pct}}$ could arise from changes in radiative feedbacks and/or changes in OHU efficiency over time (Gregory et al., 2015). To separate these two factors, we estimate λ and κ from historical and 1pctCO2 simulations, following Eq. 3.4 and Eq. 3.7, respectively. For historical estimates, ΔN, ΔT and ΔF are taken as finite differences between 1995 - 2014 and 1869 - 1882. For 1pctCO2 estimates, ΔN and ΔT are from the 20-year period centered on year 70 of the simulation when CO_2 is doubled; ΔF at the time of CO_2 doubling is approximated by F_{2x}, with a caveat that the true F_{2x} in 1pctCO2 simulations was found slightly non-logarithmic (Gregory et al., 2020, 2015).

In all models, κ_{his} is larger than κ_{1pct}, which could contribute to the lower values of $\mathrm{TCR_{his}}$ relative to $\mathrm{TCR_{1pct}}$ (Fig. 3.7b). The difference between κ_{his} and κ_{his} could arise, for instance, from changes in Atlantic meridional overturning circulation or Southern Ocean meridional overturning circulation, driven by historical non-CO_2 forcings (e.g., aerosol forcing or ozone-depleting substances). On the other hand, the difference between λ_{his} and λ_{1pct} varies by models (Fig. 3.7c). Two models show λ_{his} more negative than λ_{1pct}, along

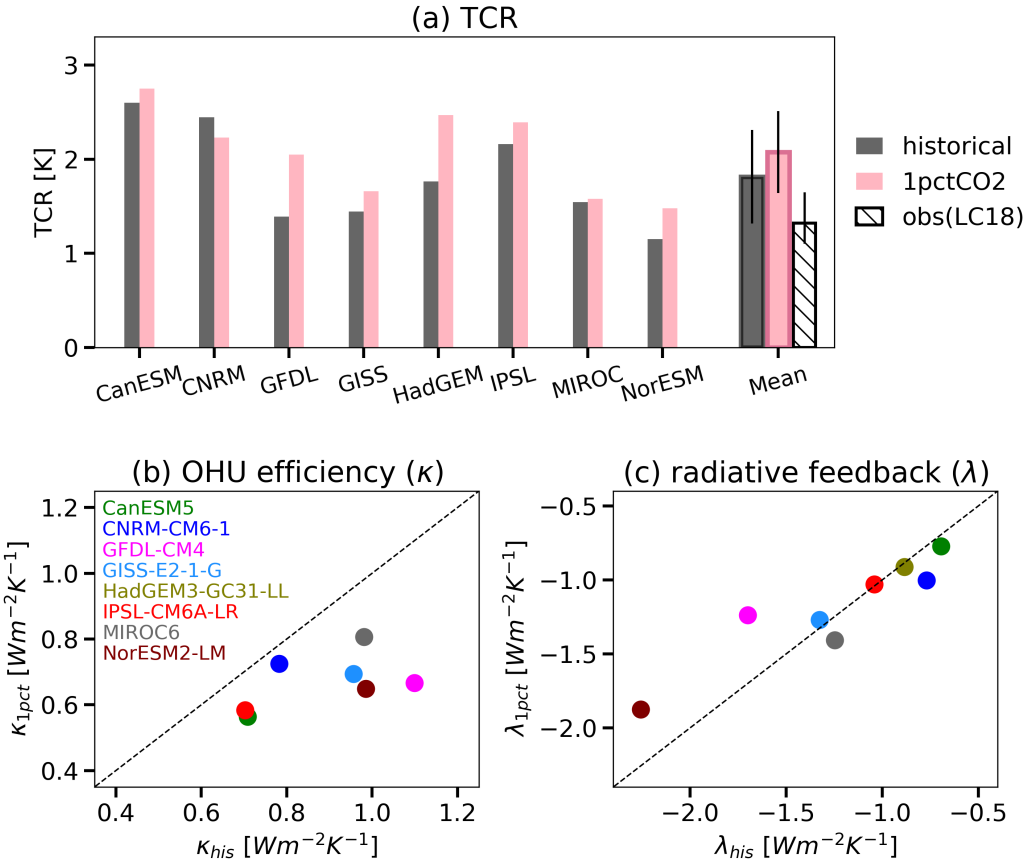

Figure 3.7: (a) TCR estimates from historical energy budget constraints and 1pctCO2 simulations. Black bars denote $\mathrm{TCR_{his}}$ values from fully-coupled historical simulations. Red bars denote $\mathrm{TCR_{1pct}}$ values from 1pctCO2 simulations. The white hatched bar denotes the best estimate of $\mathrm{TCR_{his}}$ of 1.32K based on observed energy budget changes reported by Lewis and Curry (2018), with a 17-83% range of 1.1-1.65K. (b) Ocean heat uptake efficiency and (c) radiative feedback from historical and 1pctCO2 simulations of all eight AOGCMs.

with their large κ_{his}, suggesting that the lower values of $\mathrm{TCR}_{\mathrm{his}}$ in these models are owing to changes in both radiative feedbacks and OHU efficiency. The rest of the models show λ_{his} either very close to or slightly less negative than λ_{1pct}, suggesting a dominant role of changes in κ.

In summary, we find an overall underestimate of TCR of about 0.2K using historical energy budget constraints within AOGCMs compared to that estimated in 1pctCO2 simulations, owing to the combination of more-negative radiative feedback and/or larger OHU efficiency during the historical period. The differences in λ and κ between historical and 1pctCO2 are largely ameliorated when using hist-GHG simulations (Fig. 3.8), suggesting that the underestimate of $\mathrm{TCR}_{\mathrm{his}}$ is mostly driven by historical non-GHG forcings. These results suggest that as time evolves and CO_2 forcing increases, the weakening of both radiative feedback and OHU efficiency could lead to higher values of TCR than those inferred from historical energy budget constraints.

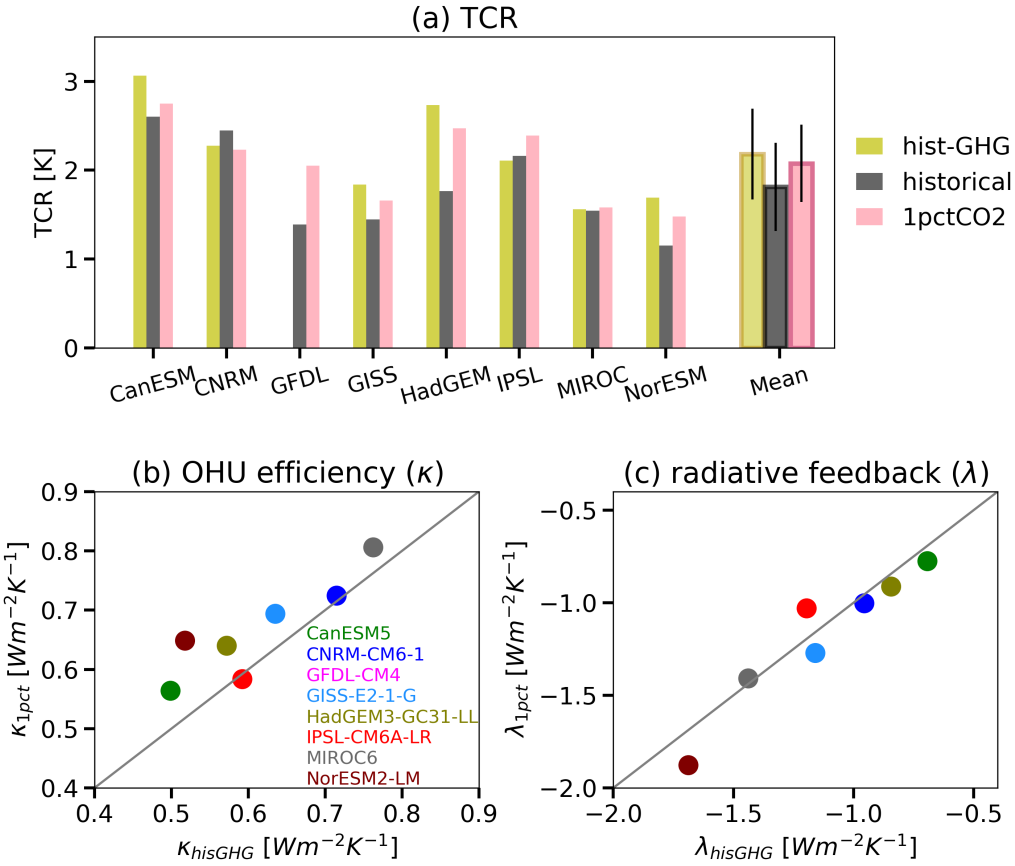

Figure 3.8: Same as Fig. 3.7, except in (a) yellow bars denote $\mathrm{TCR_{his}}$ values from hist-GHG simulations, and in (b, c) κ_{his} and λ_{his} values from hist-GHG simulations

3.5 Discussions and Conclusions

In the previous two sections, we have compared estimates of EffCS and TCR between different simulations of coupled and atmosphere-only GCMs. How do the model results compare to values of $\mathrm{EffCS_{his}}$ and $\mathrm{TCR_{his}}$ from observations, and what implications do the results have for our interpretation of the observed energy budget constraints?

In Figs. 1 and 3 we show that the reported values of $\mathrm{EffCS_{his}}$ and $\mathrm{TCR_{his}}$ from observations are much lower than the values of $\mathrm{EffCS_{4xCO2}}$ and $\mathrm{TCR_{1pct}}$ from CMIP6 models. For an observation-based estimate of $\mathrm{EffCS_{his}}$, we use values reported in IPCC AR6 (Forster et al., 2021): a median value of 2.5K and 5–95% range of 1.6–4.8K based on observed energy budget changes from 1850 - 1900 to 2006 – 2019 (Fig. 3.1b). For TCR, we use values reported by Lewis and Curry (2018): a median value of 1.32K and a 17—83% range of 1.1–1.65 K based on observed energy budget changes over 1869 – 1882 to 1995 – 2016 (Fig. 3.7). Values of $\mathrm{EffCS_{his}}$ from AGCM simulations forced by observed SST patterns are well in line with observation-based values of $\mathrm{EffCS_{his}}$, despite the fact that the values of $\mathrm{EffCS_{his}}$ and $\mathrm{EffCS_{4xCO2}}$ from their counterpart AOGCMs are both higher. The difference between estimates of $\mathrm{EffCS_{4xCO2}}$ from abrupt-4xCO2 simulations and estimates of $\mathrm{EffCS_{his}}$ from AGCM simulations with observed surface warming is thus owing to changes in SST patterns with time. It implies that if nature evolves towards equilibrium in the way that AOGCMs project, we should expect higher values of EffCS and TCR (i.e., evolving toward $\mathrm{EffCS_{4xCO2}}$ and $\mathrm{TCR_{1pct}}$) in the future than those inferred from observed energy budget constraints.

Our findings are broadly consistent with earlier studies focusing on two individual CMIP6 models (Andrews et al., 2019; Winton et al., 2020): historical energy budget constraints generally (within 6 out of 8 AOGCMs) underestimate the values of EffCS from CO_2 quadrupling and TCR from CO_2 ramping. The underestimate of $\mathrm{EffCS_{his}}$ is owing to differences in radiative feedbacks induced by the pattern effect; the underestimate of $\mathrm{TCR_{his}}$ is owing to a combination of differences in both radiative feedbacks and ocean heat uptake efficiency. Using observations, historical energy budget constraints provide even lower values of $\mathrm{EffCS_{his}}$ and $\mathrm{TCR_{his}}$, which are in line with the values from AGCMs forced by observed surface

warming. Accounting the pattern effect and assuming the observed SST pattern will evolve towards the projected equilibrium warming pattern, the observed historical energy budget may provide a biased-low constraint on EffCS and TCR.

That said, the projections by GCMs are confounded by not only uncertainties associated with atmospheric physics, e.g., cloud feedbacks (Sherwood et al., 2020; Webb et al., 2013; Zelinka et al., 2020), but also an open question: how reliable are model projections of future SST patterns? Coupled AOGCMs generally fail to reproduce the observed historical SST pattern, which led to an inconsistency between EffCS estimates from coupled historical runs and those from amip runs and observations. If the observed SST trend pattern is caused by natural variability, which will reverse sign in the coming decades according to AOGCM projections (Watanabe et al., 2021), then the higher values of EffCS and TCR found within AOGCMs may be more informative about near-future climate change under continued CO_2 forcing. If the recently observed SST trend pattern is a result of model biases in the response to GHG forcing (Coats and Karnauskas, 2017; Seager et al., 2019), the lower values of $\mathrm{EffCS_{his}}$ and $\mathrm{TCR_{his}}$ from observations may persist over the coming decades, in which case 21st century warming may be lower than that projected even by GCMs with realistic ECS values. This work suggests that both understanding the causes of the recent observed surface warming pattern and making accurate projections of future warming patterns are important for constraining transient and near-equilibrium climate change.

Table 3.1: Estimates of radiative feedback parameter, EffCS and TCR. For λ_{his} and $\text{EffCS}_{\text{his}}$ estimates derived from model historical energy budget constraints, values in the parenthesis are calculated from linear regression over 1979–2014, values outside of the parenthesis are calculated from linear regression over 1870–2014. λ_{4xCO2} and $\text{EffCS}_{\text{4xCO2}}$ from abrupt-4xCO2 simulations are calculated from regressions of ΔN against ΔT over 150yrs of the simulations. TCR_{his} values from historical simulations are calculated by taking differences between 1995–2014 and 1869–1882. (Note that multi-model mean is calculated by averaging over all 8 models, except for amip-piForcing estimates, in which case multi-model mean is average of 6 available models)

	Feedback parameter [$\text{Wm}^{-2}\text{K}^{-1}$]				EffCS [K]				TCR [K]	
Models	amipPF	amip	historical	4xCO2	amipPF	amip	historical	4xCO2	historical	1pctCO2
CanESM5	-1.46(-2.10)	(-1.46)	-0.72(-0.66)	-0.65	2.49(1.74)	(2.50)	5.11(5.51)	5.64	2.60	2.75
CNRM-CM6-1	-1.26(-1.76)	(-1.21)	-0.75(-0.67)	-0.74	3.01(2.16)	(3.13)	5.04(5.68)	4.90	2.45	2.23
GFDL-CM4	-1.90(-2.84)	(-2.44)	-1.55(-1.40)	-0.82	2.04(1.37)	(1.6)	2.51(2.77)	3.89	1.39	2.05
GISS-E2-1-G	N/A	(-1.64)	-1.26(-1.20)	-1.45	N/A	(2.01)	2.61(2.76)	2.71	1.44	1.66
HadGEM3-GC31-LL	-1.33(-1.93)	(-1.72)	-0.82(-0.64)	-0.63	2.92(2.00)	(2.26)	4.74(6.08)	5.55	1.76	2.47
IPSL-CM6A-LR	-1.64(-2.64)	(-1.96)	-1.07(-0.89)	-0.75	2.30(1.42)	(1.93)	3.54(4.28)	4.56	2.16	2.39
MIROC6	-1.50(-2.04)	(-1.75)	-1.26(-1.11)	-1.40	2.30(1.69)	(1.96)	2.72(3.10)	2.60	1.55	1.58
NorESM2-LM	N/A	(-3.17)	-1.82(-1.60)	-1.34	N/A	(1.18)	2.05(2.32)	2.56	1.15	1.48
Multi-model mean	-1.52(-2.22)	(-1.92)	-1.16(-1.02)	-0.97	2.51(1.73)	(2.07)	3.54(4.06)	4.05	1.81	2.08

Chapter 4

TWO-WAY TELECONNECTIONS BETWEEN THE SOUTHERN OCEAN AND THE TROPICAL PACIFIC VIA A DYNAMIC FEEDBACK

Abstract

Despite substantial global-mean warming, decadal-scale surface cooling has occurred in both the tropical eastern Pacific and Southern Ocean over the past 40 years, influencing not only regional climates but also the estimates of climate sensitivity. Using a paleo-reconstruction dataset of the past 2000 years, we find that sea-surface temperatures (SSTs) over the tropical eastern Pacific and part of the Southern Ocean near the southeast Pacific closely co-vary with each other on decadal timescales. While the tropical forcing on the extratropics has been extensively studied in the literature, here we focus on the other direction of the teleconnection, and ask: is the observed tropical eastern Pacific cooling connected to the observed Southern Ocean cooling?

Earlier studies proposed a zonal-mean energetic constraint as the leading atmospheric pathway, linking the response of the tropical Pacific to changes in the Southern Ocean. Using a slab-ocean model, we find that the tropical Pacific SST response to an imposed Southern Ocean surface heat flux (qflux) forcing is sensitive to the longitudinal location of that forcing, suggesting an atmospheric pathway associated with regional dynamics. The transient responses show that an imposed Southern Ocean cooling first propagates into the tropics by mean-wind advection. Once the tropical Pacific SSTs are perturbed, this tropical SST forcing can drive remote changes to the sea-level pressure and surface winds in the extratropics that are conducive to further enhancing the tropical cooling. These results suggest a mutually-interactive teleconnection between the tropical Pacific and the Southern Ocean through atmospheric circulations, and highlight potential impacts on the tropics from the extratropical climate changes that have occurred over the instrumental record.

4.1 Introduction

Observed global sea-surface temperatures (SST) have exhibited a unique pattern of warming trends since the 1980s: despite global-mean warming induced by the greenhouse gas (GHG) forcing, a broad cooling trend has occured in the tropical eastern Pacific and Southern Ocean (Fig. 4.1). In the tropical Pacific, the enhanced west-east SST zonal gradient was also associated with a strengthening of the Walker circulation along with strengthened trade winds (England et al., 2014; Kociuba and Power, 2015; L'Heureux et al., 2013). Around Antarctic, the observed surface cooling of the Southern Ocean was accompanied by an expansion of sea ice (Fan et al., 2014; Polvani and Smith, 2013; Turner et al., 2013), surface freshening, as well as a positive trend in the Southern Annular Mode (SAM) with intensified and poleward shift of surface westerly winds (Marshall, 2003; Thompson and Solomon, 2002). This observed SST trend pattern has had critical impacts not only on local climates such as tropical precipitation (Held and Soden, 2006), but also on the global warming rate (Kosaka and Xie, 2013) and the estimates of equilibrium climate sensitivity (ECS) and cloud feedbacks (Andrews et al. 2018; Zhou et al. 2016; Dong et al. 2019; Gregory et al. 2020; and also Chapter 3).

Correctly simulating the observed surface cooling trends in the tropical eastern Pacific and the Southern Ocean remains challenging for global climate models (GCMs) (Coats and Karnauskas, 2017; Fyfe et al., 2013; Kociuba and Power, 2015; Luo et al., 2018; Rye et al., 2020). The fact that GCMs under historical forcings tend to produce warming trends or less-cooling trends over these regions call into question the fidelity of model projections under continued CO_2 forcing (Plesca et al., 2018), including the equilibrium warming pattern with enhanced warming in the tropical eastern Pacific and Southern Ocean (Andrews et al., 2015; Dong et al., 2020; Heede et al., 2020; Li et al., 2013). More importantly, this projected equilibrium warming pattern is thought to give rise to a less-negative radiative feedback, and therefore higher values of ECS estimates than those inferred from recent observations (e.g., Andrews et al. 2018; Marvel et al. 2018; also see Chapter 3).

Yet the causes of the model-observation discrepancy remain unclear. The observed tropical Pacific SST trend pattern over the last few decades could arise from the Pacific

decadal natural variability (England et al., 2014; Kosaka and Xie, 2013; Watanabe et al., 2021) or could be in part influenced by the Atlantic multi-decadal variability through inter-basin teleconnection (Kajtar et al., 2018; Kucharski et al., 2015; Li et al., 2016; McGregor et al., 2018, 2014; Meehl et al., 2021; Wang, 2006). The observed tropical Pacific SST trend pattern could also be triggered by external forcings, such as anthropogenic aerosol forcing (Heede and Fedorov, 2021; Smith et al., 2016; Takahashi and Watanabe, 2016) or CO_2 forcing (Seager et al., 2019), which could be misrepresented by models due to model biases (Coats and Karnauskas, 2018; Kohyama et al., 2017; Seager et al., 2019). Similarly, the surface cooling of the Southern Ocean could result from freshwater input from retreating Antarctic ice sheets that reduces the ocean stratification (Bintanja et al., 2013; Bronselaer et al., 2018; Purich et al., 2018; Rye et al., 2020), from intensified surface westerlies associated with the positive SAM (Holland and Kwok, 2012; Purich et al., 2016), or from internal variability (Cabré et al., 2017; Latif et al., 2013; Zhang et al., 2019). While the mean ocean circulation has been proposed to largely account for the delayed Southern Ocean warming in response to GHG forcing (Armour et al., 2016), to what extent the observed surface *cooling* in the Southern Ocean is caused by external forcing or internal variability remains unclear.

Although there is no consensus on what has caused the observed cooling in the tropical eastern Pacific and the Southern Ocean respectively, the two locations could be connected through teleconnections. The tropical forcing on the extratropics has long been appreciated in the literature though an "atmospheric bridge" via Rossby wave trains generated from changes in the tropical convection (Ding et al., 2012; Li et al., 2021; L'Heureux and Thompson, 2006; Meehl et al., 2016; Trenberth et al., 1998). The tropical response to extratropical forcing has also been shown in previous studies, with two leading mechanisms proposed to account for different pathways: an atmospheric pathway through zonal-mean energetic constraints and an oceanic pathway through mean ocean circulation. The former is developed from aquaplanet slab-ocean simulations, where tropical precipitation and Walker circulation are found to respond to extratropical thermal forcing via anomalous cross-equatorial atmospheric heat transport, required by zonal-mean energy budget constraints (Hwang and Frierson, 2013; Hwang et al., 2017; Kang et al., 2009, 2008, 2020). The latter is often studied

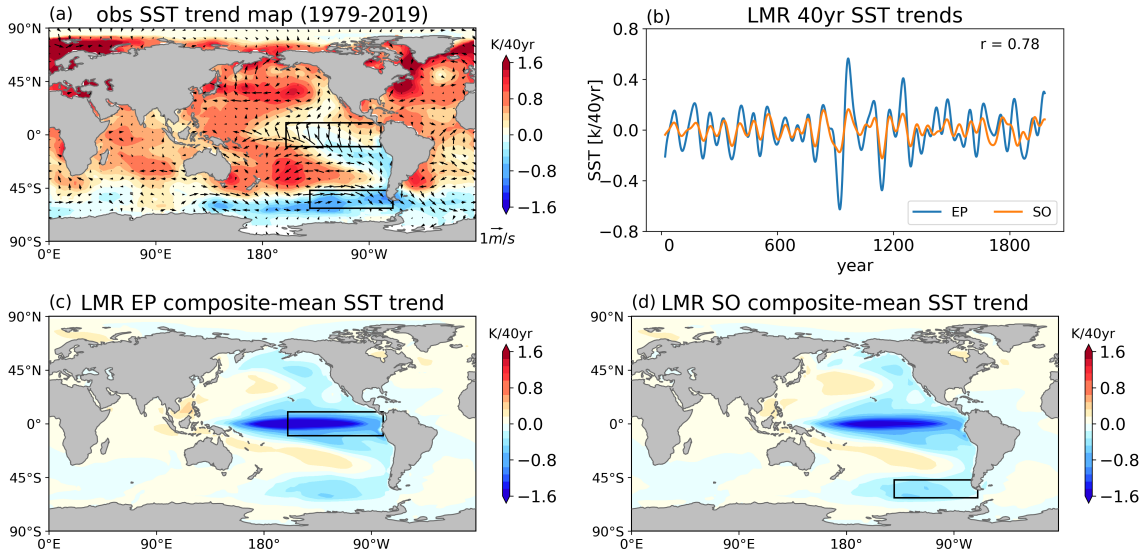

Figure 4.1: (a) Observed annual-mean SST (shading) and 10m surface wind (arrows) trends over 1979–2019 from ERSSTv5b (Huang et al. (2017a)) and ERA5 Reanalysis data, respectively. (b) Running 40yr-trend of SSTs averaged over the tropical EP region (10°S–10°N, 160°W–80°W) and SO region (62°S–47°S,140°W–70°W) from the Last Millennium Reanalysis dataset (Tardif et al., 2019). The SSTs are detrended and 30yr low-pass-filtered before computing the trends. (c, d) The composite-mean SST trend patterns associated with significant EP cooling (c) or SO cooling (d). The EP and SO regions are illustrated by the black patches in panels a, c and d.

using paleoclimate records and atmosphere-ocean coupled models, where the temperature changes of the tropical upwelled waters are traced to the temperature changes of the extra-tropical subducted waters, through mean advection of subtropical cells (Burls and Fedorov, 2014; Fedorov et al., 2015; Gu and Philander, 1997; Heede et al., 2020).

Indeed, we find that SSTs over these two key regions (patches in Fig. 4.1) closely co-vary with each other on decadal timescales in the past 2000 years in a paleo dataset - the Last Millennium Reanalysis version 2.0 (LMR) (Tardif et al., 2019). This paleo reconstruction dataset is derived from the Last Millennium simulations of the Community Climate System Model version 4 (CCSM4), combined with proxy data and linear forward models. In Fig. 4.1b, we show the running 40-yr trends of annual-mean reconstructed SSTs that have been detrended and 30-yr low-pass filtered, averaged over the tropical eastern Pacific (10°–10°N, 160°W–80°W, hereafter denoted as "EP") and part of the Southern Ocean that has cooled the most in recent decades (62°S–47°S, 140°W–70°W, hereafter "SO"). Both regions exhibit low-frequency variabilities that resemble each other at a high correlation of 0.78. We then build SST composite maps of EP warming/cooling decades and SO warming/cooling decades, to look into potential connections between these two regions. Specifically, for EP composites, we average the 40-yr trend maps of global SSTs over the 40-yr periods where EP warming or cooling trends exceed two standard deviation. Taking the difference between the warming and cooling composite-mean SST trend maps (cooling minus warming) illustrates how global SSTs change when the EP region substantially cools on decadal timescales (Fig. 4.1c). Same process is applied for the SO composite based on SO 40-yr SST trends (Fig. 4.1d). The mean SST trend maps of EP composite and SO composite show a remarkable similarity (Figs.4.1 c, d), with cooling co-occurred in both regions, as expected from the high correlation in Fig. 4.1b. More interestingly, this common pattern broadly resembles the pattern of observed SST trends in the Pacific over the past 40yrs (Fig. 4.1a), both highlighting the cooling in the tropical eastern Pacific and part of the Southern Ocean near the southeast Pacific.

These findings suggest that the observed decadal cooling trends in the tropical Pacific and the Southern Ocean may be mutually connected with each other and that there may be a two-way teleconnection between these two regions. While the teleconnection from the

tropics to the extratropics has been well established, what is less understood is how the Southern Ocean SSTs influence the tropical Pacific SSTs if this direction of the teleconnection also exists. Thus, the key questions that we aim to answer in this study are: is the observed tropical eastern Pacific cooling connected to the observed Southern Ocean cooling? If so, what is the mechanism for the two-way teleconnection between these two regions? Furthermore, what implications does this teleconnection have on our interpretation of the recent and future global warming patterns? In the following section, we first describe our idealized simulations using a slab-ocean model to study the Southern Ocean-to-tropics teleconnections. In section 4.3, we propose a new mechanism for the two-way teleconnection between the tropical Pacific and Southern Ocean, with a dynamic feedback through atmospheric circulations. In section 4.4, we show our proposed atmospheric pathway operated in two recently-published studies using fully-coupled models with presence of dynamical oceans. In section 4.5, we summarize the paper and discuss potential caveats and implications of this work.

4.2 Idealized Southern Ocean thermal forcing experiments within a slab-ocean model

4.2.1 Model setup and experiment design

We first investigate the pathways linking tropical Pacific SST changes and Southern Ocean SST changes using a slab-ocean model prescribed with anomalous ocean heat flux convergence ("qflux"). We use a slab-ocean version of the Community Atmospheric Model version 4 (CAM4), with a uniform and annual-mean mixed-layer depth of 50m. The horizontal resolution of CAM4 is 1.9° latitude × 2.5° longitude. There is no interactive ocean dynamics in this mixed-layer slab-ocean model, which allows us to separate atmospheric processes and air-sea thermal coupling from the fully coupled system. In section 4.4, we further examine the atmospheric pathways we found in the slab-ocean model in two fully-coupled model studies.

We first perform a control run and two experiments with anomalous qflux imposed in the EP and SO regions – the two regions where SSTs may be mutually connected based on recent observations and the LMR dataset of the last two millenniums. Both the control run

and the experiments have all radiative forcing agents fixed at year 2000 level. For the control run, we use an annual-mean qflux climatology constructed from a pre-industrial control run of the parent fully-coupled model CCSM4, which has been nudged to reproduce the observed tropical SST mean-state through adding an annual-cycle of additional surface heat fluxes, known as the "flux correction" technique (Hu and Fedorov, 2018; Zhang et al., 2018). This adjustment largely reduces the common biases of model mean states, such as too-cold bias of cold tongue SSTs (Capotondi et al., 2020), too-excessive precipitation off the equator known as the "double Intertropical Convergence Zone (ITCZ)" problem (Li and Xie, 2014), and the bias in the cross-equatorial winds (Hu and Fedorov, 2018). Deriving qflux climatology from the flux-corrected fully-coupled control run thus provides a relatively realistic tropical mean state of SST, precipitation and surface winds in the slab-ocean model we used (Fig. 4.2a). A caveat is that we only apply this observation-corrected qflux to open waters; for regions where sea ice exists, we use a qflux climatology calculated from a freely-evolved pre-industrial control run of the fully-coupled CCSM4, while keeping the global-mean qflux climatology to be zero (no net gain or loss of heat).

For the qflux-perturbed experiments, we add a constant qflux anomaly of 20 Wm^{-2} (i.e., a heat flux divergence from the mixed layer) on top of the qflux control climatology over the EP or SO patch. As we artificially impose a constant heat sink to the model, the energy in the model is not conserved, the global-mean SSTs are expected to cool towards a new equilibrium to balance the net heat loss. Note that we impose the qflux forcing in the localized regions rather than in zonal bands as in previous studies (Hwang et al., 2017; Kang et al., 2008, 2020; Stuecker et al., 2020), which allows us to investigate mechanisms associated with regional dynamics in a more-realistic configuration. We run both the control and qflux-perturbed simulations for 60 years, and use the last 30-yr averages to compute the equilibrium responses.

4.2.2 Teleconnections between the EP and SO regions in slab-ocean simulations

As expected, the qflux forcing imposed in the EP patch drives remote SST changes extended to the extratropics, yielding SST cooling near the SO patch in the southeast Pacific

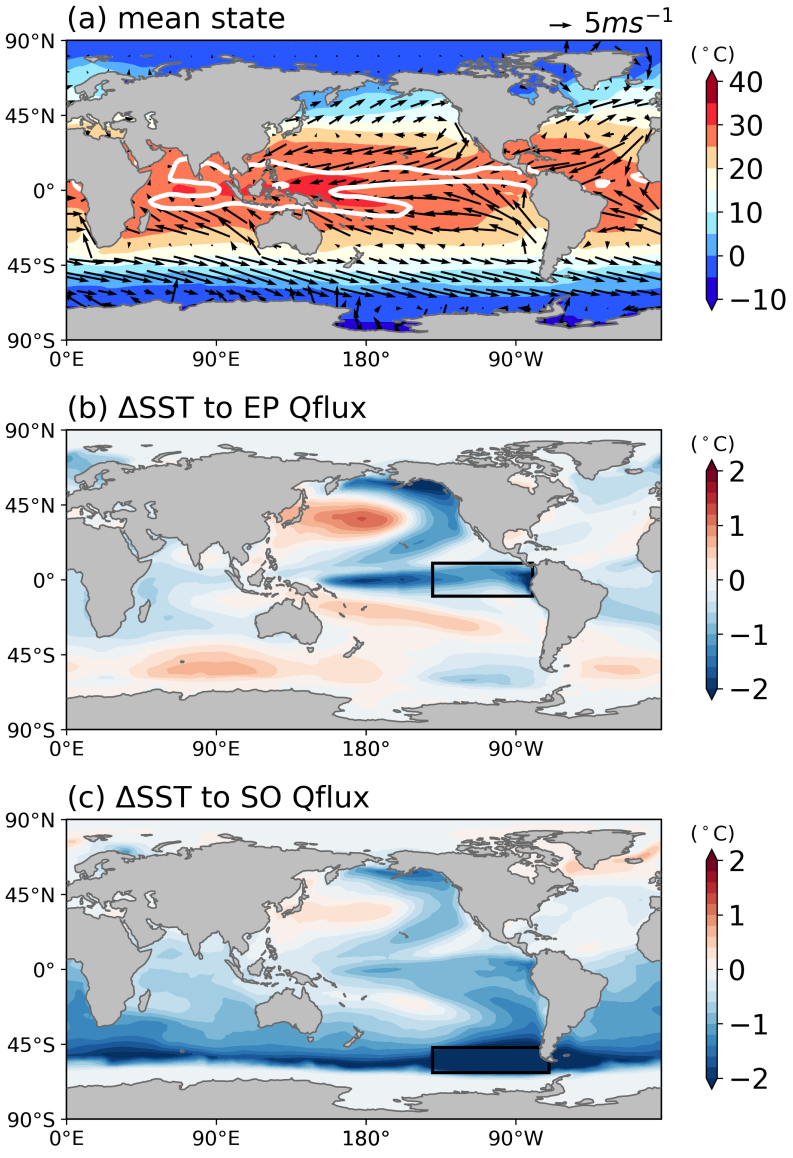

Figure 4.2: (a) Mean state climate of the slab-ocean control run. Shading denotes SSTs; arrows denote surface winds, white contour denotes 6mm/day mean precipitation. (b, c) SST response to the qflux anomaly imposed in the tropical eastern Pacific ("EP") or the Southern Ocean ("SO"), respectively. The location of the qflux forcing is illustrated by the black patch.

(Fig. 4.2b). In turn, the qflux forcing imposed in the SO patch also drives substantial tropical cooling, with more cooling in the eastern Pacific than in the western Pacific, producing a La Niña-like tropical SST pattern (Fig. 4.2c). The above two simulations are consistent with the results of the LMR dataset – the tropical eastern Pacific and the Southern Ocean near the southeast Pacific can be influenced by each other. Moreover, the results from the slab-ocean model suggest that the teleconnection between these regions can be established through atmospheric pathways without ocean circulations.

The prevailing atmospheric pathway proposed for the extratropics-to-tropics teleconnection is linked to a zonal-mean energetic constraint, derived from idealized simulations with zonal-mean extratropical thermal forcing (Hwang et al., 2017; Kang et al., 2008, 2020). That is, an anomalous inter-hemispheric gradient in radiative forcing is expected to induce anomalous cross-equatorial atmospheric heat transport, accomplished via Hadley cell adjustment. As a result, the ITCZ tends to shift towards warmer hemisphere, along with changes in the surface winds and zonal SST contrast through wind-evaporation-SST (WES) feedback (Xie and Philander, 1994).

To test this theory, we next show three similar slab-ocean experiments, with the same zonal-mean qflux forcing imposed on the same latitudes (55°S–35°S) but over different longitude bands. Here we add a uniform qflux anomaly of 15 Wm^{-2} (heat flux divergence from the mixed layer) in the southwest Pacific (130°E–170°W), southeast Pacific (140°W–80°W) and south Atlantic (60°W–0°). These patches are located slightly north of the SO patch shown previously, to avoid potential impacts of changes to the sea-ice edge. All three patch-simulations are run for 60 years, following the same setup described in the previous section.

In all cases, the imposed qflux forcing drives broad surface cooling and precipitation increase in the northern branch of the ITCZ, consistent with previous studies (Hwang et al., 2017; Kang et al., 2020). The zonal-mean precipitation changes (Fig. 4.3g) and zonal-mean SST changes (Fig. 4.3h) are similar across cases, suggesting that the zonal-mean climate changes are indeed largely determined by the zonal-mean forcing. However, the spatial patterns of tropical SST changes vary by case. The tropical eastern Pacific cools much more than the tropical western Pacific in response to the qflux forcing imposed in the southeast

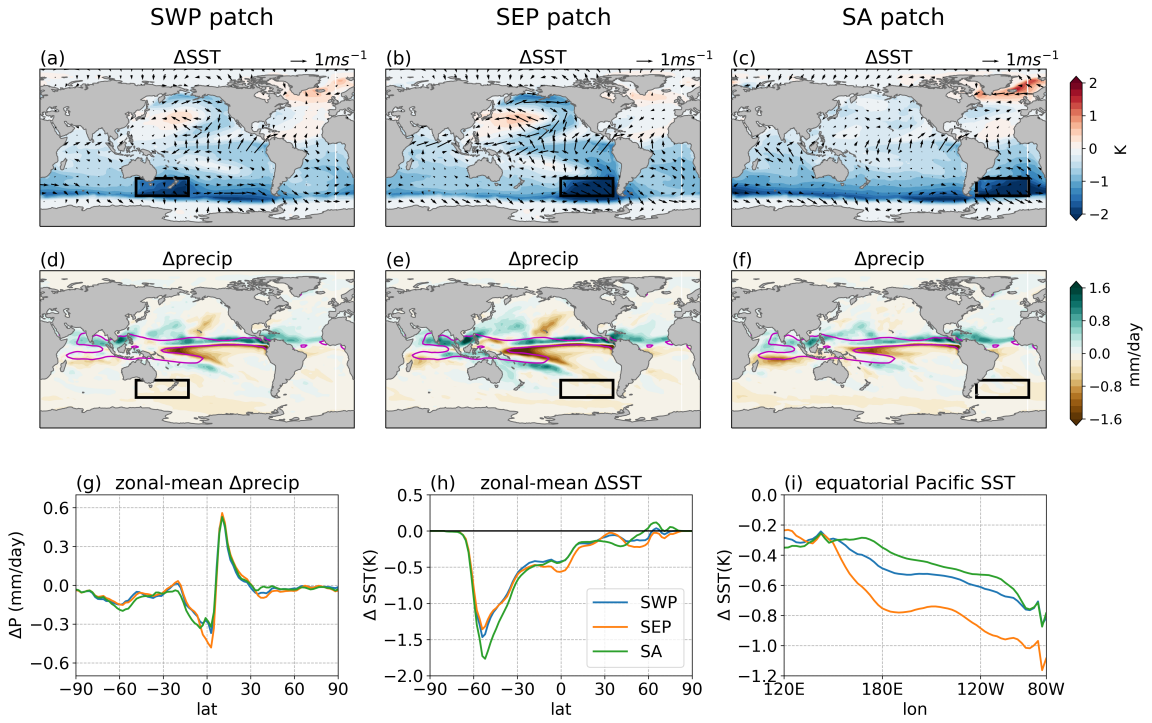

Figure 4.3: Responses to qflux anomaly imposed in the southwest Pacific (left), southeast Pacific (middle) and south Atlantic (right). (a-c) Changes in SST (shading) and surface winds (arrows). (d-f) Changes in precipitation. Pink lines denote the mean-state precipitation of 6 mm/day from control run (same as the white contour in Fig. 4.2a). (g) zonal mean changes of precipitation. (h) zonal mean changes of SST. (i) Changes of SST in the equatorial Pacific averaged over 5°S – 5°N.

Pacific (Fig. 4.3b), but this La Niña-like pattern is less prominent in the other two runs (Figs. 4.3a, c), suggesting that the Southern Ocean – tropics teleconnection is not solely dependent on the zonal mean forcing. More interestingly, the strongest teleconnection to the tropical Pacific is from the southeast Pacific, which is also the region in the Southern Ocean that is most influenced by the tropical qflux forcing (Fig. 4.2b) and where observations have showed the greatest cooling trends since 1980 (Fig. 4.1a). A key question is: why does this region produce a particularly strong Southern Ocean – tropical Pacific teleconnection?

4.3 Mechanisms for the Southern Ocean – tropical Pacific atmospheric teleconnection

4.3.1 Slab-ocean transient responses highlight the role of atmospheric circulations

To understand how the tropical Pacific SST response to the SEP qflux forcing has developed, next we look into the time-evolution of transient responses. We performed an ensemble of 20 members with the same SEP qflux forcing; each is branched from a different day of January in the control run and is run for 6 years. We present results from the average of the 20 ensemble members, to reduce noise from random natural variability.

Fig. 4.4 shows that the Southern Ocean SSTs over the patch of qflux forcing cool substantially, with relatively little cooling outside the patch, over the first 2 years. But by year 3, the cooling signal begins to reach into the tropical Pacific, forming a weak contrast in zonal SST changes. Despite substantial SST changes in the tropical eastern Pacific, there is not much significant change to the surface winds over the tropical Pacific. This hints to the leading process that contributes to the teleconnection at this early stage – advection by climatological mean winds. The mean-state surface westerlies over the southeast Pacific patch blow towards the Andes in high latitudes, but deflect into trade winds blowing off the coast in lower latitudes (Fig. 4.2a), which can efficiently advect surface temperature anomalies from the southeast Pacific to the tropical eastern Pacific. Note that the tropics have only cooled weakly up to this point, suggesting that this advection process only accounts for a small portion of the ultimate tropical cooling response to the Southern Ocean qflux forcing.

This first stage of the mean-wind advection is followed by a more substantial tropical Pacific cooling. Beginning in year 4, a massive cooling develops in the eastern Pacific which extends to the central and western Pacific, associated with an anomalous cold advection by strengthened trade winds. The strengthening of the trade winds is traced to changes in the circulation, featuring a high sea-level pressure (SLP) anomaly in the Southern Hemisphere (SH) subtropical high. The patterns of tropical Pacific SSTs, surface winds and the subtropical SLP observed in year 4 broadly persist to equilibrium (Fig. 4.4). This result reveals another stage that accounts for the major part of the tropical responses towards

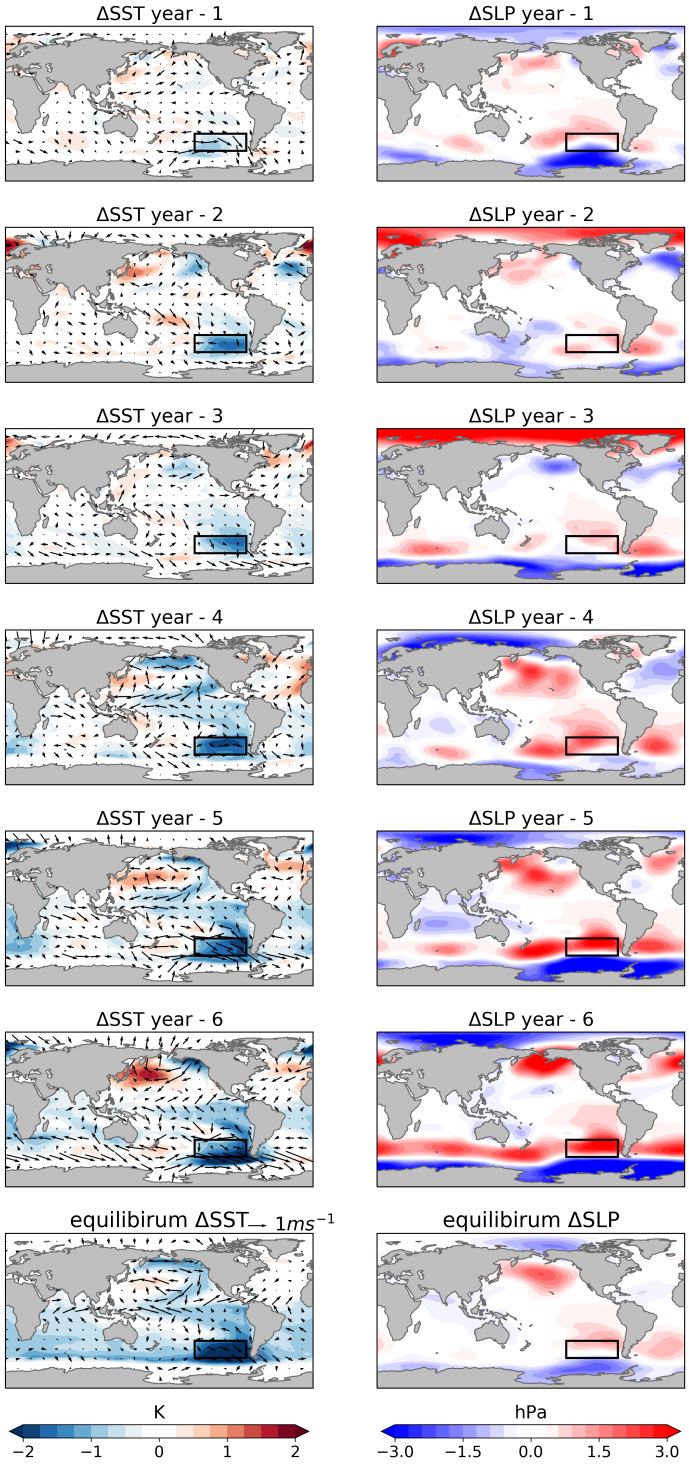

Figure 4.4: Annual mean changes of SST and surface winds (left) and SLP (right) in the first 6 years averaged over the 20 ensemble members with the southeast Pacific qflux. The bottom panels show the equilibrium responses (from a single equilibrium run averaged over years 31-60).

equilibrium: the deepening of the subtropical high SLP strengthens surface winds, which enhances the tropical surface cooling by increasing evaporation via the WES feedback.

From these transient responses, we observe two stages of the development of tropical Pacific cooling in response to the southeast Pacific qflux forcing. First, a small portion of the extratropical cooling in the southeast Pacific region can propagate to the tropical eastern Pacific through advection by climatological mean winds. Second, the tropical cooling can be amplified by the strengthened trade winds, which are driven by the high SLP anomalies in the subtropics. What remains unclear is: what caused the change in the subtropical SLP that is key to this teleconnection? Specifically, is the SLP change a direct response to the imposed Southern Ocean cooling, or does it arise due to the tropical SST change that emerges prior to the SLP change?

4.3.2 Prescribed-SST simulations trace the circulation changes to tropical SST forcing

To investigate the impacts of regional SST changes on the subtropical SLP, in this section we use a set of prescribed-SST simulations, where we prescribe the annual-mean equilibrium SST anomalies induced by the SEP qflux forcing onto different regions separately. We use the atmospheric component of the coupled model, CAM4, where SST and sea-ice concentration are prescribed but the atmosphere can freely adjust. Consistent with the coupled slab-ocean simulations, the prescribed-SST simulations also used a modern-day observed SST climatology, and all radiative forcing agents are fixed at year 2000 level. Both the control run and experiments with regional SST anomalies are run for 15 years; the responses are averaged over the last 10 years.

In the first simulation, we prescribe SST anomalies only within the SEP patch, while keeping the rest of global oceans unchanged (Fig. 4.5a). We find that this extratropical SST forcing only drives local-scale SLP changes, without much remote influence on the subtropical SLP or tropical surface winds. In the second simulation, we instead prescribe SST anomalies within the tropical Pacific (20°S–20°N, 120°E–80°W), with most of the cooling in the eastern pacific (Fig. 4.5b). This tropical SST forcing, in stark contrast to the extratropical SST forcing, drives significant responses at global scale that are even

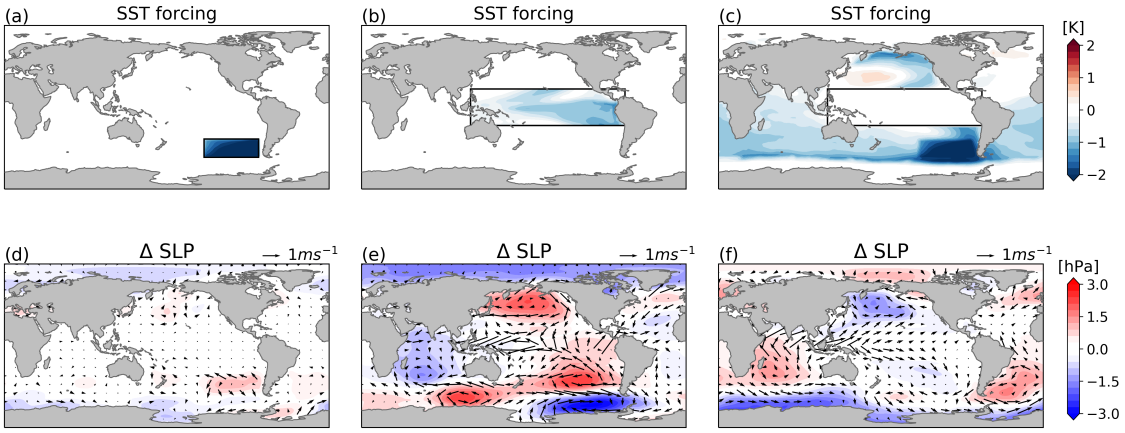

Figure 4.5: Prescribed SST simulations and their responses. (a-c) Prescribed SST anomalies in the southeast Pacific, the tropical Pacific, and global oceans except the tropical Pacific, respectively. (d-f) SLP and surface winds responses to the corresponding SST forcing. All the SST anomalies are taken from the annual-mean equilibrium SST changes in the southeast Pacific qflux experiment (Fig. 4.4 bottom left panel). The tropical Pacific is defined within 120°E – 80°W, 20°S – 20°N.

extended to the poles. Notably, it produces a pattern of SLP and surface winds resembling the pattern of transient climate response starting in year 4 of the SEP slab-ocean run (Fig. 4.4), featuring high SLP anomalies in the subtropics and strengthened southeasterlies in the subtropical and tropical eastern Pacific. Moreover, this tropical Pacific SST forcing also enhances surface westerlies in the southeast Pacific, which could drive more surface cooling over there, as shown in the EP slab-ocean run (Fig. 4.2b). All these tropics-forced extratropical circulation changes have been documented in the literature, through the well-established Rossby wave dynamics (Ding et al., 2011; Li et al., 2021; Meehl et al., 2016; Yuan et al., 2018). To further illustrate the comparison between tropical Pacific SST forcing and extratropical SST forcing, we provide another simulation where we prescribe SST anomalies all over the global oceans except the tropical Pacific (Fig. 4.5c). This broad extratropical SST forcing (also includes some tropical regions in the Indian Ocean and the Atlantic Ocean) has little impact on the SH subtropical SLP in the Pacific sector, and even produces the opposite sign of tropical surface winds.

From the prescribed SST simulations, we identify that the key process of the teleconnection in the slab-ocean runs – the changes to the subtropical SLP and surface winds – are not directly forced by the cooling in the Southern Ocean, but largely forced by the tropical Pacific SST cooling, which themselves can be triggered by the Southern Ocean SST changes through mean-winds advection.

4.3.3 A dynamic positive feedback on the teleconnection

Putting all the evidence together, we propose a two-way teleconnection between the Southern Ocean and tropical Pacific with a dynamic feedback. First, the Southern Ocean cooling near the southeast Pacific can penetrate into the tropical eastern Pacific through advection by climatological mean winds. Once the tropical Pacific SSTs have changed with more cooling in the eastern Pacific, this tropical SST pattern with anomalous convection heating can produce remote changes to the circulation through Rossby wave dynamics. These tropics-forced extratropical circulation changes include: (1) high SLP anomalies over the SH subtropical high near the Andes, which can strengthen the trade winds in the central and eastern Pacific, and therefore enhance surface cooling in the tropical Pacific; (2) low SLP anomalies over the Amundsen Sea Low, which can strengthen surface westerlies over there, enhancing surface cooling in the Southern Ocean, and amplifying the whole teleconnection process. Both of these processes act as a positive feedback on the tropical Pacific response to the Southern Ocean forcing. This positive feedback can also be observed in the transient zonal-mean SST response to the imposed qflux forcing (Fig. 4.6). Starting in year 2, the Southern Ocean SST cooling gradually propagates towards the tropics. Once the tropical SSTs substantially changed around year 3, it immediately amplifies the Southern Ocean cooling and also the tropical cooling itself through the teleconnection.

Has this proposed "dynamic feedback" occurred in observations over the past 40 years? In Fig. 4.7a, we show the 40-yr trend of annual-mean SLP over 1979–2019 from ERA5 reanalysis data (Hersbach et al., 2020). The observed SLP trend pattern highlights positive SLP trends over the SH subtropical high, and negative trends over the Amundsen Sea Low, along with strengthened trade winds in the tropical eastern Pacific and strengthened

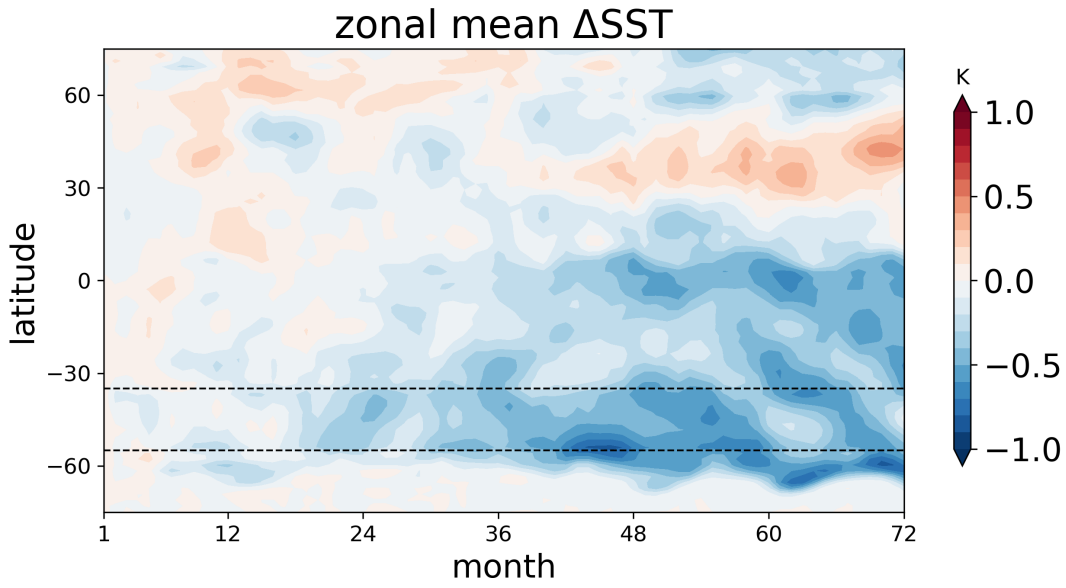

Figure 4.6: Monthly zonal-mean SST response to southeast Pacific qflux forcing over the first 6 years. The dashed lines illustrate the region of the imposed qflux forcing (55°S – 35°S).

westerlies in the SEP region of the Southern Ocean (Fig. 4.1a) – consistent with the results of our simulations. Moreover, the composite-mean SLP trend patterns from the LMR dataset (Figs. 4.7bc), associated with significant cooling trends in the EP and SO regions respectively (Figs. 4.1cd), also show similar features in the subtropics and the Amundsen Sea. These findings suggest that the tropics-forced circulation change, a key process in our proposed two-way teleconnection, has indeed occurred in observations, together with the surface cooling in both tropical eastern Pacific and Southern Ocean.

In summary, based on the simulations we presented so far (Figs. 4.2, 4.4 and 4.5), we argue that there is a two-way teleconnection between the tropical Pacific and the Southern Ocean. The tropical Pacific SST forcing can drive remote changes to the Southern Ocean SSTs, and also subtropical SLP changes that are conducive to amplifying the tropical SST changes; whereas the Southern Ocean SST forcing can also trigger the teleconnection to the tropical Pacific through advection by mean-state winds. This two-way teleconnection implies that the observed decadal-scale surface cooling in the tropical eastern Pacific and Southern Ocean may be mutually connected and amplified by each other.

However, these findings are insufficient to determine whether the observed teleconnection is activated by the tropical change or the Southern Ocean change in the first place, and whether the initial surface cooling (over either of these two regions) is driven by internal variability or anthropogenic forcings. While the underlying causes of the observed SST trend patterns remain to be further investigated, in the following two sections, we discuss one possible perspective that the observed tropical Pacific cooling trends may be traced to recent changes in the Southern Ocean.

4.4 Tropical Pacific SST response to Southern Ocean non-thermal forcings in fully-coupled simulations

Having established a mechanism for the two-way atmospheric teleconnection between the tropical Pacific and the Southern Ocean, next we focus on two recently published studies that applied non-thermal forcings over the Southern Ocean in fully-coupled GCMs, which account for the effects of Antarctic freshwater discharge (section 4.4.1) and intensified winds over the Southern Ocean (section 4.4.2). By showing the results of tropical SST responses in

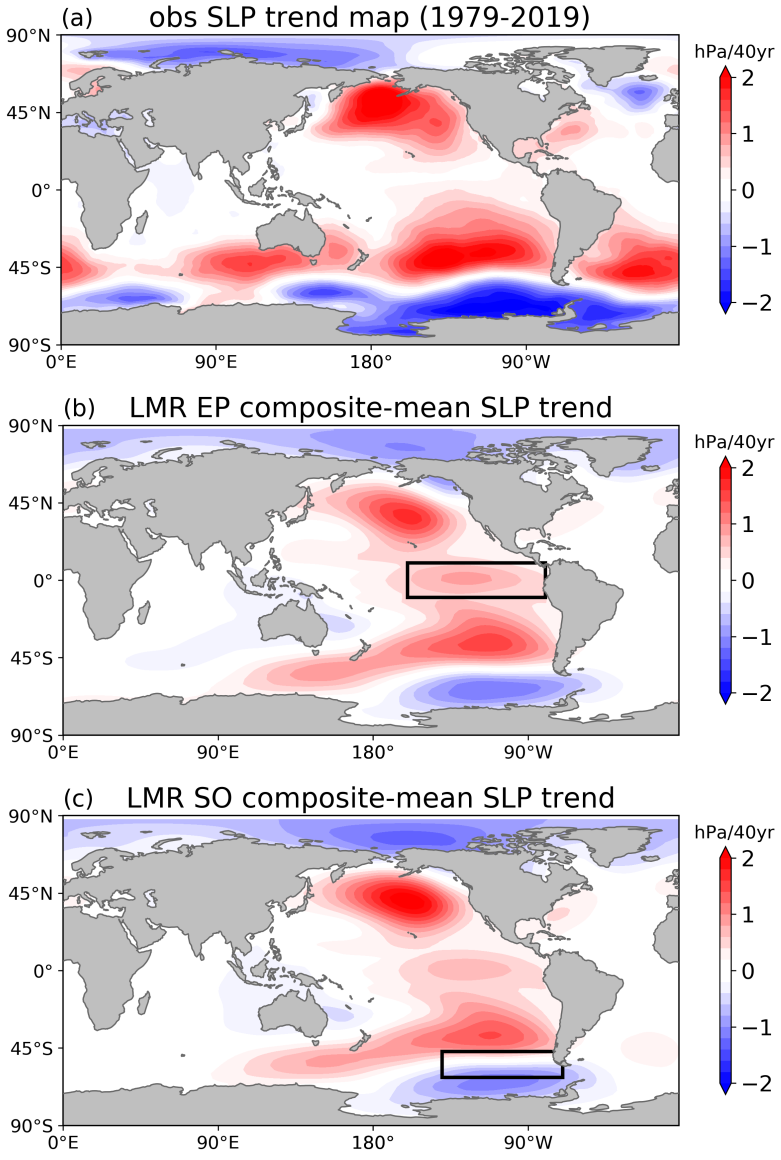

Figure 4.7: (a) Observed annual-mean SLP trends over 1979–2019 from ERA5 Reanalysis. (b, c) Composite mean of 40yr SLP trends, associated with significant cooling trends in the EP and SO regions respectively (consistent with Figures 4.1cd).

these studies, we address two questions: does the atmospheric teleconnection found in our slab-ocean results also exist in a fully-coupled configuration with the presence of dynamic oceans? What implications does this teleconnection have on the observed and projected warming patterns?

4.4.1 The impacts of Southern Ocean freshwater input

First, we show a set of so-called freshwater "hosing" experiments using the fully-coupled Community Earth System Model version 1 with the Community Atmosphere Model version 5 (CESM1-CAM5), provided by Sadai et al. (2020). These simulations account for freshwater input from Antarctic ice sheet melting over the 21st century – a process that is not represented in CMIP5 and CMIP6 GCMs. Here we present results from two simulations of Sadai et al. (2020): a control run and a hosing run; both are forced under representative concentration pathway (RCP) 8.5 scenario over 2005–2100. The control run, using the default model setup, only has freshwater input less than 0.2 sverdrup throughout the 21st century; while the hosing run adds additional time-variant and spatially-distributed meltwater and ice discharge from Antarctic ice sheets into the Southern Ocean surface (see more details in Sadai et al. 2021). The total amount of the added freshwater input, provided by an offline ice sheet model forced by the same RCP8.5 scenario, reaches to 1 sverdrup at the end of the 21st century (see Fig. 1B in Sadai et al. 2021).

Fig. 4.8 shows the SST and SLP trend maps over the 21st century from the control run and the hosing run of Sadai et al. (2020). While the RCP8.5 forcing results in a considerable amount of warming nearly all over the globe in the control run (Fig. 4.8a), the imposed freshwater input in the hosing run substantially cools the Southern Ocean surface temperatures against global warming (Fig.4.8 c). The addition of the freshwater input also leads to an expansion of sea ice and reduced global-mean surface temperatures as described in Sadai et al. (2020), consistent with earlier studies employing different models with additional freshwater forcing (Bronselaer et al., 2018; Purich et al., 2018; Rye et al., 2020). The Antarctic-freshwater induced Southern Ocean surface cooling in this hosing run is further transported to the tropics, mostly manifested in the eastern Pacific, forming a La

Niña-like warming pattern. Accompanying with the surface temperature teleconnection is a deepening of the SH subtropical high near the Andes (Fig. 4.8f), which could enhance the tropical surface cooling as discussed earlier. Although we cannot rule out the possibility that the presented teleconnection may also come about through oceanic pathways, these fully-coupled simulations show that our proposed atmospheric pathway can effectively operate with the presence of dynamic oceans, and that the teleconnection in the fully-coupled model is similar to our slab-ocean results.

Although the results of Sadai et al. (2020) may depend on the model used, it has important implications for understanding the recent and future global surface warming patterns. A growing body of literature has suggested that the Antarctic freshwater forcing may be (at least partially) responsible for the observed surface cooling and sea-ice expansion over the Southern Ocean (Bintanja et al., 2013; Bronselaer et al., 2018; Purich et al., 2018; Rye et al., 2020). This Southern-Ocean originated surface cooling, based on the teleconnection mechanism we proposed and the results of Sadai et al. (2020), may further transport to the tropics, driving tropical Pacific cooling mostly in the eastern Pacific. This theory provides another plausible explanation for the observed cooling trends in the tropical eastern Pacific and Southern Ocean though atmospheric teleconnections.

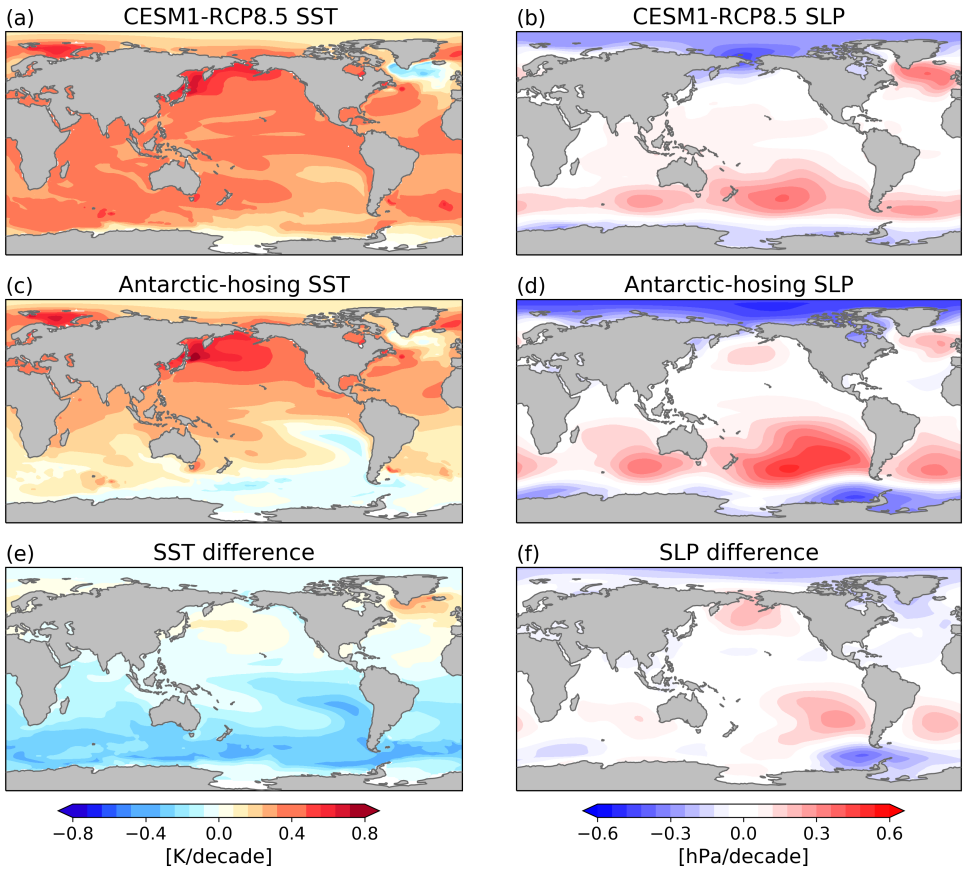

Figure 4.8: SST (left column) and SLP (right column) linear trends over 2005– 2100 from (a) CESM1 RCP8.5 control run and (b) CESM1 Antarctic hosing run with additional freshwater input from the Antarctic ice sheet. Both simulations are under RCP8.5 forcing scenario. (e, f) The difference between the control run and the hosing run that reflects the response to the imposed freshwater forcing. Both simulations are provided by Sadai et al. (2020)

4.4.2 The impacts of Southern Ocean winds

Next, we show an ensemble of Southern Ocean wind-nudging experiments over 1979-2018 (Fig. 4.9), provided by Blanchard-Wrigglesworth et al. (2021). These experiments are performed also using the fully-coupled CESM1-CAM5. All simulations are run under historical radiative forcing from 1979 to 2005 and RCP 8.5 forcing from 2006-2018, consistent with the CESM1 Large Ensemble simulations (LENS; Kay et al. 2015). We present results from the mean of five ensemble members available now (three were newly added after the publication of Blanchard-Wrigglesworth et al. 2021); each member is initiated from a different LENS member from 1 January 1980.

The novelty of these wind-nudging experiments is that, throughout the full period, zonal and meridional winds poleward of 45°S in the SH were nudged to 6-hourly ERA-Interim Reanalysis data (Dee et al., 2011) from 850hPa to the top of model (see more details in Blanchard-Wrigglesworth et al. 2021). Thus, these simulations are directly nudged to reproduce the observed strengthening of the westerly winds over the Southern Ocean, which is generally underestimated in LENS (see Fig. 3 in Blanchard-Wrigglesworth et al. 2021). Furthermore, because the model has to maintain thermal wind balance by increasing SLP gradient in the SH extratropics in response to the intensified polar winds, these wind-nudging experiments also produce positive SLP trend anomalies near the SH subtropical high compared to LENS, largely resembling the observed SLP trend pattern (Fig. 4.9d).

With the high SLP anomalies in the SH subtropics, these wind-nudging experiments surprisingly produce cooling trends in the tropical eastern Pacific, which is not seen in the LENS ensemble-mean, despite the fact that no Southern Ocean SST forcing were directly applied. Although the wind forcing induces some cooling in the Southern Ocean (Fig. 9e), this cooling is much weaker than that observed. Therefore, without strong Southern Ocean cooling to initiate the teleconnection, the tropical eastern Pacific cooling response must be caused by extratropical circulation changes, that is, the second phase of the teleconnection we found in our slab-ocean results: the high SLP anomalies in the subtropics enhance trade winds which further cools the tropical eastern Pacific SSTs. Indeed, in the tropical eastern Pacific, overlying the anomalous surface cooling is the strengthened trade winds in these

wind-nudging experiments (Fig. 9d), which are not found in the LENS ensemble-mean.

Although these wind-nudging experiments only capture part of the mechanism we proposed, the fact that the teleconnection can be established without initial Southern Ocean SST forcing suggests a dominant role of atmospheric circulation (the extratropical SLP) changes in linking the Southern Ocean to the tropical Pacific. Moreover, the results of these fully-coupled simulations suggest that atmospheric forcing can sufficiently drive atmospheric teleconnections even with the presence of dynamical oceans.

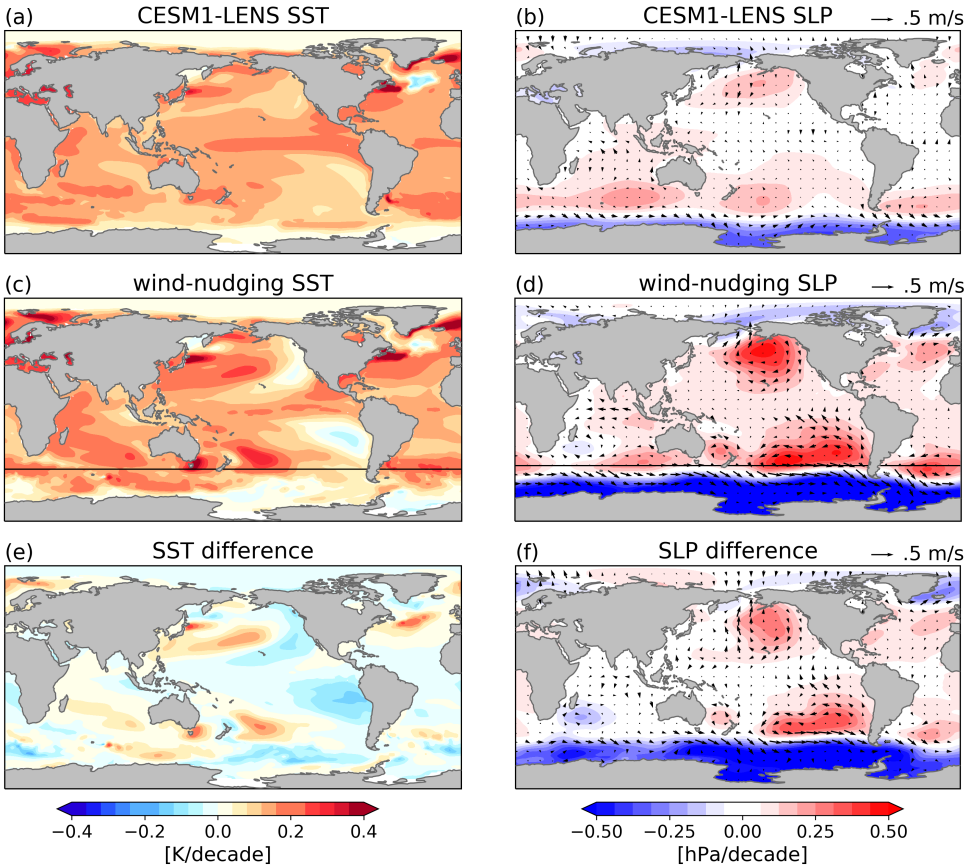

Figure 4.9: SST (left column) and SLP (right colum) linear trends over 1979–2018 from (a, b) CESM1 LENS ensemble mean and (c, d) CESM1 wind-nudging experiments (average of 5 realizations), and (e, f) the difference between the wind-nudging experiments and LENS that reflects the response to the imposed Southern Ocean winds. The wind-nudging experiments are provided by Blanchard-Wrigglesworth et al. (2021)), where the whole column of atmospheric winds poleward of 45°S (the black lines in c, d) were nudged towards ERA-Interim reanalysis.

4.5 Summary and Discussions

Using a set of slab-ocean simulations and fixed-SST simulations, we found that there is a two-way teleconnection between the tropical Pacific and the Southern Ocean. An imposed Southern Ocean cooling can first propagate into the tropics through advection by climatological mean winds over the southeast Pacific. Once the tropical Pacific SSTs have perturbed, this tropical SST forcing can drive remote changes to the extratropical circulation, including high SLP anomalies in the SH subtropical high and low SLP anomalies in the Amundsen Sea Low, yielding strengthened trade winds in the tropics and strengthened surface westerlies in the Southern Ocean. These circulation changes are conducive to further enhancing the surface cooling via the WES feedback in both the tropical eastern Pacific and the southeast Pacific of the Southern Ocean. That is, the tropics-forced circulation changes exert a positive feedback on the two-way teleconnection process. These circulation changes along with the SST changes in the tropical Pacific and the Southern Ocean have also occurred in recent observations and in a paleo reconstruction of the past 2000 years.

Although we did not discuss potential oceanic pathways, we have shown significant tropical Pacific SST responses to changes in the Southern Ocean in two sets of fully-coupled simulations driven by the proposed mechanism. One is the freshwater hosing experiments provided by Sadai et al. (2020), where Southern Ocean SSTs are changed owing to the addition of freshwater input from Antarctic ice sheets. The other is the wind-nudging experiment provided by Blanchard-Wrigglesworth et al. (2021), where the extratropical circulations are changed through nudging the polar winds to observations. Both studies show a La Niña-like tropical SST response with more cooling in the tropical eastern Pacific. The results of these two studies qualitatively corroborate the proposed atmospheric pathway in a fully-coupled configuration linking the tropical Pacific response to Southern Ocean forcings; the quantitative impacts of dynamic oceans on this atmospheric teleconnection need to be further examined.

Although the proposed atmospheric pathway is not sufficient to determine whether the observed SST trend pattern has initially resulted from a tropical cooling or Southern Ocean cooling, we have discussed one possibility that the observed tropical eastern Pacific cooling

trends may be traced to Southern Ocean surface cooling induced by the Antarctic freshwater input. Several earlier studies have suggested that the freshwater discharge from retreating Antarctic ice sheet may be largely responsible for the observed Southern Ocean surface cooling over the recent decades, and may potentially drive muted surface warming over the Southern Ocean in future. If this is the case, the freshwater-driven surface cooling in the Southern Ocean could be teleconnected to the tropics, driving surface cooling in the tropical eastern Pacific as seen in Sadai et al. (2020), which would have greater global impacts. This hypothesis provides a new perspective to the current understanding of the observed tropical Pacific SST trend pattern, accounting for the impacts from the Southern Ocean through atmospheric teleconnections. The results may lead an impetus to revisit the projected long-term warming pattern with enhanced warming in both the Southern Ocean and tropical eastern Pacific from current GCMs, which have no representation of freshwater fluxes.

Meanwhile, we also acknowledge two caveats to our results. First, the results we presented may be sensitive to the model and forcing used in this study. In the slab-ocean simulations, we used an arbitrary qflux forcing (uniform 15 Wm^{-2} at each grid box), though additional simulations with a qflux forcing ranging from 5–20 Wm^{-2} led to the same conclusion (not shown). A stronger idealized thermal forcing in the SH extratropics is also found effective in driving tropical Pacific SST response in other various slab-ocean models (Kang et al., 2020). However, we note a recent "pacemaker" study by Zhang et al. (2021) using CESM1, where the Southern Ocean SSTs are nudged to time-varying observed SST anomalies over 1979–2013, yet produced little change in the tropical Pacific SST trend pattern. We speculate that the results of little tropical Pacific SST response in Zhang et al. (2021) may be owing to the fact that the imposed Southern Ocean cooling is too small to generate significant teleconnection responses in this model. Note that the surface heat fluxes added in Zhang et al. (2021) led to an averaged Southern Ocean (poleward of 40°S) surface cooling of only 0.2°C over the full nudging period, while in our slab-ocean runs, the qflux forcing imposed within the southeast Pacific region alone led to an averaged Southern Ocean SST cooling of 0.8°C. Moreover, in Sadai et al. (2020) which used the same model CESM1, the imposed freshwater forcing led to a Southern Ocean cooling of up to 3°C over the 21st century. As we shown in Fig. 4.4, only part of the Southern Ocean SST cooling can

be transported to the tropics by mean-wind advection in the initial step. Thus, although the Southern Ocean SSTs are nudged towards observed values in Zhang et al. (2021), it is possible that the imposed Southern Ocean cooling is too small in this particular model to trigger the first step of the teleconnection. Additionally, the lack of the second step of the teleconnection (i.e., increased subtropical SLP and strengthened tropical winds) in Zhang et al. (2021) may in part also due to model biases in the tropical mean state, which is largely corrected in our slab-ocean runs. The impacts of model mean-state biases on the Southern ocean - tropics teleconection remain to be further investigated.

Another caveat of this study is the radiative effect of low clouds. Several recent studies have found that low clouds over the tropical eastern Pacific stratocumulus deck play a dominant role in the zonal-mean heat transport and therefore extratropics-tropics teleconnection (Chen et al., 2021; Hwang et al., 2017; Kang et al., 2020; Shin et al., 2021). A surface cooling over the tropical eastern Pacific tends to increase local low clouds, which can efficiently reflect incoming solar radiation back to space and therefore further cool the surface – a positive feedback associated with cloud radiative effects (CRE). Indeed, in our Southern-Ocean qflux simulations, we also observed increases in low cloud cover and enhanced reflection of shortwave radiative fluxes at the top of atmosphere over the tropical eastern Pacific, along with SST cooling over there (not shown). While the impacts of CRE warrant further quantification, we argue that this SST-clouds coupling is initially activated by changes in the tropical Pacific SSTs, which themselves are driven by the imposed Southern Ocean cooling via mean-winds advection. As shown in Fig. 4.4, the qflux forcing imposed in the south Atlantic and southwest Pacific produce weaker tropical eastern Pacific cooling and less low-clouds increases (not shown) than the qflux forcing in the southeast Pacific, even though the cloud physics is unchanged in the model. This is owing to a less-efficient "trigger", i.e., the advection by mean winds near the southeast Pacific, in these two simulations. Thus, although the CRE of low clouds could amplify the tropical eastern Pacific cooling, the initial teleconnection by mean winds is essential to the tropical SST changes.

Understanding how the observed SST trend pattern has developed and how it will evolve in the future is crucial to climate change projections. In this study, we have investigated the possibility that the observed tropical eastern Pacific cooling is connected to the observed

Southern Ocean cooling through a dynamic atmospheric pathway. This mechanism provides a new perspective to our understanding of the tropical response to extratropical forcing, accounting for the regional dynamics and atmospheric circulations. It also raises a possibility that model deficiencies in reproducing the observed tropical Pacific warming pattern may be traced to model deficiencies in accurately representing changes in the Southern Ocean, such as Antarctic freshwater input. If the freshwater input did have large impact on polar and tropical climates as some models suggested, revisiting the current GCM projections on global surface warming patterns and improving polar climate representations may be essential.

Chapter 5

CONCLUSIONS

In Chapter 2, I examined the pattern effect in CMIP5 and CMIP6 models, and confirmed that in most models feedbacks become less negative as SST patterns evolve. Using the Green's function that I developed in my Master Thesis (Dong et al., 2019), I found that the inter-model spread in the pattern effect is primarily governed by different SST patterns in CMIP5 models (less so in CMIP6 models). The results imply that if the observed warming pattern will indeed trend towards GCMs generally projected, we should expect higher values of EffCS than those derived from transient warming states.

However, in Chapter 3, I found that there is a substantial discrepancy between modeled and observed SST patterns over recent decades. In particular, fully-coupled GCMs under historical forcings fail to reproduce the observed cooling trends in the tropical eastern Pacific and the Southern Ocean, which leads to biased estimates of EffCS from historical simulations compared to those from observed historical energy budget constraints. Therefore, understanding the causes of the recent observed warming pattern and making accurate projections of future warming patterns are important for constraining transient and equilibrium climate change.

Thus, in Chapter 4, I investigated the causes of the observed tropical Pacific SST pattern, focusing on the impacts from the Southern Ocean, and asked whether the observed decadal cooling in these two regions are connected. I found that there is a two-way atmospheric teleconnection between the tropical Pacific and the Southern Ocean, where atmospheric circulations exert a positive feedback in building the teleconnection. These results imply that model deficiencies in reproducing the observed tropical Pacific SST pattern may be traced to model deficiencies in correctly representing changes in the Southern Ocean. One of the possible drivers I discussed in Chapter 4 was freshwater input from Antarctic ice sheet melting, which is not included in CMIP5 and CMIP6 GCMs but proposed to be

largely responsible for the observed Southern Ocean cooling.

The above chapters altogether point to the importance of understanding the causes of the observed global surface warming pattern and the model-observation discrepancy in the recent surface warming pattern. Yet there still remain a number of open questions. For example, I explored the possibility that the observed tropical cooling was caused (in part) by teleconnections from the Southern Ocean cooling driven by Antarctic freshwater forcing, using results from one model (CESM1). How reliable are the results based on this single model? If the tropical SST response to Antarctic freshwater forcing varies by model, would different tropical SST results mostly stem from model differences in the Southern Ocean (e.g., ocean circulations) or the tropics (e.g., tropical mean state winds, tropical cloud feedbacks)? Moreover, does accounting for freshwater input in a model change the model projected near-equilibrium warming pattern and the model's ECS? Regarding these questions, an inter-model comparison study (with the same amount of freshwater input for example) would be valuable to assess the remote impacts of Antarctic freshwater forcing through teleconnections.

In summary, understanding the extent to which the recent observed surface warming pattern was caused by external forcing or internal variability, and how local processes and remote teleconnections respectively influenced the global surface warming pattern has important implications for climate science. The answers would not only benefit model development, but would improve our understanding of climate dynamics and better constrain future climate projections under GHG forcing.

BIBLIOGRAPHY

Andrews, T., Andrews, M. B., Bodas-Salcedo, A., Jones, G. S., Kuhlbrodt, T., Manners, J., et al. (2019). Forcings, feedbacks, and climate sensitivity in HadGEM3-GC3.1 and UKESM1. *Journal of Advances in Modeling Earth Systems*, 11(12):4377–4394.

Andrews, T., Gregory, J. M., Paynter, D., Silvers, L. G., Zhou, C., Mauritsen, T., et al. (2018). Accounting for changing temperature patterns increases historical estimates of climate sensitivity. *Geophysical Research Letters*, 45(16):8490–8499.

Andrews, T., Gregory, J. M., and Webb, M. J. (2015). The dependence of radiative forcing and feedback on evolving patterns of surface temperature change in climate models. *Journal of Climate*, 28(4):1630–1648.

Andrews, T., Smith, C. J., Myhre, G., Forster, P. M., Chadwick, R., and Ackerley, D. (2021). Effective radiative forcing in a GCM with fixed surface temperatures. *Journal of Geophysical Research: Atmospheres*, 126(4):e2020JD033880.

Andrews, T. and Webb, M. J. (2018). The dependence of global cloud and lapse rate feedbacks on the spatial structure of tropical Pacific warming. *Journal of Climate*, 31(2):641–654.

Armour, K. C. (2017). Energy budget constraints on climate sensitivity in light of inconstant climate feedbacks. *Nature Climate Change*, 7(5):331–335.

Armour, K. C., Bitz, C. M., and Roe, G. H. (2013). Time-varying climate sensitivity from regional feedbacks. *Journal of Climate*, 26(13):4518–4534.

Armour, K. C., Marshall, J., Scott, J. R., Donohoe, A., and Newsom, E. R. (2016). Southern ocean warming delayed by circumpolar upwelling and equatorward transport. *Nature Geoscience*, 9(7):549–554.

Bintanja, R., van Oldenborgh, G. J., Drijfhout, S., Wouters, B., and Katsman, C. (2013). Important role for ocean warming and increased ice-shelf melt in Antarctic sea-ice expansion. *Nature Geoscience*, 6(5):376–379.

Bjordal, J., Storelvmo, T., Alterskjær, K., and Carlsen, T. (2020). Equilibrium climate sensitivity above 5 c plausible due to state-dependent cloud feedback. *Nature Geoscience*, 13(11):718–721.

Blanchard-Wrigglesworth, E., Roach, L. A., Donohoe, A., and Ding, Q. (2021). Impact of winds and southern ocean SSTs on Antarctic sea ice trends and variability. *Journal of Climate*, 34(3):949–965.

Bloch-Johnson, J., Pierrehumbert, R. T., and Abbot, D. S. (2015). Feedback temperature dependence determines the risk of high warming. *Geophysical Research Letters*, 42(12):4973–4980.

Bloch-Johnson, J., Rugenstein, M., Stolpe, M. B., Rohrschneider, T., Zheng, Y., and Gregory, J. M. (2021). Climate sensitivity increases under higher CO_2 levels due to feedback temperature dependence. *Geophysical Research Letters*, 48(4):e2020GL089074.

Bodas-Salcedo, A., Mulcahy, J., Andrews, T., Williams, K., Ringer, M., Field, P., and Elsaesser, G. (2019). Strong dependence of atmospheric feedbacks on mixed-phase microphysics and aerosol-cloud interactions in hadgem3. *Journal of Advances in Modeling Earth Systems*, 11(6):1735–1758.

Bony, S., Colman, R., Kattsov, V. M., Allan, R. P., Bretherton, C. S., Dufresne, J.-L., Hall, A., Hallegatte, S., Holland, M. M., Ingram, W., et al. (2006). How well do we understand and evaluate climate change feedback processes? *Journal of Climate*, 19(15):3445–3482.

Bronselaer, B., Winton, M., Griffies, S. M., Hurlin, W. J., Rodgers, K. B., Sergienko, O. V., Stouffer, R. J., and Russell, J. L. (2018). Change in future climate due to Antarctic meltwater. *Nature*, 564(7734):53–58.

Burls, N. and Fedorov, A. (2014). What controls the mean east-west sea surface temperature gradient in the equatorial Pacific: The role of cloud albedo. *Journal of Climate*, 27(7):2757–2778.

Caballero, R. and Huber, M. (2013). State-dependent climate sensitivity in past warm climates and its implications for future climate projections. *Proceedings of the National Academy of Sciences*, 110(35):14162–14167.

Cabré, A., Marinov, I., and Gnanadesikan, A. (2017). Global atmospheric teleconnections and multidecadal climate oscillations driven by Southern Ocean convection. *Journal of Climate*, 30(20):8107–8126.

Caldwell, P. M., Zelinka, M. D., and Klein, S. A. (2018). Evaluating emergent constraints on equilibrium climate sensitivity. *Journal of Climate*, 31(10):3921–3942.

Caldwell, P. M., Zelinka, M. D., Taylor, K. E., and Marvel, K. (2016). Quantifying the sources of intermodel spread in equilibrium climate sensitivity. *Journal of Climate*, 29(2):513–524.

Capotondi, A., Deser, C., Phillips, A., Okumura, Y., and Larson, S. (2020). ENSO and pacific decadal variability in the Community Earth System Model version 2. *Journal of Advances in Modeling Earth Systems*, 12(12):e2019MS002022.

Ceppi, P., Brient, F., Zelinka, M. D., and Hartmann, D. L. (2017). Cloud feedback mechanisms and their representation in global climate models. *Wiley Interdisciplinary Reviews: Climate Change*, 8(4):e465.

Ceppi, P. and Gregory, J. M. (2017). Relationship of tropospheric stability to climate sensitivity and Earth's observed radiation budget. *Proceedings of the National Academy of Sciences*, 114(50):13126–13131.

Chen, Y.-J., Hwang, Y.-T., and Ceppi, P. (2021). The impacts of cloud-radiative changes on poleward atmospheric and oceanic energy transport in a warmer climate. *Journal of Climate*, 34(19):7857–7874.

Coats, S. and Karnauskas, K. (2018). A role for the equatorial undercurrent in the ocean dynamical thermostat. *Journal of Climate*, 31(16):6245–6261.

Coats, S. and Karnauskas, K. B. (2017). Are simulated and observed twentieth century tropical Pacific sea surface temperature trends significant relative to internal variability? *Geophysical Research Letters*, 44(19):9928–9937.

Dee, D. P., Uppala, S. M., Simmons, A., Berrisford, P., Poli, P., Kobayashi, S., Andrae, U., Balmaseda, M., Balsamo, G., Bauer, d. P., et al. (2011). The ERA-Interim reanalysis: Configuration and performance of the data assimilation system. *Quarterly Journal of the royal meteorological society*, 137(656):553–597.

Dessler, A. E. (2020). Potential problems measuring climate sensitivity from the historical record. *Journal of Climate*, 33(6):2237–2248.

Dessler, A. E., Mauritsen, T., and Stevens, B. (2018). The influence of internal variability on Earth's energy balance framework and implications for estimating climate sensitivity. *Atmospheric Chemistry and Physics*, 18(7):5147–5155.

Ding, Q., Steig, E. J., Battisti, D. S., and Küttel, M. (2011). Winter warming in west antarctica caused by central tropical Pacific warming. *Nature geoscience*, 4(6):398–403.

Ding, Q., Steig, E. J., Battisti, D. S., and Wallace, J. M. (2012). Influence of the tropics on the southern annular mode. *Journal of Climate*, 25(18):6330–6348.

Dong, Y., Armour, K. C., Zelinka, M. D., Proistosescu, C., Battisti, D. S., Zhou, C., and Andrews, T. (2020). Intermodel spread in the pattern effect and its contribution to climate sensitivity in CMIP5 and CMIP6 models. *Journal of Climate*, 33(18):7755–7775.

Dong, Y., Proistosescu, C., Armour, K. C., and Battisti, D. S. (2019). Attributing historical and future evolution of radiative feedbacks to regional warming patterns using a Green's function approach: The preeminence of the western Pacific. *Journal of Climate*, 32(17):5471–5491.

Dufresne, J.-L. and Bony, S. (2008). An assessment of the primary sources of spread of global warming estimates from coupled atmosphere-ocean models. *Journal of Climate*, 21(19):5135–5144.

Dunne, J. P., Winton, M., Bacmeister, J., Danabasoglu, G., Gettelman, A., Golaz, J.-C., Hannay, C., Schmidt, G. A., Krasting, J. P., Leung, L. R., et al. (2020). Comparison of equilibrium climate sensitivity estimates from slab ocean, 150-year, and longer simulations. *Geophysical Research Letters*, 47(16):e2020GL088852.

England, M. H., McGregor, S., Spence, P., Meehl, G. A., Timmermann, A., Cai, W., Gupta, A. S., McPhaden, M. J., Purich, A., and Santoso, A. (2014). Recent intensification of wind-driven circulation in the Pacific and the ongoing warming hiatus. *Nature climate change*, 4(3):222–227.

Eyring, V., Bony, S., Meehl, G. A., Senior, C. A., Stevens, B., Stouffer, R. J., and Taylor, K. E. (2016). Overview of the Coupled Model Intercomparison Project Phase 6 (CMIP6) experimental design and organization. *Geoscientific Model Development*, 9(5):1937–1958.

Fan, T., Deser, C., and Schneider, D. P. (2014). Recent Antarctic sea ice trends in the context of Southern Ocean surface climate variations since 1950. *Geophysical Research Letters*, 41(7):2419–2426.

Fedorov, A. V., Burls, N. J., Lawrence, K. T., and Peterson, L. C. (2015). Tightly linked zonal and meridional sea surface temperature gradients over the past five million years. *Nature Geoscience*, 8(12):975–980.

Flato, G., Marotzke, J., Abiodun, B., Braconnot, P., Chou, S. C., Collins, W., Cox, P., Driouech, F., Emori, S., Eyring, V., et al. (2014). Evaluation of climate models. pages 741–866.

Forster, P. (2016). Inference of climate sensitivity from analysis of Earth's energy budget. *Annual Review of Earth and Planetary Sciences*, 44:85–106.

Forster, P., Richardson, T., Maycock, A. C., Smith, C. J., Samset, B. H., Myhre, G., et al.

(2016). Recommendations for diagnosing effective radiative forcing from climate models for CMIP6. *Journal of Geophysical Research: Atmospheres*, 121(20):12–460.

Forster, P., Storelvmo, T., Amour, K., Collins, W., Dufresne, J., Frame, D., et al. (2021). The Earth's energy budget, climate feedbacks, and climate sensitivity. *Climate Change 2021: The Physical Science Basis. Contribution of Working Group I to the Sixth Assessment Report of the Intergovernmental Panel on Climate Change*.

Forster, P. M., Andrews, T., Good, P., Gregory, J. M., Jackson, L. S., and Zelinka, M. (2013). Evaluating adjusted forcing and model spread for historical and future scenarios in the CMIP5 generation of climate models. *Journal of Geophysical Research: Atmospheres*, 118(3):1139–1150.

Fueglistaler, S. (2019). Observational evidence for two modes of coupling between sea surface temperatures, tropospheric temperature profile, and shortwave cloud radiative effect in the tropics. *Geophysical Research Letters*, 46(16):9890–9898.

Fyfe, J. C., Gillett, N. P., and Zwiers, F. W. (2013). Overestimated global warming over the past 20 years. *Nature Climate Change*, 3(9):767–769.

Gettelman, A., Hannay, C., Bacmeister, J., Neale, R., Pendergrass, A., Danabasoglu, G., Lamarque, J.-F., Fasullo, J., Bailey, D., Lawrence, D., et al. (2019). High climate sensitivity in the community earth system model version 2 (CESM2). *Geophysical Research Letters*, 46(14):8329–8337.

Gillett, N. P., Shiogama, H., Funke, B., Hegerl, G., Knutti, R., Matthes, K., et al. (2016). The Detection and Attribution Model Intercomparison Project (DAMIP v1. 0) contribution to CMIP6. *Geoscientific Model Development*, 9(10):3685–3697.

Gjermundsen, A., Nummelin, A., Olivié, D., Bentsen, M., Seland, Ø., and Schulz, M. (2021). Shutdown of southern ocean convection controls long-term greenhouse gas-induced warming. *Nature Geoscience*, pages 1–8.

Golaz, J.-C., Caldwell, P. M., Van Roekel, L. P., Petersen, M. R., Tang, Q., Wolfe, J. D., Abeshu, G., Anantharaj, V., Asay-Davis, X. S., Bader, D. C., et al. (2019). The DOE

E3SM coupled model version 1: Overview and evaluation at standard resolution. *Journal of Advances in Modeling Earth Systems*, 11(7):2089–2129.

Goosse, H., Kay, J. E., Armour, K. C., Bodas-Salcedo, A., Chepfer, H., Docquier, D., Jonko, A., Kushner, P. J., Lecomte, O., Massonnet, F., et al. (2018). Quantifying climate feedbacks in polar regions. *Nature communications*, 9(1):1–13.

Gregory, J. M. and Andrews, T. (2016). Variation in climate sensitivity and feedback parameters during the historical period. *Geophysical Research Letters*, 43(8):3911–3920.

Gregory, J. M., Andrews, T., Ceppi, P., Mauritsen, T., and Webb, M. (2020). How accurately can the climate sensitivity to CO_2 be estimated from historical climate change? *Climate Dynamics*, 54(1):129–157.

Gregory, J. M., Andrews, T., and Good, P. (2015). The inconstancy of the transient climate response parameter under increasing CO_2. *Philosophical Transactions of the Royal Society A: Mathematical, Physical and Engineering Sciences*, 373(2054):20140417.

Gregory, J. M. and Forster, P. (2008). Transient climate response estimated from radiative forcing and observed temperature change. *Journal of Geophysical Research: Atmospheres*, 113(D23).

Gregory, J. M., Ingram, W. J., Palmer, M. A., Jones, G. S., Stott, P. A., Thorpe, R. B., et al. (2004). A new method for diagnosing radiative forcing and climate sensitivity. *Geophysical research letters*, 31(3).

Gregory, J. M. and Mitchell, J. F. (1997). The climate response to CO_2 of the Hadley Centre coupled AOGCM with and without flux adjustment. *Geophysical Research Letters*, 24(15):1943–1946.

Grose, M. R., Gregory, J., Colman, R., and Andrews, T. (2018). What climate sensitivity index is most useful for projections? *Geophysical Research Letters*, 45(3):1559–1566.

Gu, D. and Philander, S. G. (1997). Interdecadal climate fluctuations that depend on exchanges between the tropics and extratropics. *Science*, 275(5301):805–807.

Hansen, J., Sato, M., Ruedy, R., Nazarenko, L., Lacis, A., Schmidt, G., et al. (2005). Efficacy of climate forcings. *Journal of Geophysical Research: Atmospheres*, 110(D18).

Haugstad, A., Armour, K., Battisti, D., and Rose, B. (2017). Relative roles of surface temperature and climate forcing patterns in the inconstancy of radiative feedbacks. *Geophysical Research Letters*, 44(14):7455–7463.

Heede, U. K. and Fedorov, A. V. (2021). Eastern equatorial Pacific warming delayed by aerosols and thermostat response to co_2 increase. *Nature Climate Change*, 11(8):696–703.

Heede, U. K., Fedorov, A. V., and Burls, N. J. (2020). Time scales and mechanisms for the tropical Pacific response to global warming: A tug of war between the ocean thermostat and weaker walker. *Journal of Climate*, 33(14):6101–6118.

Held, I. M. and Soden, B. J. (2006). Robust responses of the hydrological cycle to global warming. *Journal of climate*, 19(21):5686–5699.

Hersbach, H., Bell, B., Berrisford, P., Hirahara, S., Horányi, A., Muñoz-Sabater, J., Nicolas, J., Peubey, C., Radu, R., Schepers, D., et al. (2020). The ERA5 global reanalysis. *Quarterly Journal of the Royal Meteorological Society*, 146(730):1999–2049.

Hirahara, S., Ishii, M., and Fukuda, Y. (2014). Centennial-scale sea surface temperature analysis and its uncertainty. *Journal of Climate*, 27(1):57–75.

Holland, P. R. and Kwok, R. (2012). Wind-driven trends in Antarctic sea-ice drift. *Nature Geoscience*, 5(12):872–875.

Hu, S. and Fedorov, A. V. (2018). Cross-equatorial winds control El niño diversity and change. *Nature Climate Change*, 8(9):798–802.

Huang, B., Thorne, P. W., Banzon, V. F., Boyer, T., Chepurin, G., Lawrimore, J. H., et al. (2017a). Extended reconstructed sea surface temperature, version 5 (ERSSTv5): upgrades, validations, and intercomparisons. *Journal of Climate*, 30(20):8179–8205.

Huang, Y., Xia, Y., and Tan, X. (2017b). On the pattern of co2 radiative forcing and poleward energy transport. *Journal of Geophysical Research: Atmospheres*, 122(20):10–578.

Hurrell, J. W., Hack, J. J., Shea, D., Caron, J. M., and Rosinski, J. (2008). A new sea surface temperature and sea ice boundary dataset for the Community Atmosphere Model. *Journal of Climate*, 21(19):5145–5153.

Hwang, Y.-T. and Frierson, D. M. (2013). Link between the Double-Intertropical Convergence Zone problem and cloud biases over the Southern Ocean. *Proceedings of the National Academy of Sciences*, 110(13):4935–4940.

Hwang, Y.-T., Xie, S.-P., Deser, C., and Kang, S. M. (2017). Connecting tropical climate change with southern ocean heat uptake. *Geophysical Research Letters*, 44(18):9449–9457.

Kajtar, J. B., Santoso, A., McGregor, S., England, M. H., and Baillie, Z. (2018). Model under-representation of decadal Pacific trade wind trends and its link to tropical Atlantic bias. *Climate dynamics*, 50(3):1471–1484.

Kang, S. M., Frierson, D. M., and Held, I. M. (2009). The tropical response to extratropical thermal forcing in an idealized GCM: The importance of radiative feedbacks and convective parameterization. *Journal of the atmospheric sciences*, 66(9):2812–2827.

Kang, S. M., Held, I. M., Frierson, D. M., and Zhao, M. (2008). The response of the ITCZ to extratropical thermal forcing: Idealized slab-ocean experiments with a GCM. *Journal of Climate*, 21(14):3521–3532.

Kang, S. M., Xie, S.-P., Shin, Y., Kim, H., Hwang, Y.-T., Stuecker, M. F., et al. (2020). Walker circulation response to extratropical radiative forcing. *Science advances*, 6(47):eabd3021.

Kay, J., Hillman, B., Klein, S., Zhang, Y., Medeiros, B., Pincus, R., Gettelman, A., Eaton, B., Boyle, J., Marchand, R., et al. (2012). Exposing global cloud biases in the community atmosphere model (CAM) using satellite observations and their corresponding instrument simulators. *Journal of Climate*, 25(15):5190–5207.

Kay, J. E., Deser, C., Phillips, A., Mai, A., Hannay, C., Strand, G., Arblaster, J. M., Bates, S., Danabasoglu, G., Edwards, J., et al. (2015). The Community Earth System Model (CESM) large ensemble project: A community resource for studying climate change in the presence of internal climate variability. *Bulletin of the American Meteorological Society*, 96(8):1333–1349.

Kociuba, G. and Power, S. B. (2015). Inability of CMIP5 models to simulate recent strengthening of the walker circulation: Implications for projections. *Journal of Climate*, 28(1):20–35.

Kohyama, T., Hartmann, D. L., and Battisti, D. S. (2017). La niña–like mean-state response to global warming and potential oceanic roles. *Journal of Climate*, 30(11):4207–4225.

Kosaka, Y. and Xie, S.-P. (2013). Recent global-warming hiatus tied to equatorial pacific surface cooling. *Nature*, 501(7467):403–407.

Kucharski, F., Syed, F., Burhan, A., Farah, I., and Gohar, A. (2015). Tropical Atlantic influence on Pacific variability and mean state in the twentieth century in observations and CMIP5. *Climate Dynamics*, 44(3):881–896.

Latif, M., Martin, T., and Park, W. (2013). Southern Ocean sector centennial climate variability and recent decadal trends. *Journal of Climate*, 26(19):7767–7782.

Lewis, N. and Curry, J. A. (2015). The implications for climate sensitivity of AR5 forcing and heat uptake estimates. *Climate dynamics*, 45(3):1009–1023.

Lewis, N. and Curry, J. A. (2018). The impact of recent forcing and ocean heat uptake data on estimates of climate sensitivity. *Journal of Climate*, 31(15):6051–6071.

Li, C., von Storch, J.-S., and Marotzke, J. (2013). Deep-ocean heat uptake and equilibrium climate response. *Climate Dynamics*, 40(5-6):1071–1086.

Li, G. and Xie, S.-P. (2014). Tropical biases in CMIP5 multimodel ensemble: The excessive equatorial Pacific cold tongue and double ITCZ problems. *Journal of Climate*, 27(4):1765–1780.

Li, X., Cai, W., Meehl, G. A., Chen, D., Yuan, X., Raphael, M., Holland, D. M., Ding, Q., Fogt, R. L., Markle, B. R., et al. (2021). Tropical teleconnection impacts on Antarctic climate changes. *Nature Reviews Earth & Environment*, pages 1–19.

Li, X., Xie, S.-P., Gille, S. T., and Yoo, C. (2016). Atlantic-induced pan-tropical climate change over the past three decades. *Nature Climate Change*, 6(3):275–279.

Luo, J.-J., Wang, G., and Dommenget, D. (2018). May common model biases reduce CMIP5's ability to simulate the recent pacific la niña-like cooling? *Climate Dynamics*, 50(3):1335–1351.

L'Heureux, M. L., Lee, S., and Lyon, B. (2013). Recent multidecadal strengthening of the walker circulation across the tropical Pacific. *Nature Climate Change*, 3(6):571–576.

L'Heureux, M. L. and Thompson, D. W. (2006). Observed relationships between the el niño–southern oscillation and the extratropical zonal-mean circulation. *Journal of Climate*, 19(2):276–287.

Manabe, S. and Wetherald, R. T. (1967). Thermal equilibrium of the atmosphere with a given distribution of relative humidity. *Journal of the Atmospheric Sciences*, 24(47):241–259.

Marshall, G. J. (2003). Trends in the southern annular mode from observations and reanalyses. *Journal of climate*, 16(24):4134–4143.

Marvel, K., Pincus, R., Schmidt, G. A., and Miller, R. L. (2018). Internal variability and disequilibrium confound estimates of climate sensitivity from observations. *Geophysical Research Letters*, 45(3):1595–1601.

Marvel, K., Schmidt, G. A., Miller, R. L., and Nazarenko, L. S. (2016). Implications for climate sensitivity from the response to individual forcings. *Nature Climate Change*, 6(4):386–389.

McCoy, D. T., Hartmann, D. L., Zelinka, M. D., Ceppi, P., and Grosvenor, D. P. (2015).

Mixed-phase cloud physics and southern ocean cloud feedback in climate models. *Journal of Geophysical Research: Atmospheres*, 120(18):9539–9554.

McGregor, S., Stuecker, M. F., Kajtar, J. B., England, M. H., and Collins, M. (2018). Model tropical Atlantic biases underpin diminished Pacific decadal variability. *Nature Climate Change*, 8(6):493–498.

McGregor, S., Timmermann, A., Stuecker, M. F., England, M. H., Merrifield, M., Jin, F.-F., and Chikamoto, Y. (2014). Recent walker circulation strengthening and Pacific cooling amplified by Atlantic warming. *Nature Climate Change*, 4(10):888–892.

Meehl, G. A., Arblaster, J. M., Bitz, C. M., Chung, C. T., and Teng, H. (2016). Antarctic sea-ice expansion between 2000 and 2014 driven by tropical Pacific decadal climate variability. *Nature Geoscience*, 9(8):590–595.

Meehl, G. A., Hu, A., Castruccio, F., England, M. H., Bates, S. C., Danabasoglu, G., McGregor, S., Arblaster, J. M., Xie, S.-P., and Rosenbloom, N. (2021). Atlantic and Pacific tropics connected by mutually interactive decadal-timescale processes. *Nature Geoscience*, 14(1):36–42.

Meraner, K., Mauritsen, T., and Voigt, A. (2013). Robust increase in equilibrium climate sensitivity under global warming. *Geophysical Research Letters*, 40(22):5944–5948.

Myhre, G., Shindell, D., Bréon, F., Collins, W., Fuglestvedt, J., Huang, J., et al. (2013). Anthropogenic and natural radiative forcing. *Climate Change 2013: The Physical Science Basis. Contribution of Working Group I to the Sixth Assessment Report of the Intergovernmental Panel on Climate Change*, pages 659–740.

Otto, A., Otto, F. E., Boucher, O., Church, J., Hegerl, G., Forster, P. M., et al. (2013). Energy budget constraints on climate response. *Nature Geoscience*, 6(6):415–416.

Pincus, R., Forster, P. M., and Stevens, B. (2016). The Radiative Forcing Model Intercomparison Project (RFMIP): experimental protocol for CMIP6. *Geoscientific Model Development*, 9(9):3447–3460.

Plesca, E., Grützun, V., and Buehler, S. A. (2018). How robust is the weakening of the Pacific Walker circulation in CMIP5 idealized transient climate simulations? *Journal of Climate*, 31(1):81–97.

Polvani, L. M. and Smith, K. L. (2013). Can natural variability explain observed Antarctic sea ice trends? New modeling evidence from CMIP5. *Geophysical Research Letters*, 40(12):3195–3199.

Proistosescu, C. and Huybers, P. J. (2017). Slow climate mode reconciles historical and model-based estimates of climate sensitivity. *Science Advances*, 3(7):e1602821.

Purich, A., Cai, W., England, M. H., and Cowan, T. (2016). Evidence for link between modelled trends in Antarctic sea ice and underestimated westerly wind changes. *Nature communications*, 7(1):1–9.

Purich, A., England, M. H., Cai, W., Sullivan, A., and Durack, P. J. (2018). Impacts of broad-scale surface freshening of the Southern Ocean in a coupled climate model. *Journal of Climate*, 31(7):2613–2632.

Raper, S. C., Gregory, J. M., and Stouffer, R. J. (2002). The role of climate sensitivity and ocean heat uptake on AOGCM transient temperature response. *Journal of Climate*, 15(1):124–130.

Rayner, N., Parker, D. E., Horton, E., Folland, C. K., Alexander, L. V., Rowell, D., et al. (2003). Global analyses of sea surface temperature, sea ice, and night marine air temperature since the late nineteenth century. *Journal of Geophysical Research: Atmospheres*, 108(D14).

Rugenstein, M., Bloch-Johnson, J., Gregory, J. M., Andrews, T., Mauritsen, T., Li, C., et al. (2020). Equilibrium climate sensitivity estimated by equilibrating climate models. *Geophysical Research Letters*, 47(4):e2019GL083898.

Rye, C. D., Marshall, J., Kelley, M., Russell, G., Nazarenko, L. S., Kostov, Y., Schmidt, G. A., and Hansen, J. (2020). Antarctic glacial melt as a driver of recent Southern Ocean climate trends. *Geophysical Research Letters*, 47(11):e2019GL086892.

Sadai, S., Condron, A., DeConto, R., and Pollard, D. (2020). Future climate response to Antarctic Ice Sheet melt caused by anthropogenic warming. *Science advances*, 6(39):eaaz1169.

Seager, R., Cane, M., Henderson, N., Lee, D.-E., Abernathey, R., and Zhang, H. (2019). Strengthening tropical Pacific zonal sea surface temperature gradient consistent with rising greenhouse gases. *Nature Climate Change*, 9(7):517–522.

Sellar, A. A., Jones, C. G., Mulcahy, J. P., Tang, Y., Yool, A., Wiltshire, A., O'connor, F. M., Stringer, M., Hill, R., Palmieri, J., et al. (2019). UKESM1: Description and evaluation of the UK earth system model. *Journal of Advances in Modeling Earth Systems*, 11(12):4513–4558.

Sherwood, S., Webb, M. J., Annan, J. D., Armour, K., Forster, P., Hargreaves, J., et al. (2020). An assessment of Earth's climate sensitivity using multiple lines of evidence. *Reviews of Geophysics*, 58(4):e2019RG000678.

Shin, Y., Kang, S. M., Takahashi, K., Stuecker, M. F., Hwang, Y.-T., and Kim, D. (2021). Evolution of the tropical response to periodic extratropical thermal forcing. *Journal of Climate*, 34(15):6335–6353.

Silvers, L. G., Paynter, D., and Zhao, M. (2018). The diversity of cloud responses to twentieth century sea surface temperatures. *Geophysical Research Letters*, 45(1):391–400.

Smith, C. J., Kramer, R. J., Myhre, G., Alterskjær, K., Collins, W., Sima, A., et al. (2020). Effective radiative forcing and adjustments in CMIP6 models. *Atmospheric Chemistry and Physics*, 20(16):9591–9618.

Smith, D. M., Booth, B. B., Dunstone, N. J., Eade, R., Hermanson, L., Jones, G. S., Scaife, A. A., Sheen, K. L., and Thompson, V. (2016). Role of volcanic and anthropogenic aerosols in the recent global surface warming slowdown. *Nature Climate Change*, 6(10):936–940.

Soden, B. J. and Held, I. M. (2006). An assessment of climate feedbacks in coupled ocean-atmosphere models. *Journal of climate*, 19(14):3354–3360.

Stevens, B., Sherwood, S. C., Bony, S., and Webb, M. J. (2016). Prospects for narrowing bounds on earth's equilibrium climate sensitivity. *Earth's Future*, 4(11):512–522.

Storelvmo, T., Tan, I., and Korolev, A. V. (2015). Cloud phase changes induced by co_2 warming — A powerful yet poorly constrained cloud-climate feedback. *Current climate change reports*, 1(4):288–296.

Stuecker, M. F., Timmermann, A., Jin, F.-F., Proistosescu, C., Kang, S. M., Kim, D., Yun, K.-S., Chung, E.-S., Chu, J.-E., Bitz, C. M., et al. (2020). Strong remote control of future equatorial warming by off-equatorial forcing. *Nature Climate Change*, 10(2):124–129.

Takahashi, C. and Watanabe, M. (2016). Pacific trade winds accelerated by aerosol forcing over the past two decades. *Nature Climate Change*, 6(8):768–772.

Tardif, R., Hakim, G. J., Perkins, W. A., Horlick, K. A., Erb, M. P., Emile-Geay, J., Anderson, D. M., Steig, E. J., and Noone, D. (2019). Last Millennium Reanalysis with an expanded proxy database and seasonal proxy modeling. *Climate of the Past*, 15(4):1251–1273.

Thompson, D. W. and Solomon, S. (2002). Interpretation of recent Southern Hemisphere climate change. *Science*, 296(5569):895–899.

Trenberth, K. E., Branstator, G. W., Karoly, D., Kumar, A., Lau, N.-C., and Ropelewski, C. (1998). Progress during TOGA in understanding and modeling global teleconnections associated with tropical sea surface temperatures. *Journal of Geophysical Research: Oceans*, 103(C7):14291–14324.

Tsushima, Y., Emori, S., Ogura, T., Kimoto, M., Webb, M., Williams, K., Ringer, M., Soden, B., Li, B., and Andronova, N. (2006). Importance of the mixed-phase cloud distribution in the control climate for assessing the response of clouds to carbon dioxide increase: a multi-model study. *Climate Dynamics*, 27(2):113–126.

Turner, J., Bracegirdle, T. J., Phillips, T., Marshall, G. J., and Hosking, J. S. (2013). An initial assessment of antarctic sea ice extent in the CMIP5 models. *Journal of Climate*, 26(5):1473–1484.

Wang, C. (2006). An overlooked feature of tropical climate: Inter-Pacific-Atlantic variability. *Geophysical Research Letters*, 33(12).

Watanabe, M., Dufresne, J.-L., Kosaka, Y., Mauritsen, T., and Tatebe, H. (2021). Enhanced warming constrained by past trends in equatorial Pacific sea surface temperature gradient. *Nature Climate Change*, 11(1):33–37.

Webb, M. J., Andrews, T., Bodas-Salcedo, A., Bony, S., Bretherton, C. S., Chadwick, R., et al. (2017). The Cloud Feedback Model Intercomparison Project (CFMIP) contribution to CMIP6. *Geoscientific Model Development*, 10(1):359–384.

Webb, M. J., Lambert, F. H., and Gregory, J. M. (2013). Origins of differences in climate sensitivity, forcing and feedback in climate models. *Climate Dynamics*, 40(3).

Webb, M. J., Senior, C., Sexton, D., Ingram, W., Williams, K., Ringer, M., McAvaney, B., Colman, R., Soden, B., Gudgel, R., et al. (2006). On the contribution of local feedback mechanisms to the range of climate sensitivity in two gcm ensembles. *Climate dynamics*, 27(1):17–38.

Winton, M., Adcroft, A., Dunne, J., Held, I., Shevliakova, E., Zhao, M., et al. (2020). Climate sensitivity of GFDL's CM4.0. *Journal of Advances in Modeling Earth Systems*, 12(1):e2019MS001838.

Xie, S.-P. and Philander, S. G. H. (1994). A coupled ocean-atmosphere model of relevance to the itcz in the eastern Pacific. *Tellus A*, 46(4):340–350.

Yuan, X., Kaplan, M. R., and Cane, M. A. (2018). The interconnected global climate system — A review of tropical-polar teleconnections. *Journal of Climate*, 31(15):5765–5792.

Zelinka, M. D., Myers, T. A., McCoy, D. T., Po-Chedley, S., Caldwell, P. M., Ceppi, P., et al. (2020). Causes of higher climate sensitivity in CMIP6 models. *Geophysical Research Letters*, 47(1):e2019GL085782.

Zelinka, M. D., Zhou, C., and Klein, S. A. (2016). Insights from a refined decomposition of cloud feedbacks. *Geophysical Research Letters*, 43(17):9259–9269.

Zhang, H., Griffiths, M. L., Chiang, J. C., Kong, W., Wu, S., Atwood, A., Huang, J., Cheng, H., Ning, Y., and Xie, S. (2018). East Asian hydroclimate modulated by the position of the westerlies during termination i. *Science*, 362(6414):580–583.

Zhang, L., Delworth, T. L., Cooke, W., and Yang, X. (2019). Natural variability of Southern Ocean convection as a driver of observed climate trends. *Nature Climate Change*, 9(1):59–65.

Zhang, X., Deser, C., and Sun, L. (2021). Is there a tropical response to recent observed Southern Ocean cooling? *Geophysical Research Letters*, 48(5):e2020GL091235.

Zhou, C., Zelinka, M. D., and Klein, S. A. (2016). Impact of decadal cloud variations on the Earth's energy budget. *Nature Geoscience*, 9(12):871–874.

Zhou, C., Zelinka, M. D., and Klein, S. A. (2017). Analyzing the dependence of global cloud feedback on the spatial pattern of sea surface temperature change with a Green's function approach. *Journal of Advances in Modeling Earth Systems*, 9(5):2174–2189.